Theses and Dissertations   1. Thesis and Dissertation Collection, all items

1985

A diagnostic study of baroclinic disturbances in polar air streams.

Sinclair, Mark R.

http://hdl.handle.net/10945/21276

NAVAL POSTGRADUATE SCHOOL
Monterey, California

THESIS

A DIAGNOSTIC STUDY OF BAROCLINIC DISTURBANCES
IN POLAR AIR STREAMS

by

Mark R. Sinclair

September, 1985

Thesis Advisor: R. L. Elsberry

T227030

SECURITY CLASSIFICATION OF THIS PAGE *(When Data Entered)*

REPORT DOCUMENTATION PAGE		READ INSTRUCTIONS BEFORE COMPLETING FORM
1. REPORT NUMBER	2. GOVT ACCESSION NO.	3. RECIPIENT'S CATALOG NUMBER
4. TITLE *(and Subtitle)* A Diagnostic Study of Baroclinic Disturbances in Polar air Streams		5. TYPE OF REPORT & PERIOD COVERED Doctoral Dissertation September 1985
		6. PERFORMING ORG. REPORT NUMBER
7. AUTHOR(s) Mark R. Sinclair		8. CONTRACT OR GRANT NUMBER(s)
9. PERFORMING ORGANIZATION NAME AND ADDRESS Naval Postgraduate School Monterey, CA 93943-5100		10. PROGRAM ELEMENT. PROJECT. TASK AREA & WORK UNIT NUMBERS
11. CONTROLLING OFFICE NAME AND ADDRESS Naval Postgraduate School Monterey, CA 93943-5100		12. REPORT DATE September 1985
		13. NUMBER OF PAGES 193
14. MONITORING AGENCY NAME & ADDRESS(If different from Controlling Office)		15. SECURITY CLASS. (of this report)
		15a. DECLASSIFICATION DOWNGRADING SCHEDULE

16. DISTRIBUTION STATEMENT *(of this Report)*

Approved for public release; distribution unlimited

17. DISTRIBUTION STATEMENT *(of the abstract entered in Block 20, If different from Report)*

18. SUPPLEMENTARY NOTES

19. KEY WORDS *(Continue on reverse side if necessary and identify by block number)*

Polar lows
Baroclinic disturbance
Budget study

20. ABSTRACT *(Continue on reverse side if necessary and identify by block number)*

Model-generated data and FGGE analyses are used to calculate quasi-Lagrangian budgets of mass, vorticity, heat and moisture following disturbances that form within polar air streams. These polar lows grow primarily through basic

baroclinic instability processes and exhibit many features of larger maritime extratropical cyclones. Polar lows that originate on the equatorward side of a nearly straight upper-level jet are contrasted with lows that form on the poleward side of the jet and have considerable mid-tropospheric positive vorticity advection at formation time. The absence of favorable coupling to a jet stream was the missing factor in two model-generated polar lows that failed to develop. Although the vorticity balance is initially different for the two types of polar lows, the vorticity budgets during later stages are similar. The heat budget and the thickness tendency equation demonstrate that the self-development process that is present in larger maritime cyclones is also important for polar low intensification.

A Diagnostic Study of Baroclinic Disturbances
in Polar Air Streams

by

Mark R. Sinclair
B.Sc.(hons), University of Otago,
Dunedin, New Zealand, 1976

Submitted in partial fulfillment of the
requirements for the degree of

DOCTOR OF PHILOSOPHY

from the

NAVAL POSTGRADUATE SCHOOL
September 1985

ABSTRACT

Model-generated data and FGGE analyses are used to calculate quasi-Lagrangian budgets of mass, vorticity, heat and moisture following disturbances that form within polar air streams. These polar lows grow primarily through basic baroclinic instability processes and exhibit many features of larger maritime extratropical cyclones. Polar lows that originate on the equatorward side of a nearly straight upper-level jet are contrasted with lows that form on the poleward side of the jet and have considerable mid-tropospheric positive vorticity advection at formation time. The absence of favorable coupling to a jet stream was the missing factor in two model-generated polar lows that failed to develop. Although the vorticity balance is initially different for the two types of polar lows, the vorticity budgets during later stages are similar. The heat budget and the thickness tendency equation demonstrate that the self-development process that is present in larger maritime cyclones is also important for polar low intensification.

TABLE OF CONTENTS

LIST OF FIGURES

9

11

ACKNOWLEDGEMENTS

I. INTRODUCTION

A. POLAR AIR STREAM CYCLOGENESIS

The existence of cyclogenesis in polar air streams upstream or poleward of the main polar frontal cloud band has long been recognized by operational meteorologists. Such disturbances form primarily over the ocean in winter (Reed, 1979), and are of relatively small size (500-1500 km) compared with the typical extratropical cyclone. Over the ocean, their incipient stage is sometimes characterized by areas of locally enhanced cumulonimbus activity. This convective activity may later become organized into a comma-shaped cloud pattern (Reed, 1979; Mullen, 1983), or acquire features similar to tropical storms (Rasmussen, 1979). The disturbance is often accompanied by appreciable convective precipitation, and occasionally by severe weather (Stevenson, 1968; Suttie, 1970; Lyall, 1972; Seaman et al., 1982). Cyclogenesis is sometimes vigorous with considerable areal expansion of the disturbance (e.g., Cook, 1983; Mullen, 1983). The terms polar low, polar air depression, polar trough, cold trough, airmass trough, comma cloud, polar disturbance, cold vortex, Arctic instability low, and Arctic Bomb have been applied to this phenomenon. The term "polar low" will here refer to any cyclonic disturbance originating within a polar air stream.

Polar low occurrence is more widespread and frequent than the relatively sparse treatment in the literature would imply. Weber and Wilderotter (1981) state that polar air stream cyclogenesis is the most frequent type observed over both the North Atlantic and North Pacific Oceans, and the North American continent. Monteverdi (1976) shows that

13

between 20% and 50% of the annual San Francisco precipitation occurs in association with non-frontal air mass disturbances akin to the polar low. Cyclogenesis away from pre-existing cloud bands accounts for about 50% of all Southern Hemisphere winter cyclogenesis (Streten and Troup, 1973). Clark (1977) estimates that polar lows are involved in two-thirds of all winter cyclogenesis events in the Southern Hemisphere, where development is frequently of the so-called "instant occlusion" mode (Carleton, 1981). An instant occlusion forms when a polar low (evidenced by organized convection, usually in a comma formation) advances on an incipient frontal wave development. The resulting cloud vortex rapidly develops the signature of a mature occluded system (Anderson et al., 1969). Sometimes the comma cloud and frontal wave merge. In other cases, the comma cloud develops into the occlusion, distinct from the main front (Locatelli et al., 1982).

It has been suggested that two different types of polar lows exist (Rasmussen, 1979, 1981; Locatelli et al., 1982; Sardie and Warner, 1983). Satellite imagery indicates that polar lows exhibit a variety of cloud signatures (Forbes and Lottes, 1982). Some bear the hallmarks of organized convective tropical cloud systems. Okland (1977) and Rasmussen (1979) applied thermal instability theory to these systems and proposed that heating and cumulus convection play essential roles in their development. These convective disturbances form within the polar air mass well to the north of the polar jet.

The second type of polar low is more baroclinic in nature. In a case study of a polar low that crossed the British Isles, Harrold and Browning (1969) noted that enhanced baroclinity was evident at early stages. In addition, the area of significant precipitation was produced by stable large-scale ascent rather than by small-scale

convection. Such baroclinic disturbances are found to develop in the vicinity of the polar jet, and to exhibit cloud features typical of larger extratropical cyclones (Reed, 1979; Mullen, 1979, 1983; Locatelli et al., 1982; Cook, 1983). Because these baroclinic disturbances are common in the Pacific Ocean, they are frequently called Pacific polar lows.

B.   PURPOSE OF STUDY

The purpose of this study is to investigate the reasons for the formation and growth of the Pacific polar low. It has been proposed that baroclinic instability modified by diabatic processes, is responsible for the growth of the Pacific polar low (Sardie and Warner, 1983; Hodur, 1984). According to Reed (1979), there is little evidence to support the view that the Pacific polar low is a purely convective, barotropic phenomenon. However, the larger-scale organization of convection which is frequently observed in conjunction with polar lows may contribute to development. Thus, it is important to consider the effects of moist processes on development.

The early studies of baroclinic instability (Charney, 1947; Eady, 1949) showed that the longer wavelengths (>4000 km) are the most unstable, and observations verify that this scale is most prevalent in mid-latitudes. The small scales of polar lows compared with typical mid-latitude baroclinic disturbances may be explained by the small static stabilities which exist at low levels. This explanation was tested by Mansfield (1974) and Duncan (1977) who applied model calculations to observational data from polar low cases, and found predicted wavelengths close to those observed.

Further support for baroclinic instability being the primary mechanism for polar low development is offered in

15

recent theoretical studies. Gall (1976a) and Staley and
Gall (1977) used linear models to show that flows having a
Richardson number significantly lower near the surface than
aloft favor higher growth rates for short waves. Since the
Richardson number measures the ratio of static stability to
the square of the vertical wind shear (i.e., baroclinity),
this theory suggests that the small horizontal scales of
polar lows result from either reduced static stability or
enhanced baroclinity (or both) near the surface as compared
to that aloft.

Linear baroclinic theory using uniform zonal flow
predicts that short baroclinic waves are confined to near
the surface (Staley and Gall, 1977; Mansfield, 1974). This
is at variance with polar low observations (Harrold and
Browning, 1969; Reed, 1979; Mullen, 1979) which exhibit
significant geopotential perturbations near the tropopause.
Tokioka (1973), Gall (1976b) and Hodur (1984) found that the
inclusion of latent heat resulted in a deeper disturbance, a
shift of the maximum growth rates to shorter waves, and a
general increase in growth rate. Small-scale cyclonic
development occasionally occurs over the winter continent in
the absence of significant moist convection or surface
fluxes (Mullen, 1982). Additional theory is needed to
explain the small scales and vertical depth of these drier
disturbances.

Reed (1979) suggested that the comparison of polar low
structure with results from linear baroclinic theory might
not be valid because polar lows frequently develop on
already perturbed basic states. Frederiksen (1979) showed
that the presence of basic state planetary waves causes the
maximum amplitude for linear baroclinic waves to occur in
the upper troposphere as opposed to purely zonal large-scale
states which generally exhibit maximum amplitudes near the
surface. Blumen (1980) showed that nonlinear interaction

16

between growing long and short baroclinic waves can produce a deep disturbance of short horizontal scale.

A goal of this research is to clarify the relative importance of upper and low-level forcing in polar low formation. The studies discussed earlier indicate that the occurrence of an upper-level perturbation is a consequence of baroclinic development and is related to the effects of latent heating and nonlinear processes. The presence of an upper-level disturbance at later stages of polar low development is apparent from the associated comma-shaped cloud pattern. Such features are frequently referred to as upper-level vorticity maxima by forecasters (Reed, 1979). However, the role of upper-level features in early stages of polar low formation is not clear. The polar lows described by Reed (1979) and Mullen (1979) form on the poleward side of the upper-level wind maximum under cyclonic upper-level flow. In contrast, the polar low of Cook (1983) initially formed beneath anticyclonic flow on the equatorward side of the upper jet. It is apparent that in some circumstances, polar lows form as a result of low-level baroclinic processes (Mansfield, 1974; Harrold and Browning, 1969) while in others, upper-level forcing is present (Reed, 1979).

An additional goal of this work is to clarify the role of surface fluxes in polar low formation and development. Polar lows form mostly over the oceans in winter (Reed, 1979) when surface heating is largest. Mullen (1979) showed that large air-sea temperature differences accompany Pacific polar lows, especially at genesis. In addition, numerical simulations have shown that latent heat release and surface fluxes are essential for polar low development (Sandgathe, 1981), and for realistic structure and growth rates (Hodur, 1984). On the other hand, Mansfield (1974) found that surface fluxes hinder polar low development by adding heat in antiphase to the growing temperature wave. Danard and

Ellenton (1980) suggested that heating in the cold sector of a developing cyclone destroys available potential energy. These authors and Bosart (1981) suggested that the role of the surface fluxes is to establish a favorable low-level environment for polar low development.

C. HYPOTHESIS

The main hypothesis of this study is that Pacific-type polar lows form as a result of moist baroclinic instability. As such, they exhibit many typical features of extratropical cyclones. It is proposed that the baroclinic polar low may form initially under straight upper-level flow, or alternately, downstream from a significant pre-existing upper-level trough. Subsequent development may be described in terms of the "self-development" mechanism. The upward sensible heat flux maintains the reduced low-level static stability which is required for continued development of the disturbance. The surface moisture flux ensures an abundant supply of moisture for condensation which considerably enhances cyclogenesis by the enhancement of vertical ascent and generation of available potential energy.

To test this hypothesis, a diagnostic analysis of several model-generated and observed polar lows is performed. The simulated polar lows formed realistically in the polar air stream of a mature cyclone. Therefore, the effects of nonlinear interactions and a perturbed large-scale state, previously shown to be important, are present from genesis. By contrast, many modelling studies start with a uniform zonal initial state. Model output forms a complete data set accurate to computer roundoff, with much improved spatial and temporal resolution over observational data. Adequate resolution is crucial for such a study of polar lows. Conclusions drawn from study of the model data will be validated by similar analysis of observed polar lows.

18

Polar low formation and evolution is interpreted in a vorticity and thermodynamic balance context. Storm-following budgets of vorticity and heat are used to diagnose important physical processes and are related via hydrostatic arguments. A moisture budget aids interpretation of diabatic terms in the heat budget. The analysis is complete, because the vorticity and thermodynamic equations contain no assumptions or approximations.

The study consists of four sections. Chapter II describes the quasi-Lagrangian diagnostic analysis applied to examples of polar low development as simulated by the United States Navy Operational Global Atmospheric Prediction System (NOGAPS) model (Sandgathe, 1981), and occurring in the First GARP Global Experiment (FGGE) data set. Chapter III describes examples of polar lows from both the FGGE data and the NOGAPS simulations which develop under straight upper-level flow. Polar lows which form in the presence of a pre-existing upper-level trough will be analyzed in Chapter IV. Finally, these developing disturbances will be compared with non-developing disturbances to understand why some disturbances grow and others do not (Chapter V). Numerical details of the quasi-Lagrangian diagnostics are presented in the Appendix.

II. NUMERICAL PROCEDURE

This study of polar lows is based on both the results of numerical simulations and observational FGGE data. The rationale for using model-generated data is that the distribution of conventional observations over the oceans is inadequate to resolve polar low disturbances. Model output forms a complete data set; that is, fields of meteorological variables which are consistent solutions to the primitive equations are available at every gridpoint to computer roundoff accuracy. The atmospheric model (NOGAPS) includes a sophisticated parameterization of boundary layer and diabatic processes, which have been shown to be important for polar low development. Such a complete and accurate specification of physical processes cannot be achieved in an observational study.

In observational studies, many important processes are diagnosed indirectly. Direct measurements of latent heat release, surface fluxes, radiative effects and friction are seldom available. Rather, these processes are usually estimated from the observed fields of wind, temperature and moisture. For example, diabatic effects are usually calculated as a heat budget residual using an estimate of vertical velocity derived from the horizontal wind fields. Surface fluxes of heat, moisture and momentum (friction) are diagnosed via empirical relationships. In the NOGAPS model, these internal processes are calculated directly in a mutually consistent fashion, and are available at every gridpoint to computer roundoff accuracy. Thus, it is possible to study quantitatively the effect of these processes on model storm development (e.g. Sandgathe, 1981; Winninghoff and Elsberry, 1983; Bosse, 1984; Liou and Elsberry, 1985).

Another important advantage to using model-generated data is the increased time resolution. Polar lows are typically short-lived so the coarse (12 h) time resolution of most observational analyses is often inadequate to fully describe rapid changes. The increased precision of time derivatives coupled with the dynamic consistency of the model-generated fields should yield reliable diagnoses of model storm processes. The residuals of budget-type calculations in which a time derivative is related to the sum of several processes should provide an estimate of the integrity of the diagnostic routines. Error also arises from numerical approximations within the model (e.g. finite differences), so the residual only provides an upper bound on numerical uncertainty associated with the diagnostic routines.

It should be emphasized that the fidelity of the model simulations in describing natural processes is strongly model dependent. The model is at best an incomplete representation of the atmosphere, and results are affected by numerical solution techniques. Physical processes are parameterized in the model. Although computed to computer round-off accuracy, they are only approximations to true atmospheric physical processes. Therefore, the study of model output will only serve as a guide to the study of observational data. Conclusions based on the analysis of the model are validated only when corroborated by similar results from the observational data. FGGE analyses provide the best opportunity for such a study of maritime cyclogenesis.

The following sections describe the NOGAPS model and brief details of the simulations, the FGGE data set and the basis of the quasi-Lagrangian budget analysis scheme.

A. NOGAPS SIMULATIONS

The "model-data" sets used for this study are from the simulations of Sandgathe (1981) to determine the role of sensible and latent heat fluxes on extratropical cyclo-genesis.   The model integrations started with idealized zonal initial conditions representative of transition season climatology in each hemisphere.   During the first few days of model integration,   a cyclone which resembled a typical mid-latitude disturbance developed   in each hemisphere. After about 6 days of model integration, a variety of secon-dary, smaller-scale disturbances developed.   Most of these secondary cyclones resembled polar lows in that they formed and developed in the western (polar) sector of the parent low.   Some of these disturbances developed rapidly and even-tually replaced the parent cyclone as the primary low center. Others migrated cyclonically about the parent low with little change in intensity.   One of the goals of the diagnostic studies with numerically-simulated data is to determine quantitatively the mechanisms which cause some of these lows to develop whereas others do not. Then the same diagnostic analysis will be applied to polar lows chosen from the FGGE data to demonstrate the validity of conclu-sions that are drawn from the model-generated set.

The NOGAPS model used to simulate the polar lows for this study is a state-of-the-art atmospheric model developed by the United States Naval Environmental Prediction Research Facility (NEPRF),   based on a version of the UCLA general circulation model.   NOGAPS is a sigma-coordinate primitive-equation model with six vertical layers and it utilizes the Arakawa scheme C staggered grid horizontal differencing scheme. The adiabatic model dynamics are described in detail by Arakawa and Lamb (1977).   The model diabatic package includes   the   Arakawa   and   Schubert   (1974)   cumulus

22

parameterization scheme, and the Randall (1976) version of the Deardorff (1972) planetary boundary layer parameterization. A good overview of the model diabatics is given by Rosmond (1981); it will not be reproduced here. For the experiments of Sandgathe (1981), a sectorized version of NOGAPS featuring cyclic east-west continuity was used. A horizontal domain of 60° longitude by 180° latitude (pole to pole) with a resolution of 2.5° longitude by 2° latitude was used. The version of the NOGAPS model used by Sandgathe (1981) is not the present version.

Sandgathe (1981) investigated the role of air-sea fluxes and latent heating in the development of the secondary cyclones by selectively witholding these physical processes at various stages of development. In the experiments where either surface moisture flux, or all diabatic processes (including latent heating) were witheld, development of the secondary lows was hindered. Sandgathe suggested that the model development of the secondary lows was brought about by low-level thermal processes, and that surface fluxes significantly modify the low-level environment, and thus contribute to development.

The polar lows in these simulations develop within a realistic context. Since the model has been integrated for 6 days before they appear, it is expected that the full spectrum of waves is present. Therefore, the effects of nonlinear wave-wave interactions are included, and the polar lows grow in the polar air stream of the parent low, as is the case in nature.

Model output is initially on a staggered grid, and in sigma vertical coordinates. Prior to diagnostic calculations, the meteorological variables were interpolated onto pressure surfaces, smoothed to remove unwanted noise, and then interpolated onto the diagnostic budget grid using a bicubic spline fit to the smoothed isobaric gridpoint data.

23

B. FGGE ANALYSIS

The First GARP Global Experiment (FGGE) has resulted in the most extensive global atmospheric data set ever collected by the meteorological community (Halem et al., 1982). Particular emphasis was placed on data-sparse areas. The conventional observational data base comprising surface (land and ships) observations, rawindsondes, pilot balloons and aircraft data was supplemented by satellite-derived soundings and cloud-drift winds, ocean buoys and reconnaissance flights with dropsondes. This improved data base is particularly useful for studying maritime weather systems.

The FGGE data have been combined into dynamically consistent analyses at the European Centre for Medium Range Weather Forecasts (ECMWF), as described by Bengtsson et al., (1982). The ECMWF data-assimilation system consists of a three-dimensional multivariate optimum interpolation, a nonlinear normal mode initialization and an automatic system for data checking. A 15-level model with a horizontal resolution of 1.875° lat/long is used for the dynamical assimilation which results in the level III-B analyses used in this study. Fields archived are geopotential heights, horizontal wind components, mean sea-level pressure, initialized temperature, relative humidity and initialized vertical velocity for the 15 standard levels up to 10 mb. Climatological sea-surface temperature (SST) data are used in the physical parameterization package of the model. Global analyses for 0000 GMT and 1200 GMT are archived for the period December 1978 to July 1979. During the two special observing periods, January/February and June 1979, additional analyses were produced for 0600 GMT and 1800 GMT. Previous studies using the six-hourly FGGE data (Cook, 1983; Wash and Cook, 1985; Calland, 1983; Wash and Calland, 1985) noted problems with the data at 0600 GMT and 1800 GMT.

24

Therefore, data from these times were not utilized in the present study.

The FGGE data were interpolated onto the budget grid in the same manner as the model-generated data. However, since the FGGE data were already on isobaric surfaces, no vertical interpolation was required.

C. QUASI-LAGRANGIAN DIAGNOSTICS

The quasi-Lagrangian budget approach used in this study relates time changes in the volume average of a basic meteorological quantity (e.g. mass, vorticity, heat, moisture) to net gain due to transport of that property through the boundaries of the budget volume and to sources and sinks within the volume. The budgets presented in the following sections are calculated by replacing f in (A.1) (see Appendix) by the property of interest. Vertical velocity is computed using the kinematic method as described in the Appendix. The sources and sinks are identified as dynamical and physical processes within the volume, and are determined via the governing equations for the property. Thus, the budget analysis provides a quantitative measure of cyclone development or dissipation in terms of its interaction with the environment and in terms of the various physical and dynamical processes within the budget volume.

The budget residual includes the effects of interpolation and truncation errors, as well as additional physical processes not included in the budget formulation. When observed data are used, additional contributions to the residual arise from inherent data uncertainty, and from subgrid scale processes not detectable on the discrete grid. When model output is used as data, it is possible to formulate the governing equation in a manner that is mathematically consistent with model processes. In that case, the

25

budget residual results solely from truncation and interpo-
lation errors.

The budget volume is centered on and translates with a
distinguishable feature of the developing cyclone (or polar
low). This study utilizes the spherical geometry of the
quasi-Lagrangian diagnostic budget framework formulated by
Johnson and Downey (1975). Spherical budget volume geometry
is especially suitable because many atmospheric systems are
quasi-circular in shape. The size of the volume is chosen
to approximate the scale of the cyclone. The
quasi-Lagrangian approach permits separation of the advec-
tive effects associated with the translation of the system
from the processes which force development. The transport of
storm properties is determined relative to the moving storm.
Features of cyclone development are interpreted in a mean-
ingful manner as changes relative to a moving storm. The
governing equation for the property of interest is expressed
in the quasi-Lagrangian framework by replacing the Eulerian
local rate of change ($\partial/\partial t$) with $\delta/\delta t - \mathbf{C}.\nabla$, where $\delta/\delta t$ is
the rate of change following the system, and $\mathbf{C}$ is the trans-
lation velocity of the system which is computed as described
in the Appendix.

Budget results are often presented in time-section form.
Because the budget is evaluated at every model output or
data assimilation time, these results are used to describe
the time-evolution of storm processes. A cubic spline fit
in time is used to provide an instantaneous estimate of the
time-derivative term. This technique preserves the original
time resolution of the data by removing the need for time-
averaging. This feature is especially important for the FGGE
data which are sampled only every 12 h. Most previous budget
studies employ a finite-difference approximation to the time
derivative, which is subject to large truncation errors. To
minimize the time truncation error, the time difference is

26

usually taken over the smallest possible increment and the remaining budget terms time-averaged over this period.

The budget approach emphasizes area and boundary averaged processes over the budget domain. To examine spatial details of storm processes, horizontal fields of terms in the governing equation for the property of interest are also presented for selected times and levels. These fields are also presented in storm-following coordinates.

A bicubic spline is used to interpolate the data onto the budget grid and to compute the various terms for the horizontal representation. Because the data are represented throughout the x, y plane by the bicubic spline function, the values on the budget grid are obtained by evaluating the cubic at the budget gridpoint location. Analytic differentiation of this cubic yields mutually consistent estimates of the horizontal derivatives up to degree two. This is computationally efficient because terms involving horizontal derivatives occurring in (A.1) or the governing equations are calculated from a single spline fit to the original data. This considerably simplifies computation by avoiding the further step of calculating finite differences on the budget grid, or alternately computing these on the rectangular data grid and interpolating the results onto the budget domain. Since the spline is initially fitted to an area larger than the budget domain area, there is no degradation near the boundaries as occurs with finite differences. Such use of cubic splines also preserves the important smaller-scale synoptic features being studied here. For example, vorticity advection involves second derivatives of velocity. The simplest finite difference technique requires three grid points which involves values representing a distance of 7.5° for a 2.5° grid. This is undesirable for the scale of disturbance considered here. Calculating such terms from the original bicubic spline fit

to the horizontal wind field is computationally efficient and results in a much more accurate representation of the local derivative. Further details are provided in the Appendix, which includes a derivation of the quasi-Lagrangian vorticity advection term in spherical coordinates.

The cubic spline has additional mathematical properties which make it suitable for use in meteorological analysis. Because both the gradient and curvature of the bicubic spline fit are everywhere continuous, the meteorological variable is represented as a smoothly varying property. In one dimension, the cubic spline results from a minimization of the domain integral of the square of the second derivative of the property of interest (Marchuk, 1982). For wavelike functions, this ensures a preferential attenuation of some analogue of short-wave energy. Such a property is clearly desirable, since the original grid permits only wavelengths longer than twice the grid spacing.

III. CYCLOGENESIS UNDER STRAIGHT UPPER FLOW

In this study, the Pacific (or baroclinic) polar low is further classified into two types. This classification is based on conditions at polar low formation. The first (Type I) appears initially as a shallow baroclinic disturbance equatorward of the jet streak under straight or even anticyclonic upper-level flow. The incipient low is associated with light surface winds and is located to the upstream of a mature cyclone. The low develops in the polar air stream of the parent cyclone and increases in both vertical and horizontal extent. The polar low develops characteristics of a typical small-scale maritime extratropical cyclone, and eventually may replace the primary low as the main circulation center. The second class of polar low (Type II) is distinguished from the first in that it forms on the poleward side of the upper-level jet in a strong surface polar air stream beneath positive vorticity advection (PVA) aloft. Examples of Type II disturbances are found in Reed (1979) and Mullen (1983). Because later stages of development are similar for both types, discrimination between types I and II is possible only at genesis.

Over the data-sparse oceans it is not always clear whether upper-level PVA is present at early stages of storm development. An advantage of model-generated data is that the early stages of development can be traced completely to determine the relative roles of upper-level and lower-level processes.

Type I polar lows - those developing under straight upper-level flow - will be examined in this section. To illustrate the analysis technique, the description of the diagnostic budget results will be quite detailed. Synoptic

29

charts, and mass, vorticity, heat and moisture budgets are employed in this study. Within this diagnostic framework, the role and importance of latent heat release, and surface sensible and moisture fluxes will be evaluated. An example of a Type I polar low has been taken from the simulated data set. The North Atlantic storm analyzed by Cook (1983) and Wash and Cook (1985), using the FGGE data, will provide the observational example. Cook's mass and vorticity budget analysis will be extended to include heat and moisture diagnostics.

A. SYNOPTIC OVERVIEW

1. NOGAPS Case

Geopotential and vorticity maps for selected times for the model-generated polar low are shown in Fig. 3.1 a-f. The indicated longitude is based on the 60° cyclic east-west continuity used for the NOGAPS simulations. The surface low originated as an eastward extension from a cyclone situated far to the west (Fig. 3.1 a). The central pressure of the incipient disturbance was around 1009 mb. The initial 500 mb flow (Fig. 3.1 d) is generally anticyclonic and only weakly perturbed. A tongue of weak positive vorticity is located slightly to the west of the surface disturbance. The 700 mb vorticity field for this time (not shown) is also predominantly undisturbed, which suggests that the disturbance initially was very shallow. During the first 24 h (Fig. 3.1 a,b), the surface low becomes embedded in the northwesterly flow behind the parent cyclone, which is located to the east, and the central vorticity intensifies from 5×10^{-5} s^{-1} to 10×10^{-5} s^{-1}. It is at this stage that the system is best classified as a polar low. The 500 mb pattern for this time (Fig. 3.1 e) indicates considerable amplification of the downstream vorticity minimum.

30

During the first 24 h, this 500 mb vorticity minimum strengthened from -4×10^{-5} s^{-1} to less than -10×10^{-5} s^{-1} while the upstream vorticity maximum increased by less than half this amount. This increase in the vorticity variation along the flow results in increasing PVA aloft (Fig. 3.1 e,f).

The polar low subsequently translated about the primary low and eventually became the main center. At the end of the time period (Fig. 3.1 c), the surface low is a tight, closed circulation with a central pressure of 985 mb. Thus, the surface pressure decreased about 18 mb in 30 h. A secondary vorticity maximum is evident in this figure at the location "w". At 500 mb (Fig. 3.1 f), the short-wave cyclonic feature has expanded to a broadly cyclonic flow. The vorticity maximum at this time is strongly asymmetric, with cyclonic extensions to the east and southwest.

Based on the 300 mb isotach analysis (Fig. 3.2 a-c), the polar low formed in the zone between the entrance region of two 35 ms^{-1} jet streaks. After 24 h, the cyclone is located south of a well-developed jet streak. Increasing negative shear vorticity downstream from the center (Fig. 3.1 d, e) is associated with the strengthening of this jet streak. The surface cyclone is located equatorward of the jet for the first 36 h of development. At 276 h, the surface cyclone lies directly below the jet axis. At maturity (Fig. 3.2 c), the low is located at the poleward exit region of a cyclonically curved jet.

Vertical motion fields (Fig. 3.2 d-f) show that the strongest ascent occurs in the eastern sector of the distur-bance, and exhibits the characteristic "comma" shape. It is noteworthy that almost the entire comma lies equatorward of the upper jet axis during early stages of development (Fig. 3.2 d,e). At the end of the period (Fig. 3.2 f), there is a secondary weaker ascent maximum to the south of the cyclone which occurs in the expected location of the cold front.
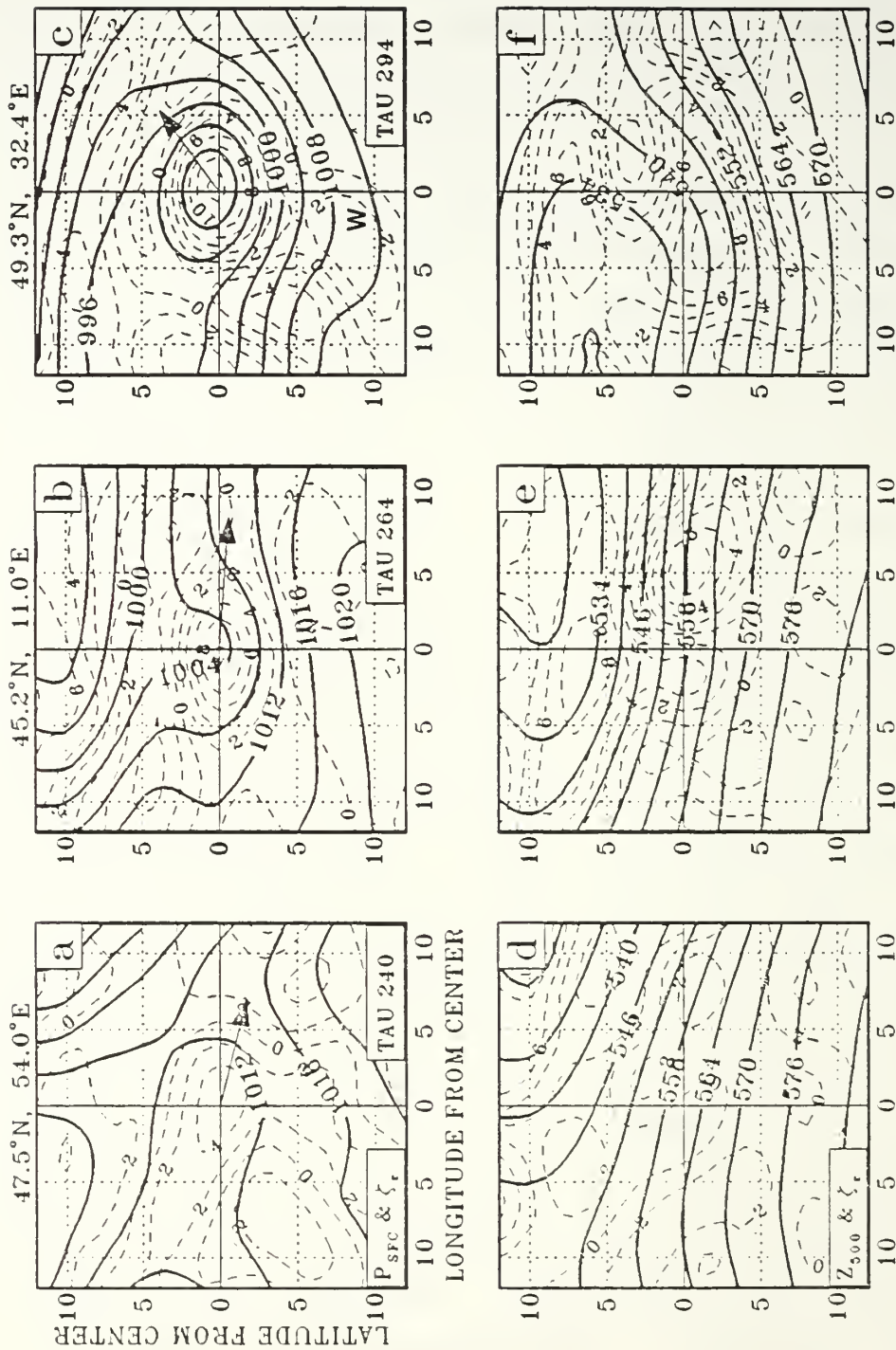
31

Fig. 3.1.   (a-c) Surface pressure (mb, solid) and relative vorticity
(10^{-5} s^{-1}, dashed); and (d-f) 500 mb heights (dam, solid)
and relative vorticity (10^{-5} s^{-1}, dashed) for NOGAPS Type
I. The coordinates of the surface vorticity center are speci-
fied at the top of the figure and the translation velocity
is indicated by the arrow such that 5° of latitude corresponds
to 10 ms^{-1}. Time is indicated in the lower right corner.
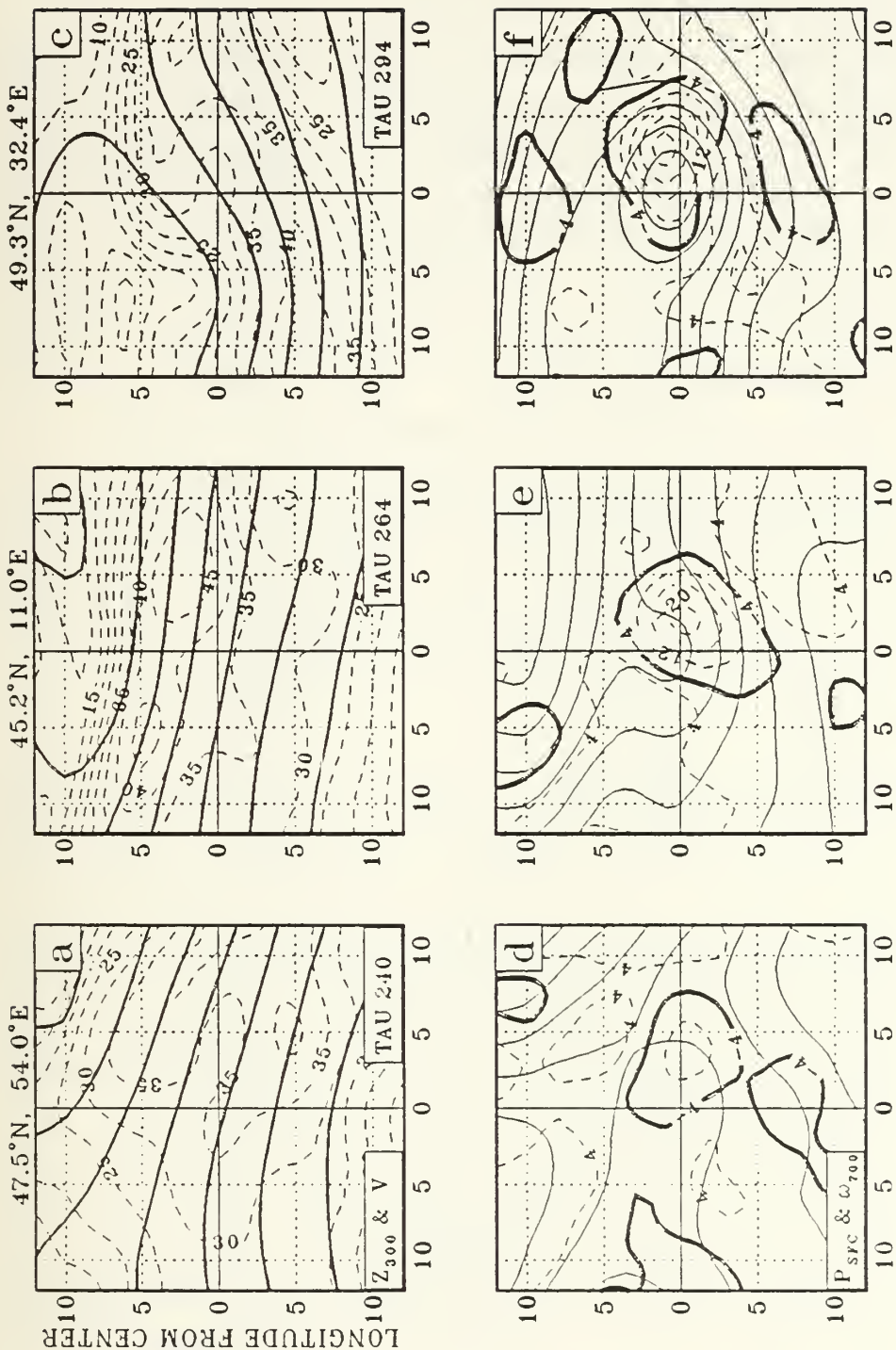
Fig. 3.2. (a-c) 300 mb heights (contours every 120 dam, solid) and wind speed (ms⁻¹, dashed); and (d-f) surface pressure (contours every 4 mb, solid) and 700 mb vertical p-velocity (mb h⁻¹, dashed), except that -4 mb h⁻¹ isoline highlighted for clarity) for NOGAPS Type 1. Format as in Fig. 3.1.

The thermal fields for this case are shown in Fig. 3.3. The initial surface disturbance (Fig. 3.3 a) is close to the thermal ridge in a zone of appreciable baroclinity. With this particular phase relationship, the thermal advection patterns tend to amplify both the thermal ridge ahead of the low and the cold trough behind it. A zone of confluence ahead of the disturbance results in further strengthening of the horizontal temperature gradient after 24 h (Fig. 3.3 b). By the end of the sequence (Fig. 3.3 c), the baroclinity is weaker, and a general cooling has occurred, especially in the western sector. At 500 mb (Fig. 3.3 d), the initial temperature gradient in the vicinity of the low is weak. However, the strong cold advection far to the north serves to enhance the thermal contrast immediately to the north of the surface development (Fig. 3.3 e). By the end of the sequence, strong cooling has occurred in the western sector (Fig. 3.3 f), which results in thermal patterns similar to those at the surface at this time.

2. FGGE Case

The observational Type I case is the slightly more intense North Atlantic storm analyzed by Cook (1983) and Wash and Cook (1985). A detailed synoptic discussion of this storm is found in those studies; salient features only will be presented here. Synoptic charts for this North Atlantic disturbance are shown in Figs. 3.4 to 3.6. The surface low formed just to the west of Iceland and deepened from near 1009 mb to 976 mb as it moved southeastward toward the British Isles (Fig. 3.4 a-c). The storm developed in the northerly flow around a stationary, occluded system situated off the coast of Norway and eventually replaced this as the primary circulation center. The incipient low formed beneath a 500 mb ridge (Fig. 3.4 d). However, a short-wave trough that formed about 8° latitude to the northwest of the

34

Fig. 3.3. (a-c) As in Fig. 3.1 a-c except surface temperature (°C, dashed); (d-f) as in Fig. 3.1 d-f except 500 mb temperature (°C, dashed).
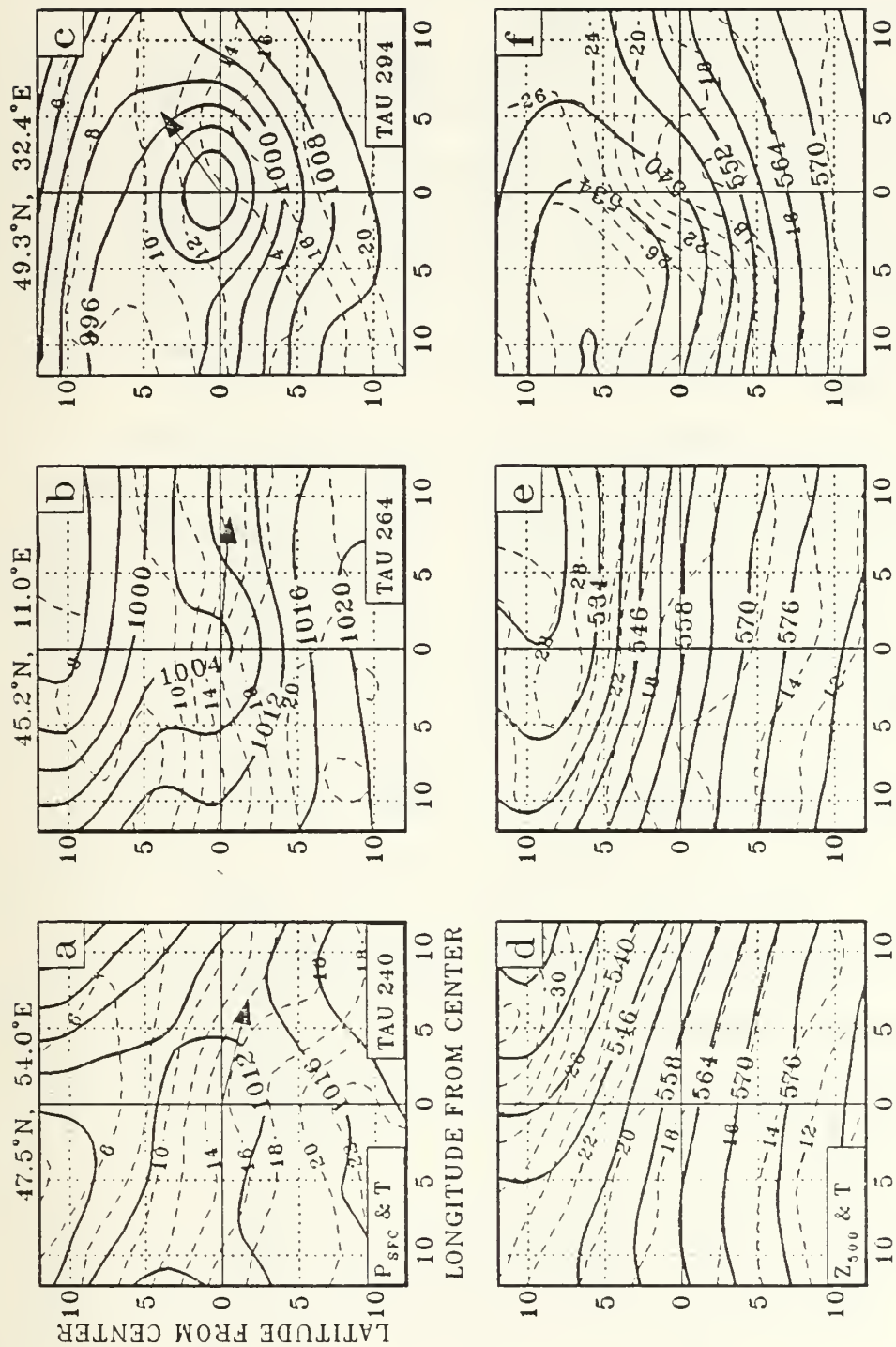
surface disturbance developed concurrently with the low-level cyclone to become a significant upper trough by the end of the period (Fig. 3.4 e,f).

The initial surface development occurred in a thermal ridge to the south of a strong baroclinic zone (Fig. 3.5 a,d). As development progressed, the baroclinic zone moved south to a location near the surface disturbance (Fig. 3.5 b,e). At maturity, very little of the original baroclinity remains (Fig. 3.6 c,f). The surface temperature maxima in Fig. 3.5 a,b occur near the locations of the strongest surface pressure gradient. This suggests that these locations are warmed by the surface heat fluxes which are strongest when the surface wind is strong. In comparison with the NOGAPS thermal analysis (Fig. 3.3), the FGGE surface temperature field is rather noisy. Since the surface observations incorporated in the FGGE data set include those from a variety of sources including land-based stations, buoys and ships, the variability is not surprising.

The 300 mb jet streak analysis shows that the cyclone formed beneath the upper ridge in the right exit region of a 40 m s^{-1} jet maximum located to the northwest (Fig. 3.6 a). At 0000 GMT 27 January (not shown) the low center was located directly below the wind maximum. At later times (Fig. 3.6 b,c) the storm center was below the left exit jet quadrant. Because the polar low formed beneath the right convergent exit region of the upper-level jet, it is unlikely that the initial surface development was directly related to the jet streak.

Satellite imagery during the life of this cyclone is presented in Cook (1983). This imagery shows that the polar low formed in the vicinity of disorganized middle and high-level clouds in a generally convective flow. The system rapidly acquired an organized multilayered comma-shaped configuration accompanied by vigorous deep convection.

36
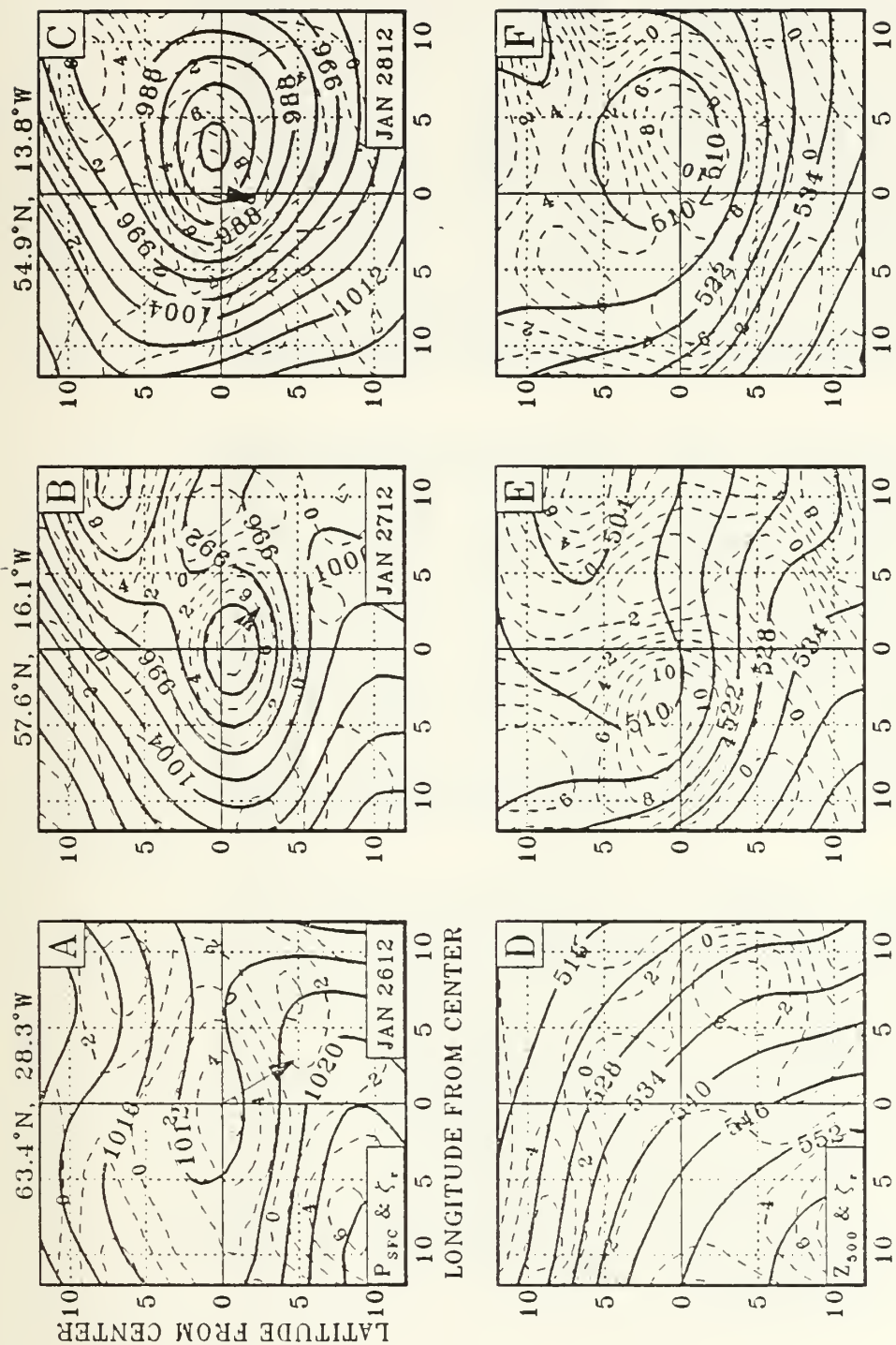
Fig. 3.4.   (a-c) As in Fig. 3.1 except for FGGE Type I
with dates indicated in lower right (2612
means 1200 GMT 26 January, 1979).

37
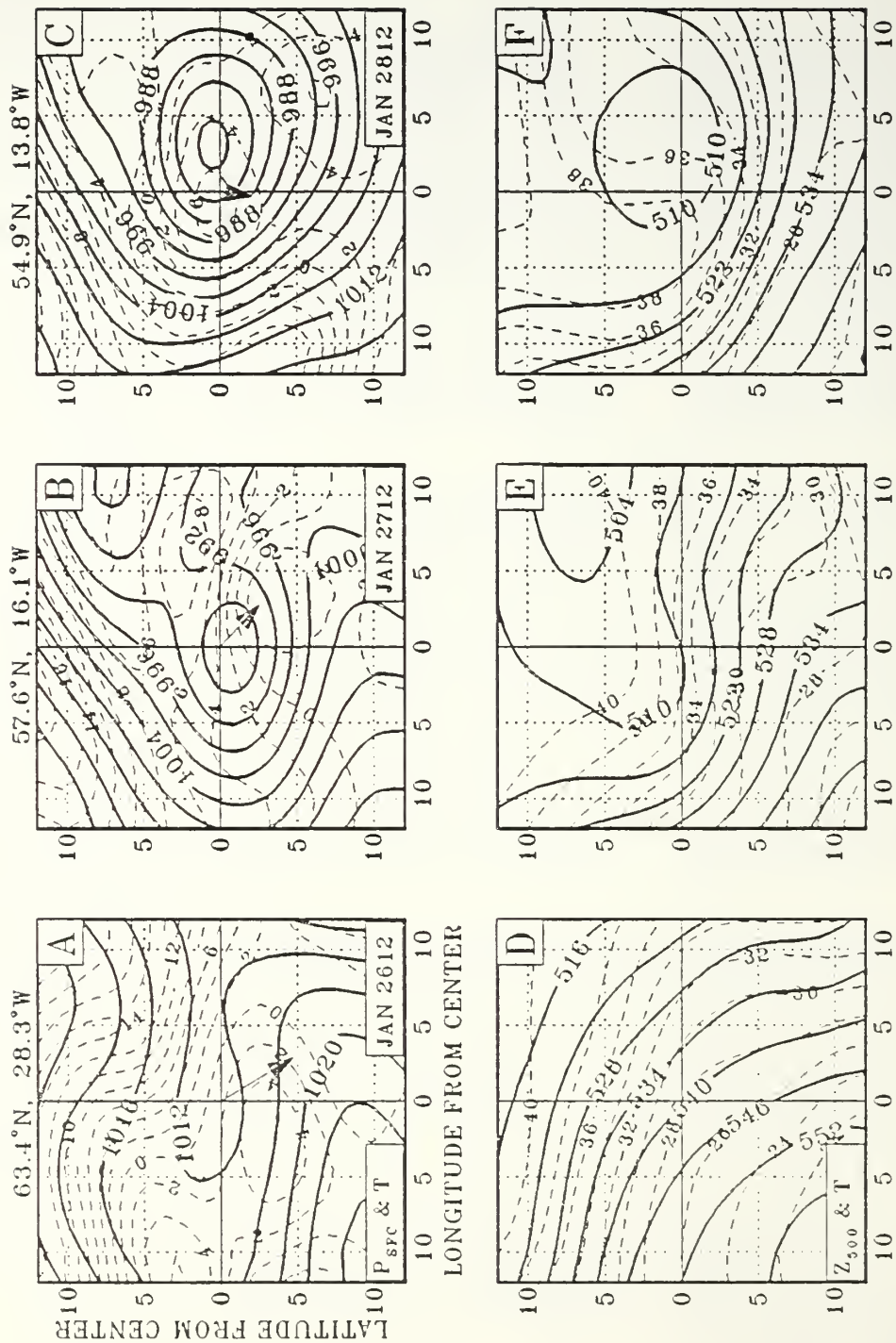
Fig. 3.5.   As in Fig. 3.3 except for FGGE Type I.

38
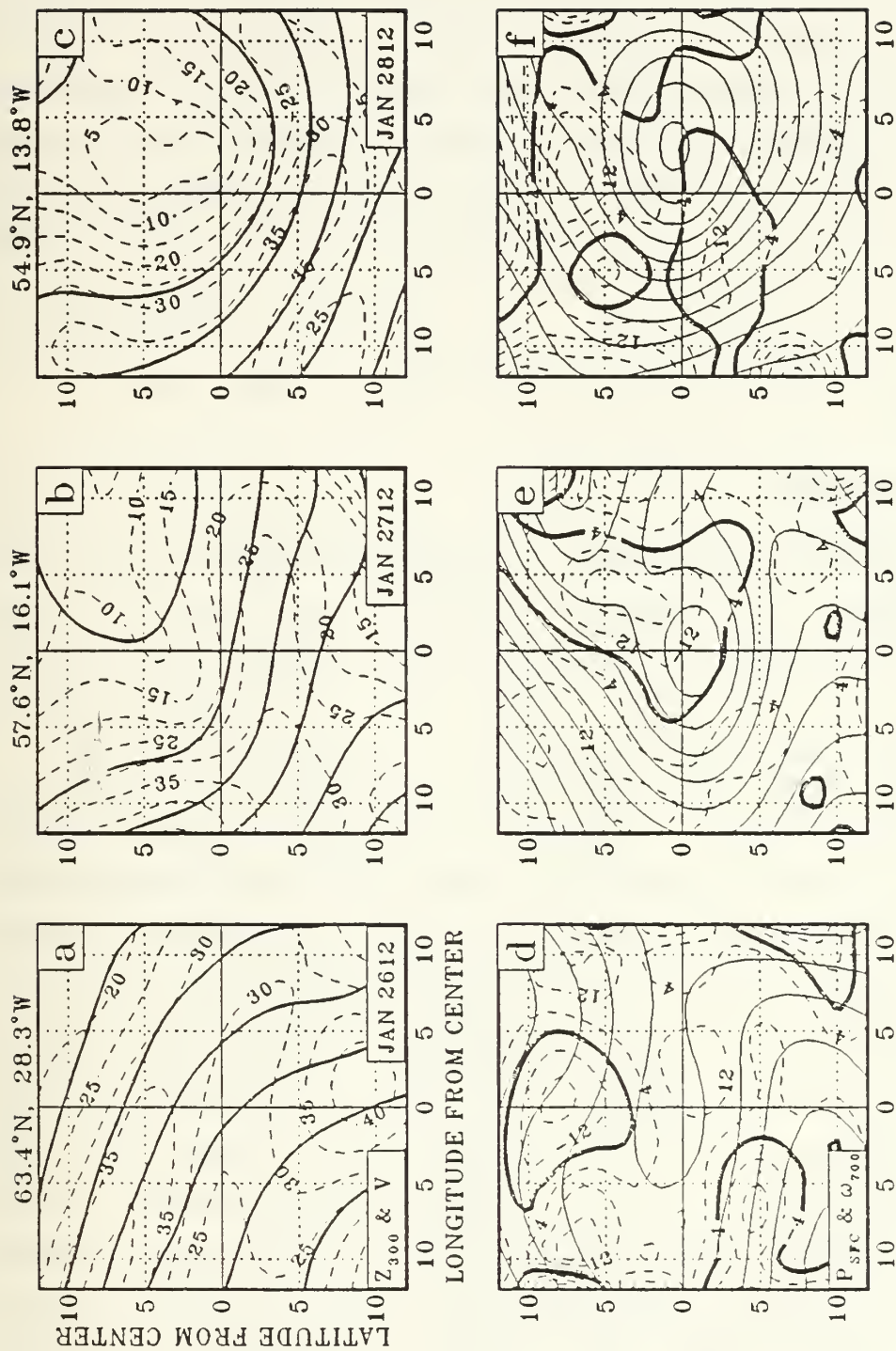
Fig. 3.6. As in Fig. 3.2 except for FGGE Type I.

39

Following maturation, the demise of the storm was accompanied by dissipation of this cloud feature.

The kinematically-derived omega fields for this storm (Fig. 3.6 d-f) are rather noisy. The characteristic comma shape and other details of the satellite cloud signature are poorly reproduced, which suggests that the FGGE level III-B analyses are only able to describe the coarse features of this polar low. At the initial time, ascent occurs about 800 km to the north of the disturbance center (Fig. 3.6 d) in conjunction with the left exit region of the upper-level jet streak in Fig. 3.6 a. Later, a broad area of ascent is located to the northeast of the surface low (Fig. 3.6 e).

3. Discussion

The synoptic features of the model-generated cyclone and the FGGE case study of Cook are similar in many respects. The essential feature which characterizes these two cyclones is that both formed under anticyclonic upper flow on the equatorward side of an upper wind maximum. These synoptic features would appear to place these cyclones in the Petterssen et al. (1962) and Petterssen and Smebye (1971) type A category. However, upper-level forcing appears to play an important role in both cases of cyclogenesis. For both cases, low-mid tropospheric frontogenetical forcing is apparent at early stages. In the FGGE example, the mass and vorticity diagnostics (presented below) showed that rapid circulation increases occurred with the incursion of the forward divergent quadrant of an upper jet streak into the budget volume (Cook, 1983). These results suggest that upper-level forcing may play a greater role in such cases than the Petterssen description would imply.

The detailed diagnostic analysis which follows will highlight many of these features. Similarities between

40

model-generated and FGGE data will demonstrate the realism of the simulations and provide further justification for analysis of simulated polar lows. Although two very distinct storms are studied, the diagnosis of similar physical processes will be regarded as strong support for the importance of that process. Differences may be due to dissimilar storm processes or may indicate inadequate representation of physical processes in the model.

B. MASS BUDGET ANALYSIS

The mass budget permits some insight into the strength of the vertical mass circulation associated with these developing polar lows. The mass budget is comprised of net horizontal convergence of mass flux which is exactly offset by vertical flux divergence. These terms are necessarily equal because the vertical transport is computed from kinematically-derived vertical velocity fields as described in the Appendix.

The mass transport is computed for nine 100 mb deep layers for a 5° latitude radius (555 km) budget volume. The maximum surface absolute vorticity is used to locate the budget volume at each time, as described in the Appendix. Instantaneous budget terms are evaluated at each data time (every 3 h for NOGAPS output and 12 h for FGGE case).

The time-section of horizontal mass flux convergence for the model-generated polar low is shown in Fig. 3.7 a. The mass unit of 9.89×10^{14} kg is the air mass contained in a 100 mb deep 5° radius budget cylinder. The lateral transport exhibits a a two-layer structure with low-level mass inflow below an outflow layer. Vertical growth of the convergent layer accompanies polar low development with a rise in the level of non-divergence (LND) from near 750 mb to 490 mb. The kinematically-derived vertical velocities (Fig. 3.7 b)

41

reflect the strength of the area-averaged mass circulation. The strongest increases occur during the first 24 h while the cyclone is located to the south of the jet, with slow strengthening thereafter.

The mass circulation has an oscillatory fluctuation superposed on the slower variations associated with the development of this polar low. This cyclic pattern is reflected in the surface pressure tendency trace (see A.2 in the Appendix) as a 12 h oscillation superposed on the slower deepening trend. This oscillation was earlier documented by Tallman (1982) who attributed the fluctuations to the presence of an external gravity wave propagating within the model. Time sections (not shown) of the zonally-averaged mass tendency showed that these waves are of meridional wavenumber one, and therefore represent a periodic transfer of mass between hemispheres. Because this "sloshing" is an artifact of the model, it was not analyzed further.

For the FGGE case, the mass circulation (Fig. 3.8 a) develops a two-layer structure similar to that for the NOGAPS case (Fig. 3.7 a). During the first 12 h of this disturbance, the mass circulation is that of an anticyclone, with convergence aloft and divergence near the surface. The omega time-section (Fig. 3.8 b) shows that the largest increase in the strength of the mass circulation occurs between 1200 GMT 26 January and 1200 GMT 27 January with further slower growth until 0000 GMT 28 January. Some of this initial increase in the vertical mass circulation occurs while the cyclone is located on the equatorward side of the jet streak. Unlike the NOGAPS example where the mass circulation remains strong throughout the development, the FGGE case exhibits a decline in the strength of this circulation. This decrease is supported by weakening of the cloud features in the satellite imagery toward the end of the sequence.

LATERAL MASS FLUX CONVERGENCE
(9.89×10^{14} kg per day)

ω (mb per hour)
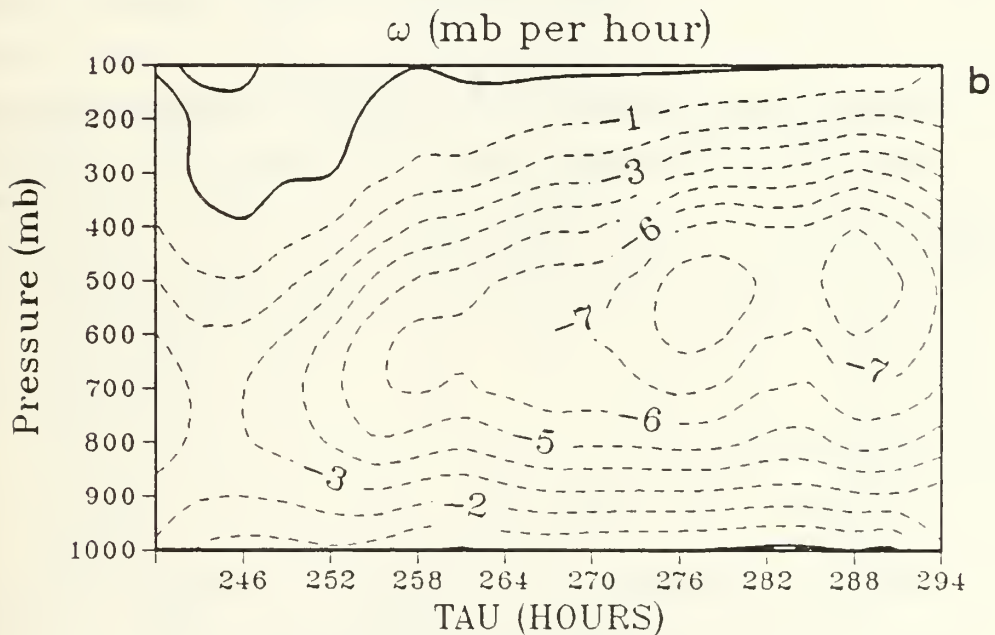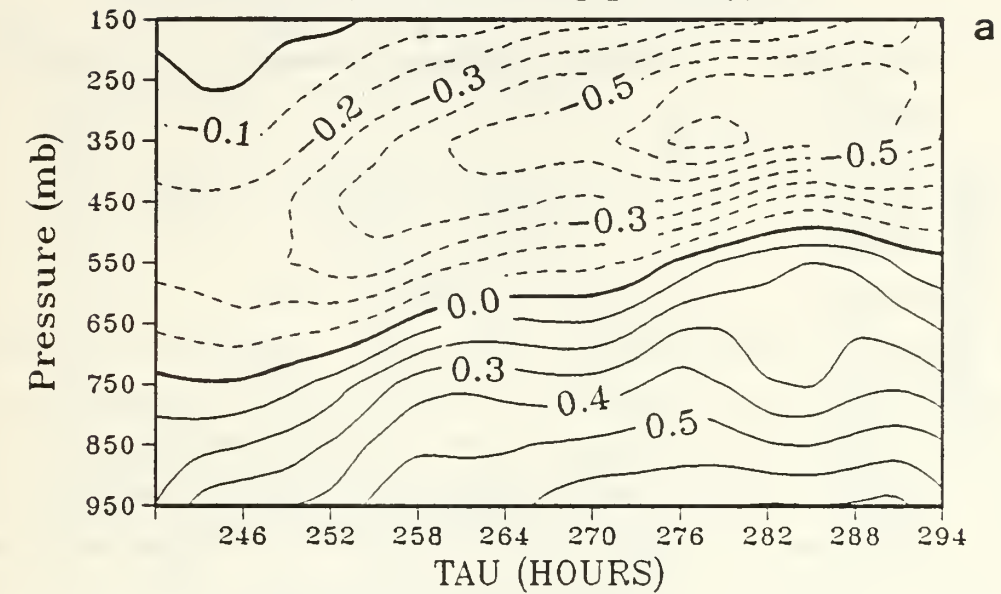
Fig. 3.7.   (a) Time evolution of lateral mass flux convergence in 5° latitude radius volume for NOGAPS Type I. Positive (solid) values indicate inflow. (b) Area-averaged vertical p-velocity (mb h^{-1}). Positive (negative) values are solid (dashed).

43

LATERAL MASS FLUX CONVERGENCE
(9.89 x 10^{14}kg per day)

ω (mb per hour)
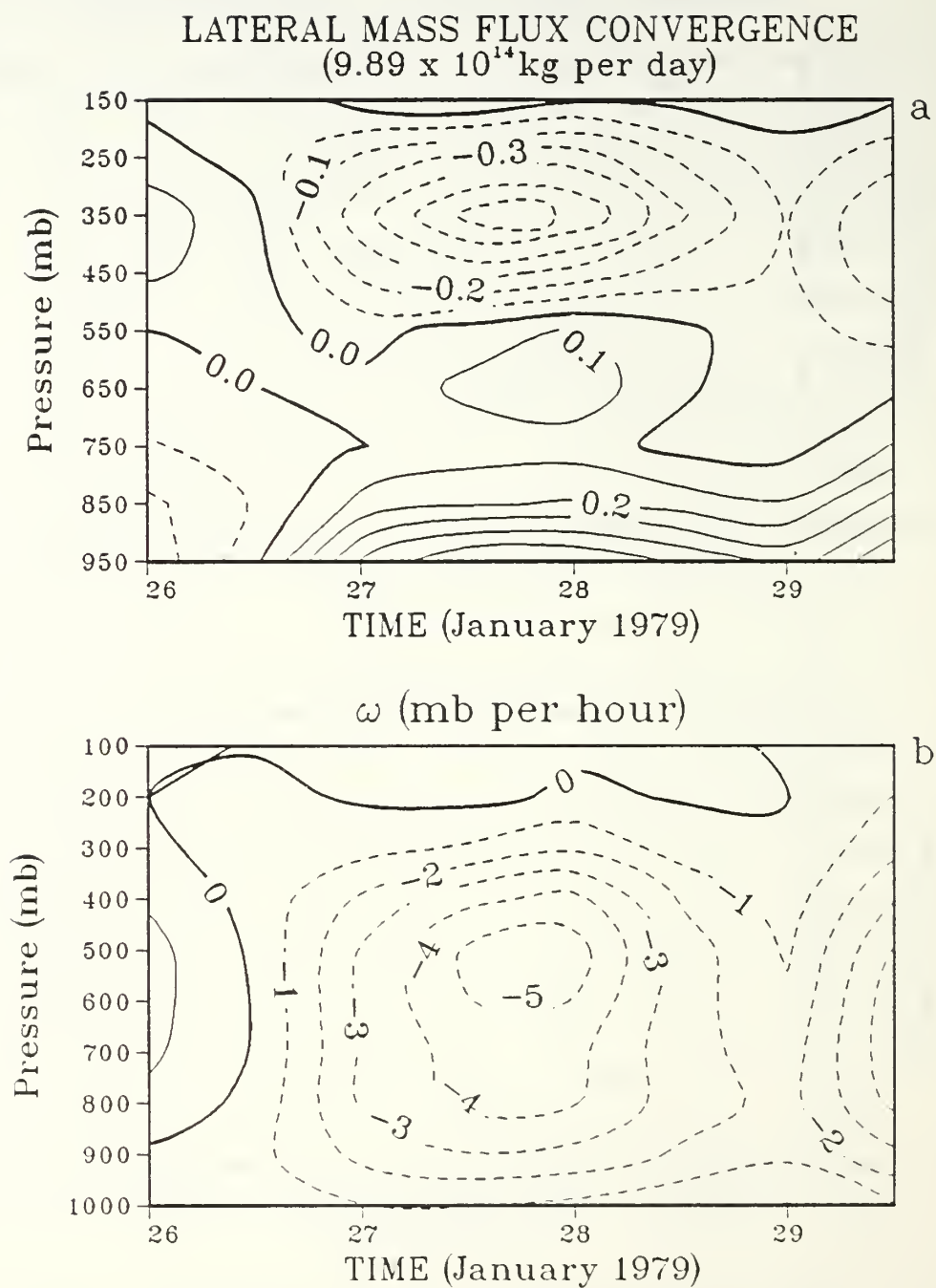
Fig. 3.8. As in Fig. 3.7 except for FGGE Type I.

C. VORTICITY ANALYSIS

The quasi-Lagrangian isobaric inviscid vorticity equation

$$\frac{\delta}{\delta t}(\zeta_r + f) \quad = \quad -(\mathbf{V} - \mathbf{C}) \cdot \mathbf{V}(\zeta_r + f) \quad - \quad \omega \frac{\partial \zeta_r}{\partial p} +$$

$$\qquad\quad A \qquad\qquad\qquad\quad B \qquad\qquad\qquad\qquad C$$

$$(\zeta_r + f)\mathbf{V} \cdot \mathbf{V} + \left(\frac{\partial u}{\partial p}\frac{\partial \omega}{\partial y} - \frac{\partial v}{\partial p}\frac{\partial \omega}{\partial x}\right) \qquad\qquad (3.1)$$

$$\qquad\quad D \qquad\qquad\qquad\qquad E$$

relates storm-relative changes in absolute vorticity (term A) to horizontal and vertical vorticity advection (terms B and C), divergence (term D) and twisting (term E) sources. This equation is used to specify the source/sink terms (terms D and E) for the vorticity budget. The budget equation is obtained by integrating each term in (3.1) over the 5-degree radius budget volume which is enclosed between pressure levels 10 mb apart, and partitioning the horizontal and vertical fluxes into mean and eddy components, as described in the Appendix. The budget terms are calculated by replacing f in (A.1) by the absolute vorticity, and S by terms D and E from (3.1). The terms in (3.1) are also calculated directly and displayed on horizontal plots.

1. Simulated Case

The vertical time-section of quasi-Lagrangian absolute vorticity tendency for the NOGAPS data is shown in Fig. 3.9. Initially, there is weak anticyclogenesis aloft. Cyclogenesis initially occurs below 600 mb but spreads rapidly throughout the depth of the troposphere. While much of the increase in the mass circulation occurs during the first 24 h, the largest vorticity increase occurs near 300 mb at 285 h. These rapid vorticity increases occur as the

300 mb jet crosses to the south of the surface low center.
These vorticity changes are described by the various trans-
port and internal generation processes which are evaluated
in the vorticity budget described below.

$$\delta\zeta/\delta t$$
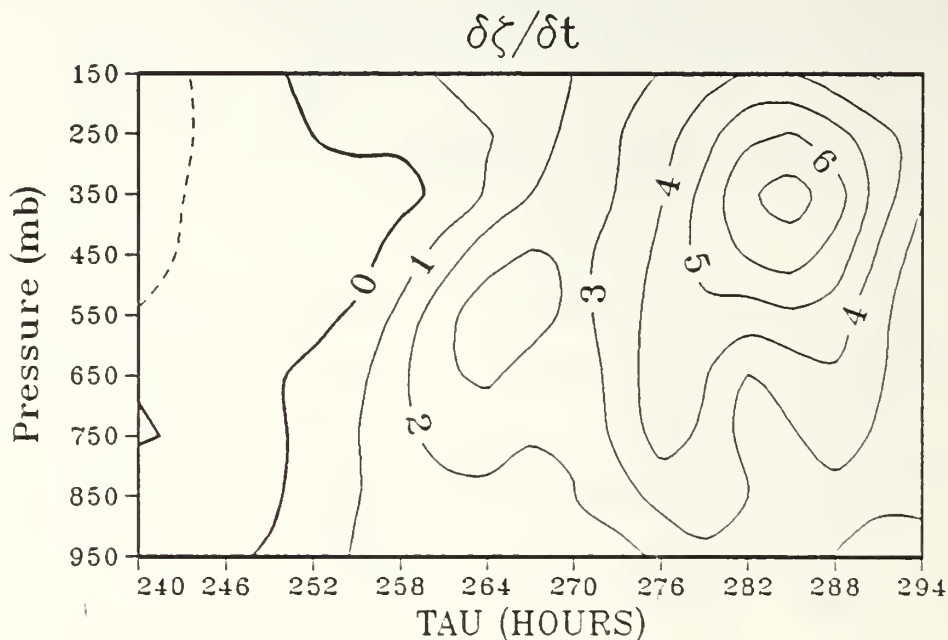
Fig. 3.9.   Time evolution of quasi-Lagrangian absolute
            vorticity tendency $(10^{-5}\ s^{-1})$ for NOGAPS
            Type I.

        Vertical profiles of vorticity budget results for
three stages of polar low development are presented in Fig.
3.10. A budget term is positive when it represents a process
which produces   a vorticity   increase.   The   observed
quasi-Lagrangian tendency of absolute vorticity (top graphs)
is equivalent to the sum of vorticity changes due to the six
terms graphed below, plus a residual. The mean and eddy
terms in Fig.   3.10 d-i are the mean and eddy flux conver-
gence terms computed from (A.1). The horizontal eddy term is
approximately equivalent to the area-averaged advection of
absolute vorticity. Equality occurs when the convergence and
mean horizontal vorticity flux convergence terms are equal

46

(see equation A.21 in the Appendix). This is evidently the case here, except near the surface. Other vorticity budget studies in which divergence and vorticity advection partitions were explicitly computed (e.g. Calland, 1983; Cook, 1983) yielded lateral eddy flux and vorticity advection partitions within a few percent in the mid and upper troposphere.

The existence of small negative residuals indicates a vorticity sink not specified in (3.1). Model diffusion processes and surface friction probably account for these residuals, as suggested by the opposite signs exhibited by the relative vorticity and the budget residual (Fig. 3.10 a-c). In anticyclonic areas, diffusion acts as a vorticity source by eroding the negative vorticity. The smoothing algorithm used prior to interpolation acts as a low-pass filter, and would therefore represent an additional diffusive effect. The large negative residual at final stages of this storm (Fig. 3.10 c) occurs in conjunction with large relative vorticity, and thus appears to be the result of model diffusion processes. The budget is closed to an acceptably small residual, which strengthens conclusions regarding the relative importance of the various vorticity generation or destruction processes. This further reinforces the justification for use of model output as data, since observational studies using larger budget volumes with time averaging have yielded larger residuals (e.g. DiMego and Bosart, 1982; Cook, 1983; Chen and Bosart, 1979).

The budget results for the first 21 h of development suggest that the initial anticyclogenesis aloft is associated with upper-level divergence that is offset by a small positive horizontal eddy term (Fig. 3.10 d). Although the vorticity advection at the initial time is small (see Fig. 3.1 d), the positive eddy term in Fig. 3.10 d results from the amplification of the 500 mb wave that occurs during this

47
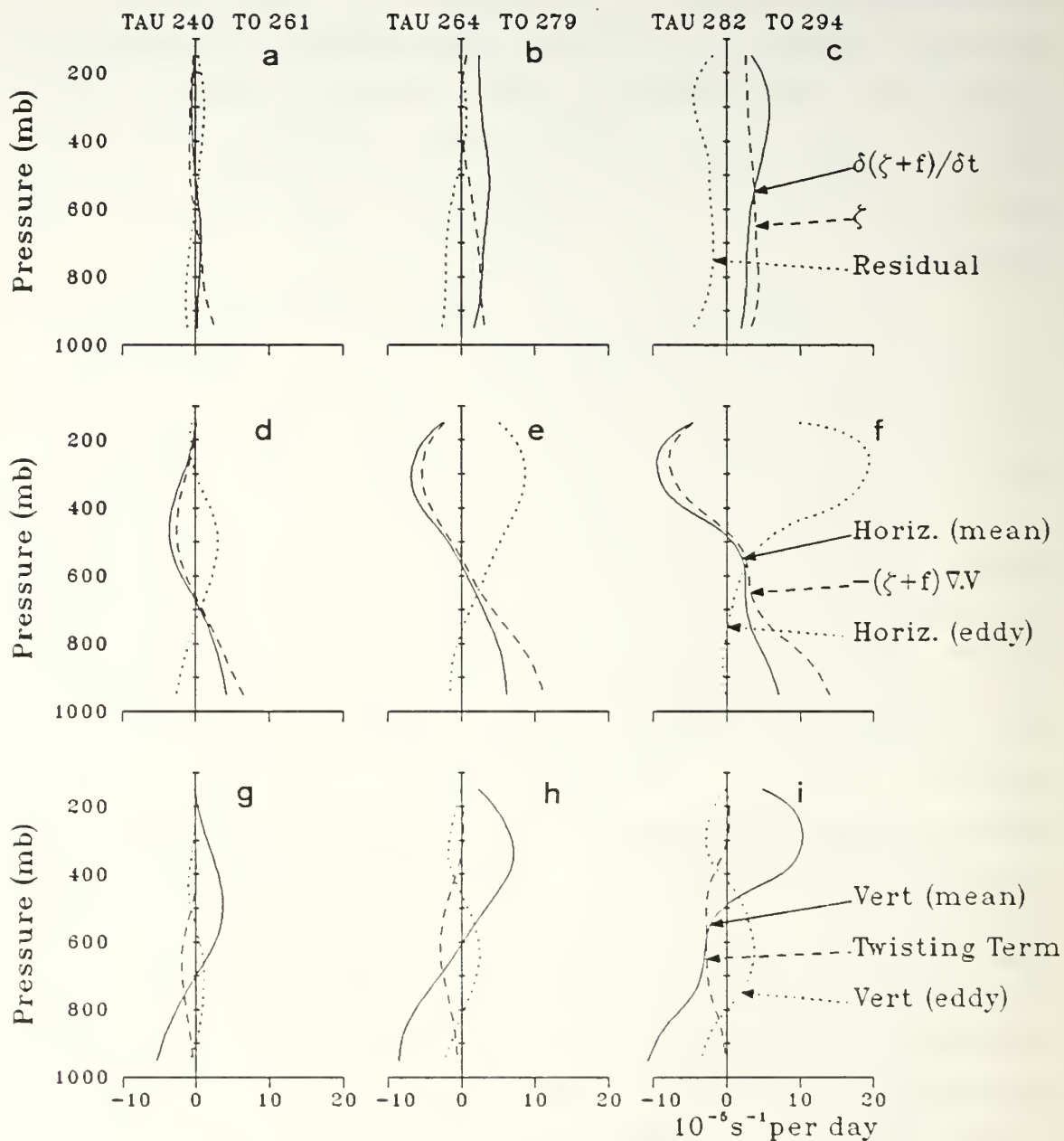
Fig. 3.10. Vorticity budget terms for same volumes as in mass budget for NOGAPS Type I. Budget terms (described in text) are indicated in the legend on the right side. Times are indicated at the top of the figure.

48

21 h period (see Fig. 3.1 e). This growing upper-level wave
is coupled with the developing surface disturbance.
Increasing convergence in the lower troposphere gives
vorticity production there, but this is opposed by a
negative horizontal eddy term which arises from the initial
asymmetry of the low. Except near the surface, the net
contribution from the mean horizontal and vertical flux
convergence terms (Fig. 3.10 d,g) is negligible.

At later stages of development, absolute vorticity
generation becomes significant at all levels. Near the
surface, vorticity generation occurs as a result of an
increasing convergence source term and is countered by the
effects of friction, and vertical eddy flux in the volume.
The horizontal eddy flux term becomes negligible below 700
mb, which reflects the increasing symmetry of the low-level
disturbance, and the vertical orientation of the vorticity
features in this layer. Friction is not calculated explic-
itly in this formulation. A frictional sink is inferred from
the budget residual (Fig. 3.10 b,c), which is predominantly
negative for the surface layer. There is a net loss of
low-level vorticity by the mean circulation, with vertical
export exceeding the mean horizontal inflow. However, this
loss is not sufficient to cancel the large gain from conver-
gence. As cyclogenesis occurs, convergence becomes more
efficient in producing vorticity growth due to the growing
absolute vorticity coefficient in the convergence term. As
the LND increases, vorticity generation by convergence
increases in vertical extent. The growth of surface
vorticity due to low-level convergence was noted in other
quasi-Lagrangian vorticity budget studies (Chen and Bosart,
1979; DiMego and Bosart, 1982; Calland, 1983; Cook, 1983;
Bosart and Lin, 1984; Wash and Calland, 1985).

Aloft, the strong cyclogenesis observed near the end
of the sequence is consistent with the rapid growth of the

horizontal eddy term (PVA) that is partially offset by the divergence sink term (Fig. 3.10 e,f). The twisting term and vertical vorticity transport are important only in the middle troposphere. Vorticity generation occurs as a result of vertical eddy flux, and is offset by twisting effects (Fig. 3.10 g-i). Upward motion ahead of and subsidence behind the budget volume center result in considerable horizontal gradients of omega, especially near the LND where omega is largest. Thus, it is in this middle layer that the twisting term is important. DiMego and Bosart (1982) computed quasi-Lagrangian budgets for the transformation of tropical storm Agnes (June, 1972) into an extratropical cyclone. They also found generation by vertical advection offset by twisting. A similar relationship between these terms was also noted by Calland (1983) and Chen and Bosart (1979) for cases of maritime extratropical cyclogenesis which occurred during outbreaks of cold continental air. It would be expected that the twisting term would be a rather important vorticity sink in the development of small-scale disturbances in a highly sheared environment. Because this term depends on the horizontal gradient of vertical velocity, it apparently acts to damp small-scale baroclinic disturbances in the wind field.

Spatial distributions of the vorticity generation terms in (3.1) for 500 mb are illustrated in Fig. 3.11. The quasi-Lagrangian vorticity tendency (g-i of this figure) is the sum of vorticity advection (a-c), convergence (d-f), vertical advection and twisting. Because vertical advection and twisting effects are smaller in magnitude than the other terms and offset one another to a high degree, they are not included in Fig. 3.11.

At the initial time, the pattern of vorticity tendency (Fig. 3.11 g) in the vicinity of the cyclone is determined primarily by the convergence term (Fig. 3.11 d).
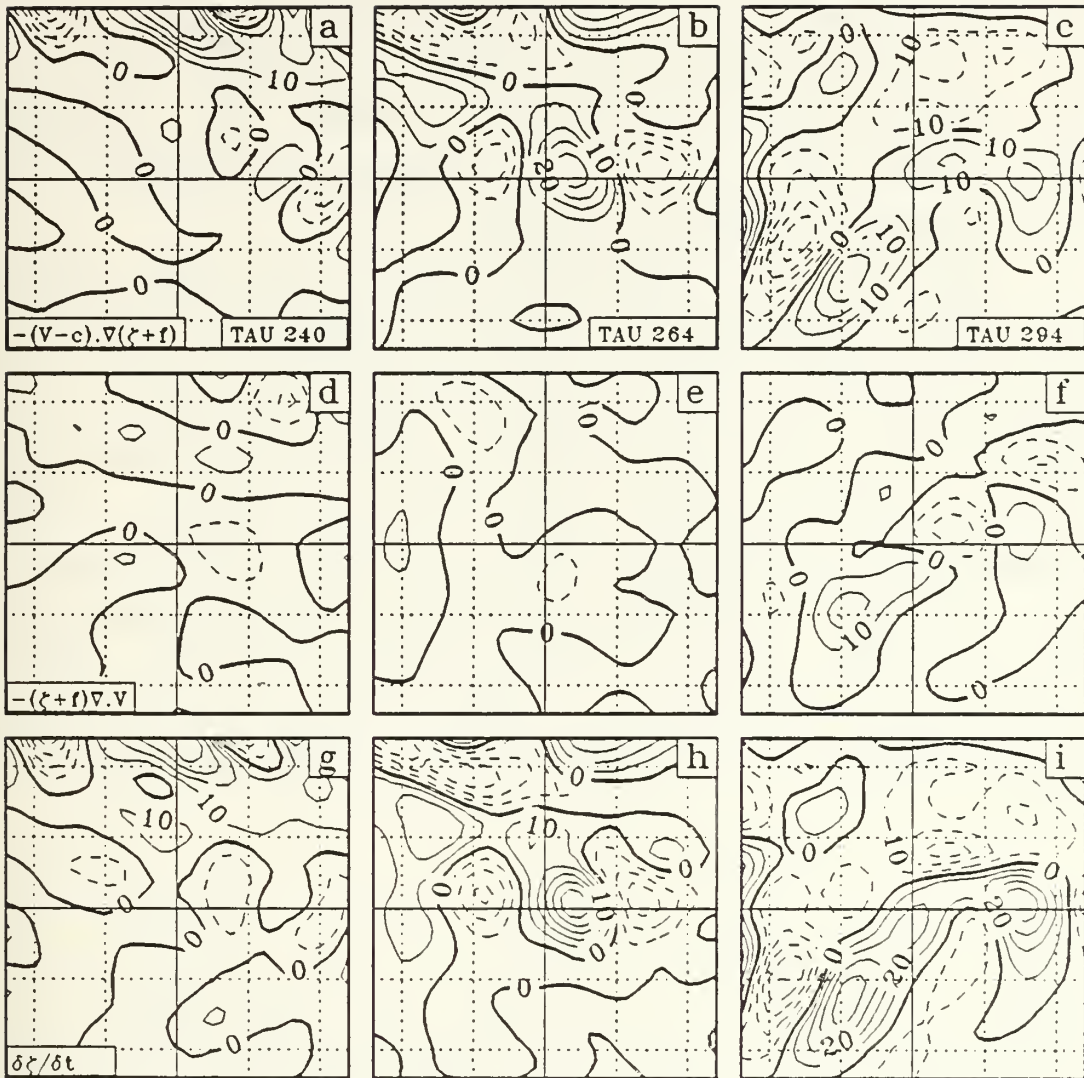
Fig. 3.11. Vorticity equation terms at 500 mb for NOGAPS
Type I. (a-c) absolute vorticity advection;
(d-f) convergence term; (g-i) quasi-Lagrangian
absolute vorticity tendency. Format as in Fig.
3.1 except axis labels and center coordinates
omitted for clarity. Units are 10^{-5} s^{-1} per
day. Heavy solid line is zero contour, and solid
(dashed) lines are positive (negative) values.

Weak vorticity advection (Fig. 3.11 a) reflects the initially undisturbed nature of the upper flow and confirms this cyclone as Type I. The patterns of divergence (convergence) occur in conjunction with the upward (downward) vertical mass circulation east (west) of the disturbance center (Fig. 3.2 d), and are largely unrelated to the initial vorticity advection pattern.

The initial pattern of positive vorticity tendency to the west and negative to the east results in a vorticity pattern that tilts westward with height and leads to the development of a vorticity gradient along the upper flow. As a result, vorticity advection increases rapidly to become the dominant term (Fig. 3.11 b). At this stage, it is not possible to say whether this cyclone is Type I or II because it is developing in conjunction with an amplifying upper-level wave. This emphasizes an advantage of model-generated data that was noted earlier - namely that we can trace a weak disturbance back in time to a point where there is no PVA aloft.

The PVA maximum in Fig. 3.11 b is highly correlated with the upward vertical velocity maximum in Fig. 3.2 e. Since the thermal gradient at 500 mb (Fig. 3.3 e) at this location is weak, it is unlikely that the upward motion results from warm advection. The amplification of the upper waves and the growth of the secondary mass circulation appear to be mutually cooperative processes at early stages of cyclone development.

Because vorticity advection occurs downstream from the vorticity extrema, subsequent centers of vorticity tendency (Fig. 3.11 h) are progressively displaced downstream. This tendency eventually leads to an eastward extension of the cyclonic vorticity maximum and pushes the ridge well ahead of the cyclone center (see Fig. 3.1 f).

By the end of the period, vorticity generation (Fig. 3.11 i) occurs in two distinct lobes to the east and south-west. The vorticity advection term contributes most to the generation. The eastern lobe occurs in conjunction with upward motion in that area (Fig. 3.2 f). Convergence at 500 mb (Fig. 3.11 f) in this region is probably a result of the increased depth of the convergent layer at this time (Fig. 3.7 a) since divergence occurs at 300 mb (not shown). The area of positive vorticity tendency to the southwest of the surface low is the result of upper-level convergence implied by the subsidence in that location (see Fig. 3.2 f). This tendency results in the southwesterly extension of the vorticity maximum in Fig. 3.1 f. PVA is very efficient in maintaining this lobe, because it occurs near the upper wind maximum. The area of weak ascent ahead of this region results in an area of low-level convergence to the south of the surface low center. This convergence is responsible for the formation of the secondary vorticity disturbance "w" in Fig. 3.1 c.

2. FGGE Case

The relative vorticity tendency (Fig. 3.12) exhibits large increases throughout a deep layer centered on 0600 GMT 27 January, with decreasing vorticity after 1200 GMT 28 January. The strongest cyclogenesis occurred during the period when the surface cyclone crossed to the poleward side of the jet axis.

Vorticity budgets for the FGGE case are presented in Fig. 3.13. During the first 12 h, the calculated budget terms do not account for the low-mid tropospheric cyclo-genesis. The budget terms at this early stage indicate convergence aloft above low-level divergence, which are consistent with the subsidence during this period (Fig. 3.8 b). The large budget residual indicates that an additional
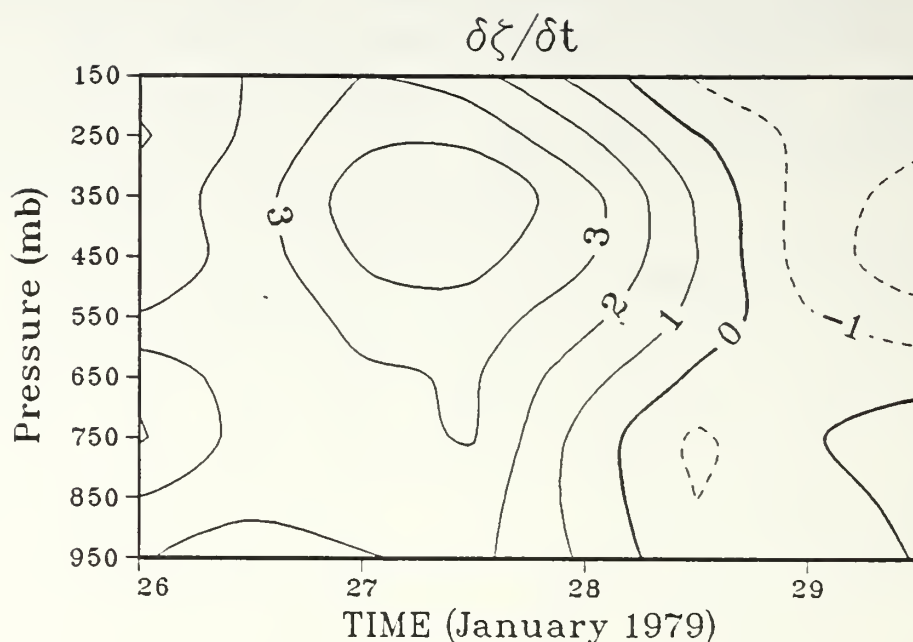
Fig. 3.12. As in Fig. 3.9 except for FGGE Type I.

vorticity source is needed to explain the positive vorticity
tendencies which occur in conjunction with a vorticity sink
due to divergence and eddy transport losses. This residual
possibly arises from data inconsistencies. During the first
12 h of development, the elevated terrain of Greenland is
included in the western part of the budget area. In winter,
radiational cooling results in a cold layer near the
surface. The surface winds in this layer are strongly decou-
pled from the synoptic pressure patterns and are representa-
tive of a very shallow surface layer. Over elevated terrain,
the ECMWF analysis extrapolates to pressure levels below the
topography. Thus, the terrain-dependent surface wind infor-
mation may be applied to a much deeper layer than is appli-
cable, and this may account for the large budget residuals,
at least below about 800 mb.
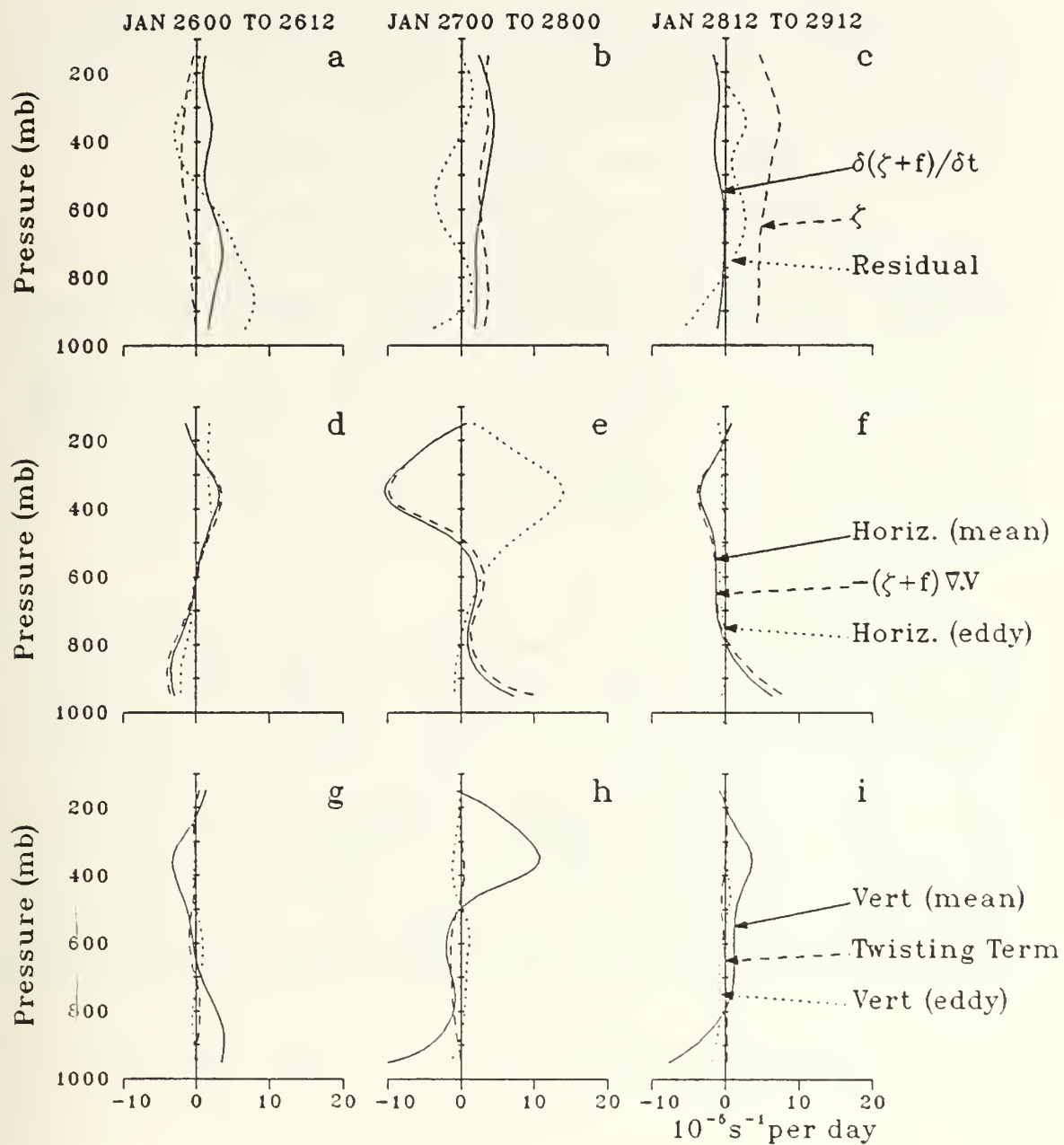
Fig. 3.13. As in Fig. 3.10 except for FGGE Type I.

55

Between 0000 GMT January 27 and 0000 GMT January 28, convergence near the surface causes a vorticity increase. This is offset by friction (negative residual) in the lowest layer. Generation aloft is from PVA and is partly offset by divergence. During the final 24 h of the sequence, decreasing vorticity occurs throughout the whole troposphere. Aloft, this is largely a result of a much reduced eddy flux term which is caused by the decreasing vertical tilt of the system at this time (see Fig. 3.4 c, f). Near the surface, decreasing low-level mass inflow inhibits further generation. As for the NOGAPS case, the horizontal and vertical mean flux convergence terms (Figs. 3.13 d-f and g-i) are equal and opposite so the net effect of these terms is negligible.

Horizontal depiction of the terms in (3.1) at 500 mb is given in Fig. 3.14. Initially, weak NVA occurs directly above the surface low (Fig. 3.14 a), which shows that this is a Type I polar low not initiated by PVA. The area of PVA to the east is associated with the vorticity minimum near that location (see Fig. 3.4 d). Generation by convergence occurs above and to the northeast of the low center (Fig. 3.14 d). The area of strong divergence and PVA to the north of the center is associated with the left exit region of the jet streak to the northwest (Fig. 3.6 a). Since the jet-related divergence is located about 800 km from the surface center, it is unlikely to be responsible for genesis of this storm.

At 1200 GMT 27 January, the strongest positive vorticity tendency occurs to the south and west of the center (Fig. 3.14 h), with negative tendencies to the north and east. This is consistent with both the southward movement of the upper jet streak, and the growing amplitude of the 500 mb trough/ridge in Fig. 3.4 e. As the cyclone later occludes, the largest positive tendency (Fig. 3.14 i) occurs
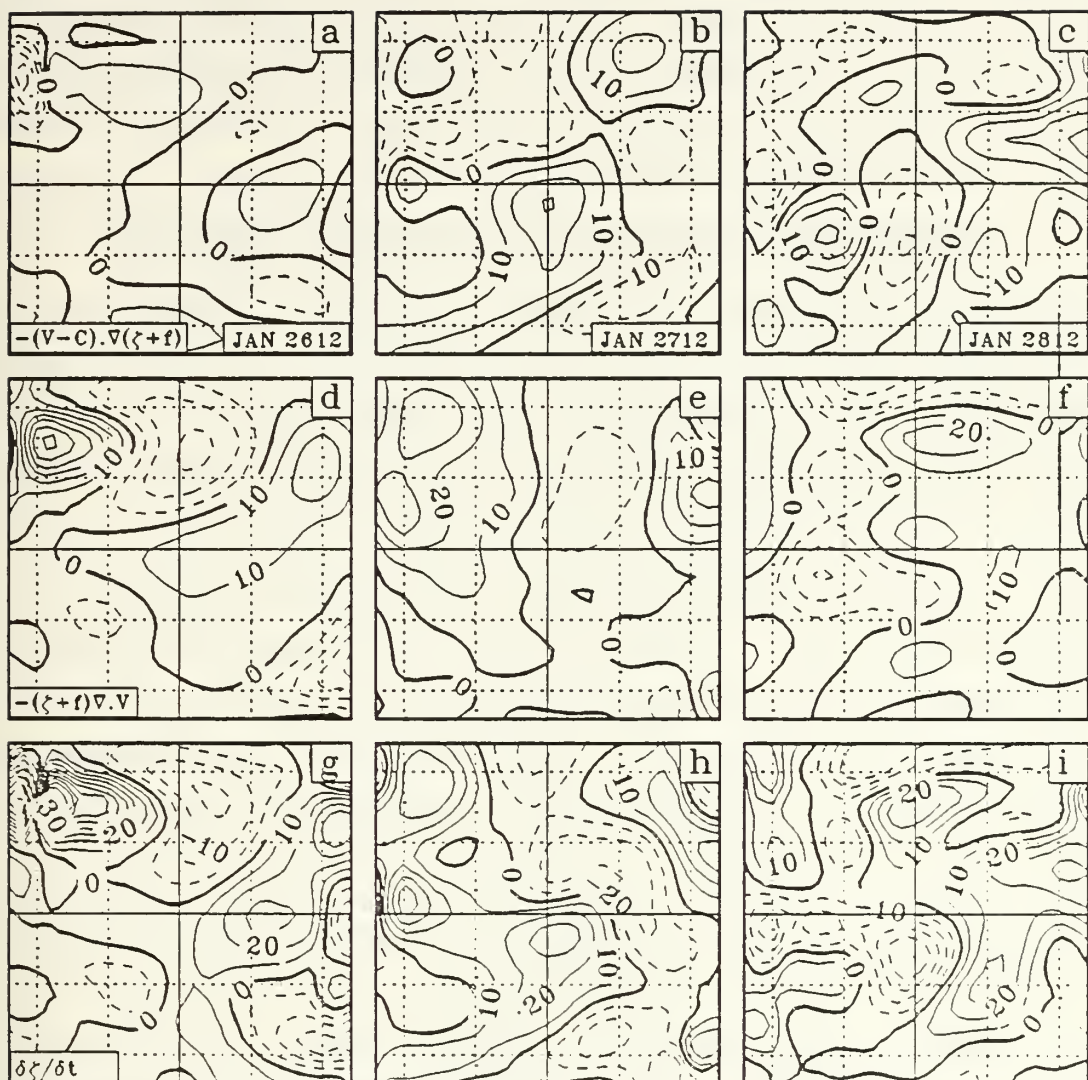
Fig. 3.14. As in Fig. 3.11 except for FGGE Type I.

in lobes to the east and the south of the low center (note that the center of Fig. 3.14 at 1200 GMT 28 January is located well to the west of the surface low center in Fig. 3.4 c). This is similar to the final vorticity tendency pattern for the NOGAPS case in Fig. 3.11 i.

3. Summary and Discussion of Vorticity Analysis

The development of these two Type I cyclones has been described in terms of the various vorticity generation mechanisms. Mass circulation increases lead to vorticity generation from the divergence term. The resulting growth of upper-level perturbations causes increasing vorticity advection in conjunction with the divergent secondary circulation. Vorticity advection leads to deformation of the upper vorticity patterns. In both cases, strongest cyclogenesis aloft appears to immediately follow the time when the 300 mb jet streak first crosses to the south of the low center. Surface vorticity generation by convergence maintains the surface cyclone against the effects of frictional dissipation. The nonlinear deformation of the upper-level vorticity field appears to create an environment favorable for the next secondary cyclogenesis.

As the low develops, the growing vertical motion results in increasing upper-level divergence. From (3.1) this may be written

$$\nabla \cdot \mathbf{V} = \frac{[-(\mathbf{V} - \mathbf{C}) \cdot \nabla(\zeta_r + f) - \frac{\delta}{\delta t}(\zeta_r + f)]}{(\zeta_r + f)} \tag{3.2}$$

which neglects the twisting and vertical advection terms that were shown in the vorticity budget analysis to be small. By definition Type I polar lows form under essentially straight upper-level flow so the initial PVA is small. From (3.2), the growth of upper-level divergence is therefore balanced by decreasing vorticity. Since the

58

initial location of the polar low is in the low absolute vorticity environment of the warm side of the jet streak, the reduced denominator of (3.2) means that only slight anticyclogenesis is required to balance the mass circulation increases. Despite growth of upper-level divergence, very little PVA is initially required for vorticity balance.

The FGGE and the model-generated polar lows exhibit some differences. In the FGGE case, vorticity generation occurs throughout a deep layer during the first 24 h (Fig. 3.12). Maximum cyclogenesis coincides with the end of the strongest mass circulation increase, and decreases there-after. In the NOGAPS case, maximum cyclogenesis aloft occurs well after the initial mass circulation increase. One reason for the later cyclogenesis in the NOGAPS case is the intense downstream ridging aloft which offsets vorticity increases in the trough early in the development. Another reason is the longer period that the NOGAPS case remains in the lower vorticity environment equatorward of the upper-level jet.

The decrease of the mass circulation in the later half of the FGGE case gives rise to weakening low-level convergence and decreasing vorticity generation. In the NOGAPS case, the maintenance of the vertical mass circula-tion ensures continued vorticity generation from the nonli-near convergence source term. It will remain to be determined why the strong mass circulation persists longer in the model-generated case.

For the FGGE case, Cook (1983) showed that the most vigorous vorticity increases were associated with the incur-sion of the forward divergence quadrant of a jet streak into the budget volume (see Fig. 3.6). Initial development of this disturbance cannot be attributed to jet-related mass circulation increases, since the low formed equatorward of the jet streak (Fig. 3.6 a) under an area of weak NVA aloft. The upper-level jet streak was initially uncoupled to the

low-level disturbance. However, once the forward divergence quadrant of the jet became superposed with the surface disturbance, strong coupling and vigorous cyclogenesis occurred.

It is important to realize that the vorticity budget results do not imply a mechanism for cyclogenesis. Rather, vorticity changes are viewed in a balance context. The actual changes in vorticity reflect the continual hydrostatic adjustment of geopotential to changes in the thermal structure, which are themselves dependent on a variety of physical processes. Thus, the vorticity budget results alone are unable to yield a complete description of the cyclone development. For this reason, a diagnostic analysis of the thermal processes was also performed.

D.   THERMODYNAMIC ANALYSIS

   1.   Heat Budget Analysis

The quasi-Lagrangian budget of potential temperature relates changes in the volume-averaged potential temperature to the various heat flux convergence terms evaluated using (A.1), and to the diabatic source and sink terms. The diabatic terms arise from air-sea heat flux, radiative fluxes and condensational heating. In terms of potential temperature, θ, the thermodynamic equation is

$$\frac{\delta\theta}{\delta t} \;=\; -(\mathbf{V}-\mathbf{C})\cdot\nabla\theta \;-\; \omega\,\frac{\partial\theta}{\partial p} \;+\; (\frac{1000}{p})^{R/C_p}\;\frac{\dot{Q}}{C_p} \qquad\qquad (3.3)$$

where $\dot{Q}/C_p$ is the total diabatic heating rate, which is specified as a model output variable. Therefore, it is possible to specify completely the model heat budget, with budget residuals representing truncation and interpolation errors only.

Vertical profiles of the heat budget terms for the NOGAPS case are graphed in Fig. 3.15. The calculations are applied to the same budget volumes as the mass and vorticity budgets. The budget is computed by replacing f in (A.1) by potential temperature. The diabatic source term is specified as the last term in (3.3). The quasi-Lagrangian potential temperature tendency (Fig. 3.15 a-c) is equal to the sum of the net mean and eddy flux convergence terms, and the total diabatic heating (Fig. 3.15 d-f), plus the budget residual. The horizontal and vertical components of the net eddy partition, and the cumulus heating (part of the total heating) are included for convenience as g-i of this figure. The horizontal and vertical components of the net mean heat flux convergence are each an order of magnitude larger (100°K /day) than the graphed terms, and are approximately equal and opposite. Therefore, only their sum is presented.

The residual term is generally small relative to the leading terms. However, large changes in the vertical gradient of potential temperature near the tropopause cause systematic errors in the vertical interpolation of temperature from sigma to pressure surfaces. The erroneous theta values lead to budget residuals that are highly correlated with the large flux convergence term (compare the residual and the net mean flux convergence profiles in Fig. 3.15). Negligible error is introduced from interpolation of the momentum terms because the mass circulation is balanced to high precision at each gridpoint.

At early stages of polar low development, potential temperature changes are slight (Fig. 3.15 a). However, as the cyclone grows, net cooling occurs (Fig. 3.15 b,c) as the low moves toward higher latitudes. This cooling is consistent with the rapid cyclogenesis aloft later in the development (Fig. 3.9). The largest terms in the heat budget are diabatic heating and the approximately equal and opposite
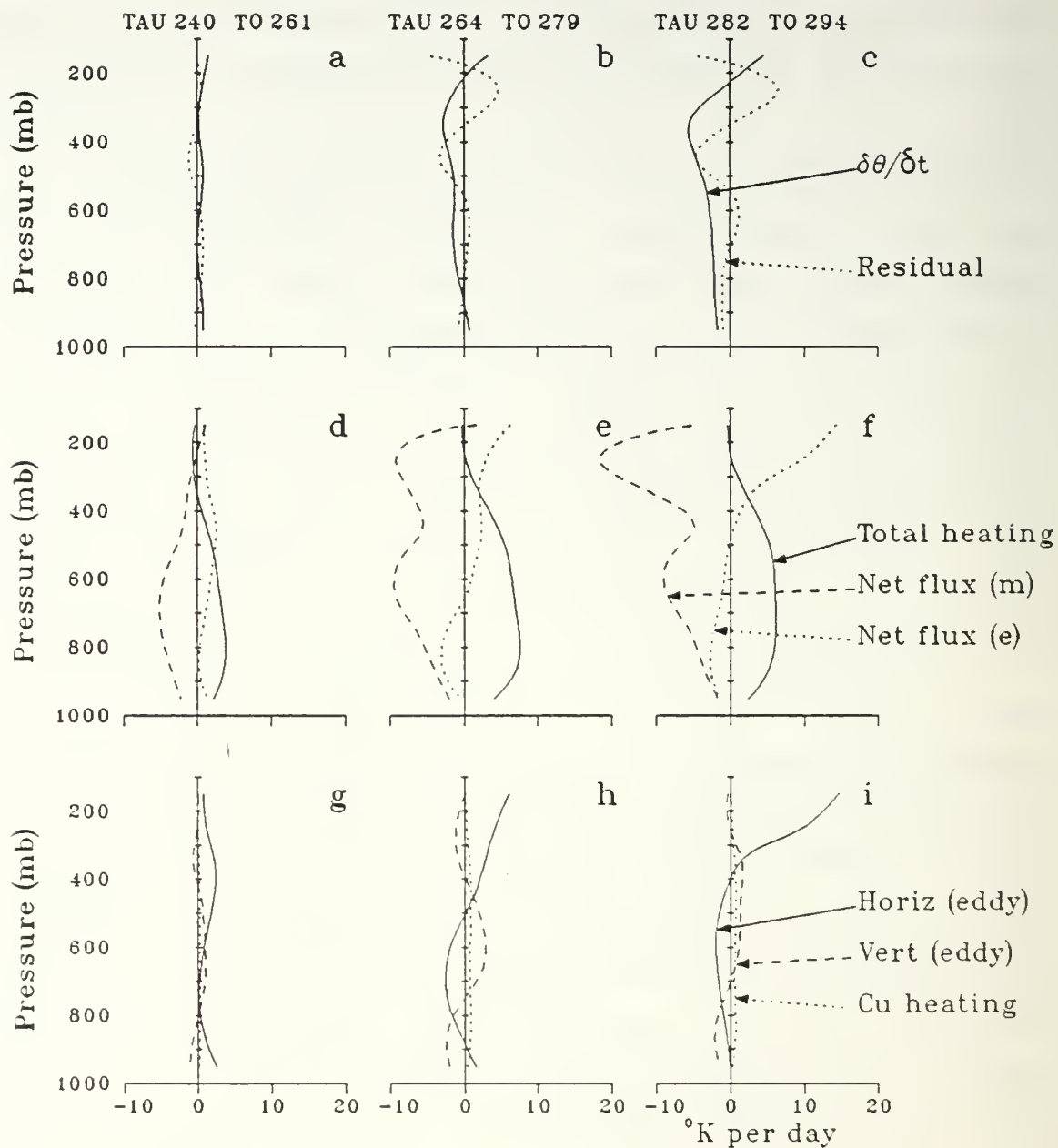
Fig. 3.15. Heat budget terms for NOGAPS Type I. Format as in Fig. 3.10.

adiabatic cooling that is associated with the mean mass circulation (Fig. 3.15 d-f). Diabatic heating arises primarily from condensation and latent heat release in ascending air.

Compared with the two leading terms, the potential temperature tendencies, and horizontal and vertical advection (eddy terms) are small in this area-averaged setting, except near the tropopause. The horizontal eddy term is small, since the 5° latitude radius budget area includes both strong cold and warm advection. To relate thermodynamic terms to synoptic features of this developing storm, heat budget terms are depicted in a horizontal format in the next subsection.

2.   Thickness Tendency Analysis

Maintenance of hydrostatic conditions is an important physical constraint in the atmosphere, and is guaranteed in the numerical model. Temperature increases (decreases) in an atmospheric column must be accompanied by increasing (decreasing) geopotential thickness for the layer. For example, net temperature decreases in the column above the developing polar low observed in Fig. 3.15 c are compatible with the vorticity tendency profile for the same time period (Fig. 3.10 c), which indicates stronger cyclogenesis aloft compared to that near the surface.

To gain more insight into the relative importance of the individual thermodynamic processes in polar low development, the terms in the quasi-Lagrangian thickness tendency equation have been evaluated as follows:

$$\frac{\partial h}{\partial t} = \int_{500}^{900} [-(\mathbf{V} - \mathbf{C}) \cdot \nabla T + (\frac{\alpha}{C_p} - \frac{\partial T}{\partial p})\omega + \frac{\dot{Q}}{C_p}] d(\ln p) \qquad (3.4)$$

$\qquad$ A $\qquad\qquad\qquad$ B $\qquad\qquad\qquad$ C $\qquad\qquad$ D

The layer below 500 mb was chosen for this calculation because it is most relevant for polar low development. Also, interpolation errors in the temperature values are larger aloft. An average potential temperature increase of 1°K for this layer corresponds to a thickness increase of approximately 15 gpm. The quasi-Lagrangian correction to the thermal advection (term B) is employed. The vertical advection (term C) is proportional to the product of vertical velocity and static stability. This term also will be referred to as adiabatic cooling in ascent regions (warming in descent areas). The diabatic heating (term D) is the vertical integral of the model-derived total heating. The net quasi-Lagrangian thickness change (term A) is calculated as the sum of the three terms in (3.4). Reasonable agreement was found between this sum and the explicitly calculated thickness tendency field (not shown). The latter involves evaluating time derivatives at each gridpoint. It was concluded that the sum of the three terms in (3.4) yields reliable estimates of the thickness tendency.

The thickness tendency equation analysis for the NOGAPS case extends a similar analysis by Sandgathe (1981) of this low (his case B). His analysis used the Eulerian form of the thermodynamic equation in sigma coordinates. The present technique employs the quasi-Lagrangian adjustment to the thermal advection term, and is presented in isobaric coordinates for three stages of cyclone development (Fig. 3.16).

During polar low genesis, the thermal advection patterns (Fig. 3.16 a) have a large cooling tendency to the north of the surface center. This cooling is partly offset by subsidence warming (Fig. 3.16 d). Diabatic heating (Fig. 3.16 g) and adiabatic cooling (Fig. 3.16 d) almost exactly cancel to the east and south of the development. The net effect (Fig. 3.16 j) is a tendency for the thickness
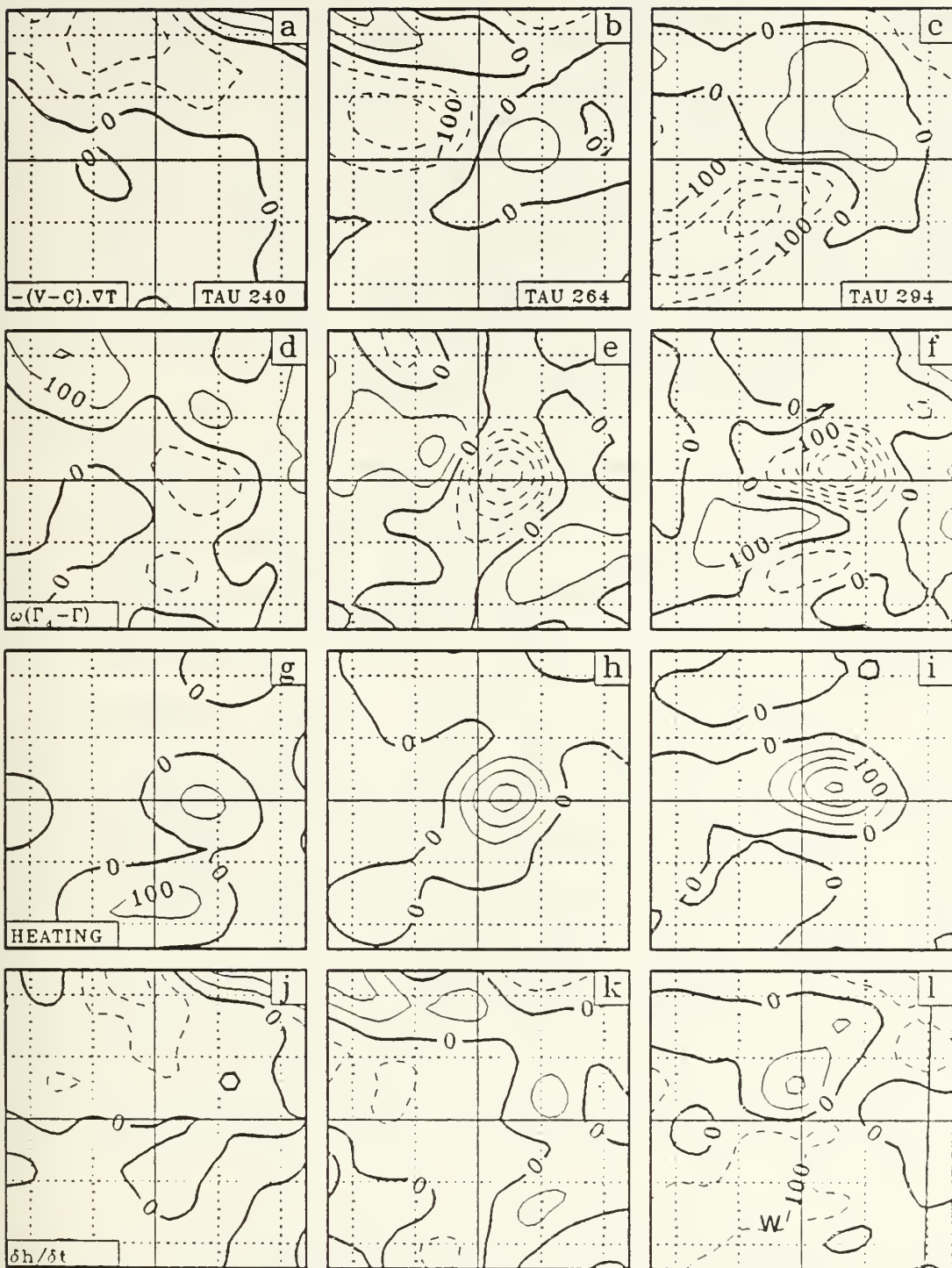
Fig. 3.16. Thickness tendency equation terms for NOGAPS
Type I. (a-c) horizontal thermal advection;
(d-f) vertical advection; (g-i) diabatic heat-
ing; (j-l) quasi-Lagrangian thickness tendency.
Format as in Fig. 3.11. Units are m day^{-1}.

65

gradient to increase in the area to the north of the surface cyclone. This frontogenetic tendency was previously noted in the synoptic discussion (see Fig. 3.3). Vertical ascent ahead of the surface disturbance appears to be initiated by weak warm advection and augmented by the latent heat release, since the fields of ascent, warm advection and diabatic heating are approximately co-located, and the net temperature tendency is comparatively small. It is this growing vertical circulation which is responsible for the vorticity generation discussed earlier.

After 24 h, a strong dipolar pattern of advective cooling to the rear and warming ahead of the low has developed (Fig. 3.16 b). In the ascent region, the net effect of diabatic heating (Fig. 3.16 h) and adiabatic cooling (Fig. 3.16 e) is slight cooling, so net thickness changes (Fig. 3.16 k) approximately reflect the contribution from thermal advection.

At the end of the sequence, the net warming patterns (Fig. 3.16 l) reflect a cyclonic rotation of earlier patterns. This rotation reflects the deformation of the thermal fields by the advection term. At this time, the trend is to eliminate the north-south temperature and geopotential gradient near the location of the polar low. This also has the effect of producing a more vertical geopotential structure. On the south side of the area of cooling in the lower left of Fig. 3.16 l, the trend is frontogenetic. This trend, and the frontolytic trend near the low center, are consistent with the movement of the jet streak to the south of the surface low center (Fig. 3.2 a-c).

Very good qualitative agreement exists between the present analysis at 264 h and that of Sandgathe (1981). The main difference is the presence of an area of strong warm advection to the northwest of the surface cyclone in the quasi-Lagrangian analysis (Fig. 3.16 b). This difference reflects the effect of storm translation.

66

Caution is required in the interpretation of the thickness tendencies in Fig. 3.16, as geopotential changes aloft and near the surface are included. In general, potential temperature tendencies are larger aloft than near the surface (Fig. 3.15 a-c), as specific volume increases with height. It follows from (3.4) that geopotential changes at 500 mb account for most of the diagnosed thickness variations. Exceptions to this may occur in regions where net low-level heating (cooling) is much larger in magnitude than that aloft. In such cases, most of the thickness increase (decrease) would be reflected by falling (rising) surface geopotential.

Comparing Figs. 3.16 k and 3.1 e, it is apparent that thickness increases (decreases) occur near the 500 mb ridge (trough). Such localized changes in the thermal structure of the troposphere tend to amplify the 500 mb trough-ridge couplet, which is compatible with the progressive increase in the variation of vorticity along the flow noted earlier (see Figs. 3.1 d and e). The increased PVA implied by this change requires an increase in the upper-level divergence between the trough and the ridge. The associated upward motion cools the layer, offsets the warm advection and opposes further amplification of the upper wave. However, release of latent heat in the ascending air largely offsets this limiting effect. Warming beneath the ridge continues and leads to further amplification of the upper wave. The progressive growth of upper-level divergence favors increasing low-level convergence, which leads to intensification of the surface cyclone. This intensification in turn strengthens the thermal advection fields and results in further amplification of the upper waves. Thus, the so-called "self-development" mechanism for cyclone intensification proposed by Sutcliffe and Forsdyke (1950) appears to apply for maritime cyclogenesis on this scale of motion as well.

67

At the initial time, the net diagnosed thickness
tendency (Fig. 3.16 j) is not conducive to self-development.
Although the thermal advection at this time produces a weak
dipolar pattern of the right phase for self-development, it
is more than offset by the effects of adiabatic cooling.
Similar results were obtained when (3.4) was evaluated for
the layer between 900 and 800 mb. Amplification of the
thermal advection dipole caused by development of the low-
level cyclone eventually results in net thickness changes of
the correct phase for self-development (Fig. 3.16 k). The
strengthening of the thermal gradient to the north of the
cyclone may also contribute to growth of the thermal advec-
tion term.

Self-development is favored by some combination of
reduced static stability, high relative humidity, and
enhanced baroclinity. In very stable air, adiabatic cooling
(term C of (3.4)) is large. Therefore, for self-development
to occur, larger contributions from thermal advection and
latent heat release are necessary to offset the limiting
effect. This is achieved when the thermal gradient is large
and the air is moist. In a lower static stability environ-
ment, the limiting effect is smaller, and self-development
will occur for smaller thermal gradients and moisture
content.

The Richardson number measures the ratio of static
stabilty to baroclinity. Therefore, a low Richardson number
is likely to be conducive to self-development. Following
Gall (1976a), a spherical Richardson number is defined as,

$$
R_i = \frac{\frac{R}{P}(\frac{\alpha}{C_p} - \frac{\partial T}{\partial p}) f_{45}^2}{[\frac{\partial u}{\partial p}(f_\phi + 2u\frac{\tan\phi}{a})]^2 + [f_\phi \frac{\partial v}{\partial p}]^2}
\tag{3.5}
$$

68

where f_{45} is the value of f at 45° N. The term involving tan⊕ in the denominator of (3.5) normalizes the vertical wind shear so that a given shear is equivalent to the same horizontal temperature gradient, irrespective of latitude. This formulation is similar to the zonal Richardson number of Gall (1976a). According to Gall (1976a) and Staley and Gall (1977), reduced Ri favors development of short-wave baroclinic disturbances. The reduced values of 700 mb Ri (Fig. 3.17) which occur slightly downstream of the disturbance center are consistent with the hypothesis that these polar lows grow through baroclinic processes. Additional areas of reduced Ri occur to the east and southwest of the low center (Fig. 3.17 c).
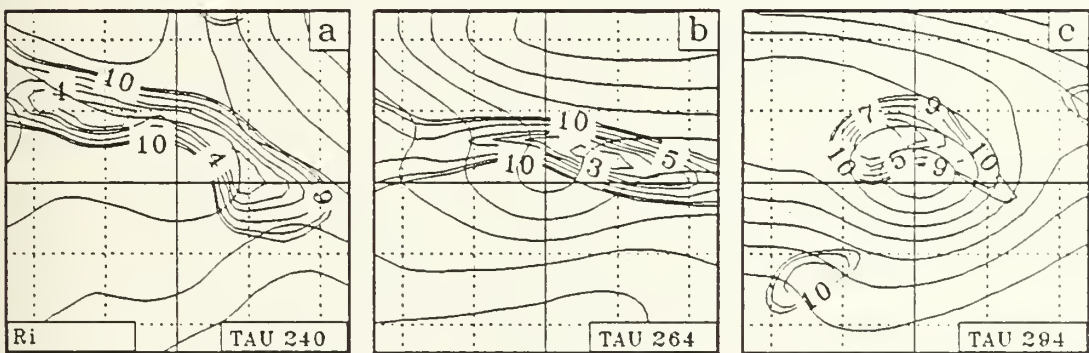
Fig. 3.17. 700 mb height (contours every 60 dam, solid) and Richardson number for NOGAPS Type I. Values above 10 are not contoured.

The rotation of the thickness change dipoles is important for later secondary cyclogenesis. Following development of the cyclone, cooling occurs in the southwest

quadrant (Fig. 3.16 1). This cooling, which is largely a
result of thermal advection (Fig. 3.16 c), is consistent
with the cyclonic vorticity generation at 500 mb (Fig. 3.11
i) occurring in that region. Furthermore, the patterns of
cooling at the location "w" in Fig. 3.16 1 are frontogen-
etic, which results in an area of enhanced baroclinity near
"w" in Fig. 3.3 c. Thus, the secondary vorticity maximum at
"w" in Fig. 3.1 c appears to be the result of baroclinic
processes, as suggested by the Ri minimum near that location
(Fig. 3.17 c).

3. Influence of Latent Heat Release

Condensation in the ascending air ahead of the
developing cyclone results in release of latent heat. In the
thickness tendency analysis presented earlier, diabatic
heating was shown to promote continued self-development of
the polar low by opposing the limiting effect of adiabatic
cooling (Fig. 3.16). This means that vertical ascent can
increase further than would occur if diabatic heating were
absent. This augmented vertical velocity leads to increased
generation of low-level vorticity and results in a more
vigorous cyclone. The enhancement of ascent by latent
heating has been noted by many investigators (e.g.
Smagorinsky, 1956; Aubert, 1957; Danard, 1964). Danard
(1964) solved the diagnostic quasi-geostrophic omega equa-
tion with and without latent heat release for a major winter
cyclone over the central United States. He found an approxi-
mate doubling of the vertical ascent when latent heating was
included, which led to strengthening of the low-level
convergence and high-level divergence. This resulted in an
increased production of low-level vorticity. Associated
changes in the ageostrophic (divergent) wind components
contributed to kinetic energy (KE) generation at both high
and low levels.

Another role for the internal diabatic heat source is generation of available potential energy (APE), which may be converted to storm KE. The concept of APE was introduced by Lorenz (1955), who defined it as the difference between the total potential energy of the atmosphere at a given time, and a hypothetical state obtained by adiabatically rearranging the thermal structure to a statically stable barotropic state. As such, it represents the part of the potential energy which is available for conversion to KE. The existence of APE generation is not a guarantee of an increase of storm KE; rather, it indicates an energy source potentially available for conversion to KE. Conversion is indicated by a positive covariance between specific volume and vertical motion (warm air rising, cold air sinking). As a first approximation, generation of eddy APE depends on covariances of heating and temperature deviations on an isobaric surface. Hahn and Horn (1969), and Bullock and Johnson (1971) used the exact expression for APE to show that a combination of heating at low-mid tropospheric levels in the warm sector, and cooling at mid-high levels in the cold sector is most conducive to eddy APE generation.

Production of APE for the model-generated polar low is evident in the previous analyses. The largest diabatic heating (Fig. 3.16 g-i) occurs above the location of maximum positive low-level temperature perturbation (Fig. 3.3 a-c). The thermal patterns at 700 and 850 mb (not shown) are approximately in phase with those at the surface. As self-development progresses, the net effect (Fig. 3.16 k-l) of diabatic heating, adiabatic cooling and thermal advection is to amplify the thermal wave. Moreover, the diabatic heating is increasing with time. The correlation of the diabatic heating with the growing temperature wave ensures increasing generation of APE as the low intensifies.

Covariances of omega and specific volume evaluated at 100 mb intervals have been used to diagnose baroclinic conversion (Fig. 3.18 b). Initially, weak eddy APE to KE transformations occur in a shallow layer below 750 mb, with another layer of weak positive conversion aloft. During the first 12 h, the shallow surface layer of positive conversion extends to 500 mb and strengthens. A thermally indirect circulation (negative conversion) develops above this level. Later, positive conversion occurs throughout the troposphere. The time section of diabatic heating (Fig. 3.18 a) is rather similar to that of vertical velocity (Fig. 3.7 b). This suggests that vertical ascent is enhanced by latent heat release. The similarity between the ascent and the diabatic heating patterns suggests that the temporal variation of the APE generation may resemble Fig. 3.18 b.

This analysis has shown that diabatic heating due to condensation in the warm sector enhances both generation of eddy APE and conversion to KE in the polar low. This is in accord with previous work for mid-latitude cyclones (e.g. Danard, 1966; Bullock and Johnson, 1971; Gall, 1976b; Vincent et al., 1977; Robertson and Smith, 1983). Furthermore, it is apparent that net warming patterns favorable for self-development (warming in warm sector, cooling in cold) imply increasing APE generation and conversion to storm KE. Hodur (1984) compared adiabatic and diabatic simulations of a wavenumber 20 (wavelength about 1400 km) baroclinic disturbance. The disturbance grew from a zonal initial state typical of conditions during the genesis of Pacific polar lows (Mullen, 1979). Hodur found that inclusion of diabatic effects increased the KE of the disturbance by an order of magnitude, as rapid intensification resulted from a much strengthened baroclinic conversion of eddy APE to KE. The depth of the layer of positive eddy conversion was much greater for the moist experiment which resulted in a deeper disturbance.

DIABATIC HEATING (°C per day)
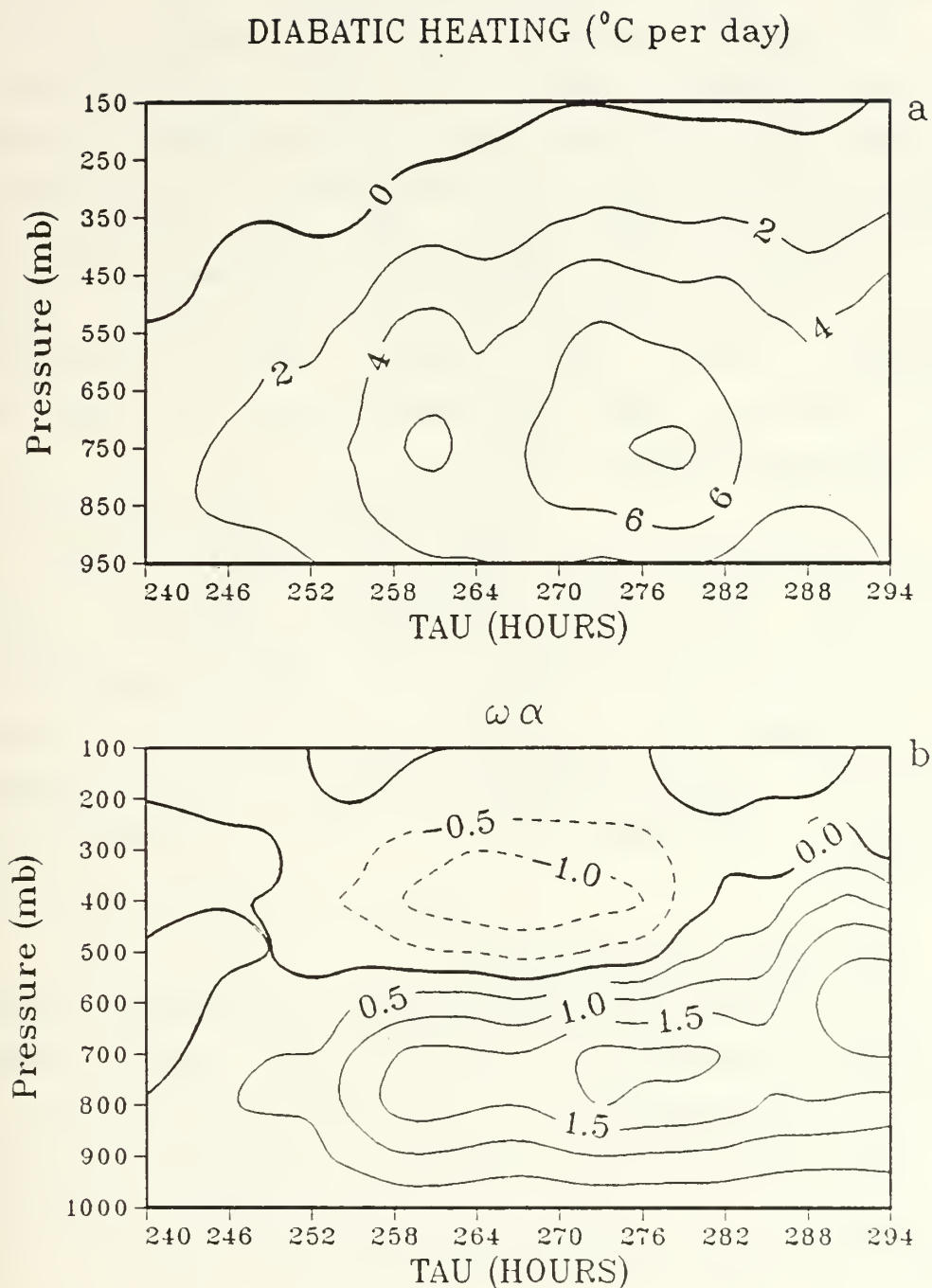
Fig. 3.18.   (a) Time evolution of diabatic heating (°C per day) and (b) baroclinic conversion (mW kg^{-1}) for NOGAPS Type I. Format as in Fig. 3.7.

73

The Pacific type polar low is generally a deep disturbance having significant geopotential amplitude near the tropopause (Reed, 1979; Mullen, 1979; Locatelli et al., 1982). At genesis, the Type I polar low is shallow, as it forms under straight upper-level flow. The release of latent heat plays a crucial role in the formation of upper-level geopotential waves by contributing to the increase in the temperature perturbation in the warm sector at mid-levels. The maximum eddy conversion is shifted upward which results in a deeper disturbance than would be the case in the absence of latent heating (Gall, 1976b). Alternately, diabatic heating allows self-amplification of the upper waves to progress further.

Tracton (1973) suggested that the latent heat release associated with precipitation creates the imbalance necessary for the onset of development prior to the time when vorticity advection alone would initiate development. This is certainly the case here, since the initial PVA is minimal. In this case, the development of upper-level PVA can be viewed as the hydrostatic response of the system to thermodynamic forcing and is not a precursor of cyclogenesis.

4. Moisture Budget Analysis

In the previous subsection, it was shown that the thermodynamic balance of the developing system depends crucially on the strength of the latent heat release. To examine the processes which ensure the supply of water vapor to the ascending air, a quasi-Lagrangian moisture budget has been performed (Fig. 3.19) for the NOGAPS-simulated polar low. The moisture conservation equation

$$E-P = \frac{\partial q}{\partial t} + \nabla \cdot [q(\mathbf{V} - \mathbf{C})] + \frac{\partial}{\partial p}(q\omega) \qquad (3.6)$$

74

expresses the difference between evaporation (E) and precipitation (P) as the sum of horizontal and vertical flux divergences of specific humidity (q) and the quasi-Lagrangian tendency term (change in storage). E-P is computed as a budget residual. Large accumulations of water vapor result from horizontal and vertical flux convergence (Fig. 3.19 d-f). Because there is little change in the mean vapor content of the column, there must be a net loss of water from the system (precipitation), as indicated by the negative residual for the volume. It should be remembered that evaporation of the condensed water is also occurring at some gridpoints within the volume. The negative residual indicates that precipitation exceeds evaporation when averaged over the budget volume.

Most of the water vapor accumulation occurs as a result of the mean circulation. Horizontal moisture flux convergence is strong near the surface and decreases to near zero above 700 mb (Fig. 3.19 d-f). Near the surface, this is offset by vertical flux divergence. In the mid and upper troposphere, most of the moisture accumulation for precipitation arises from vertical flux convergence.

5. Role of Air-Sea Fluxes

The boundary fluxes of moisture and heat arise from air-sea moisture and temperature differences in the presence of boundary layer winds. In the NOGAPS simulations, the model sea-surface temperature (SST) is independent of longitude with the maximum SST gradients between 45 and 50° N and between 32 and 42° S.

In NOGAPS, the PBL fluxes are assumed to heat the lowest sigma layer of the model, which is about 200 mb deep. A surface heat flux of 100 W m^{-2} is equivalent to a heating rate of about 4°K per day for a 200 mb deep layer. The air-sea sensible heat flux is shown in Fig. 3.20. At early
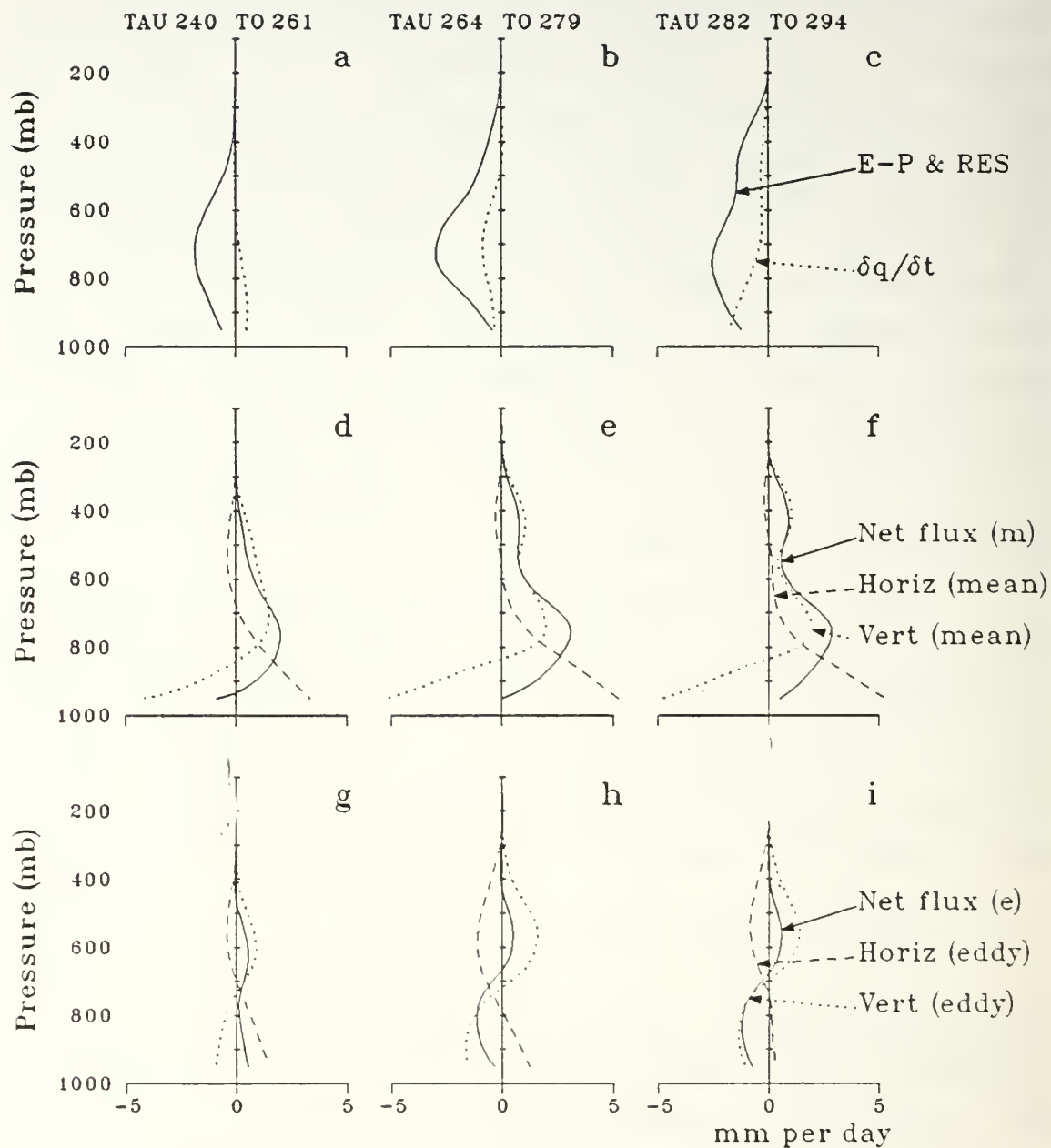
Fig. 3.19.   Moisture budget terms for NOGAPS Type I. Format
              as in Fig. 3.10.

stages of development when the surface winds are light, the
fluxes are negligible (Fig. 3.20 a). As the disturbance
becomes more intense, the fluxes (Fig. 3.20 b) tend to warm
the coldest air and cool the warmest air (compare Fig. 3.3
b). These sensible heating patterns oppose the effects of
thermal advection and inhibit growth of the thermal wave.
This tends to destroy eddy APE and oppose self-development.
However, even the strongest flux in Fig. 3.20 amounts to
only a few degrees per day of heating. A surface flux of 100
W m^{-2} causes a thickness increase of only 25 gpm per day in
a 200 mb surface layer, which is only a small fraction of
the diagnosed thickness tendency components in Fig. 3.16.
Thus, in this case, the surface heat flux offers minimal
opposition to cyclogenesis.
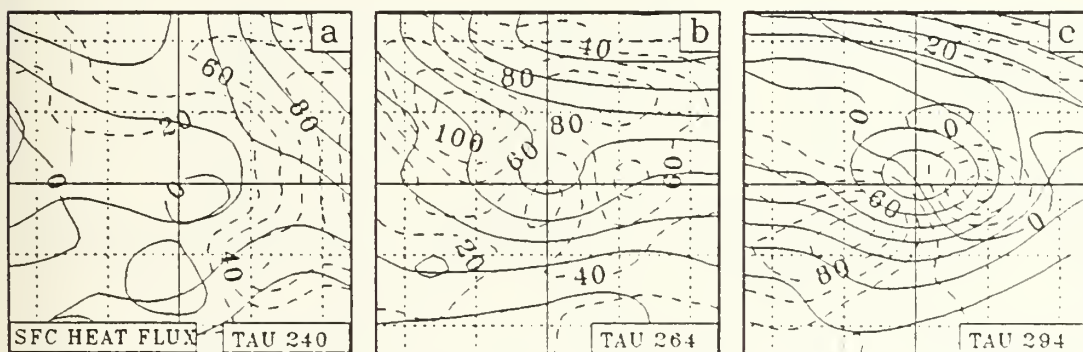
Fig. 3.20. (a-c) As in Fig. 3.1 a-c except surface sensible
heat flux (Wm^{-2}, dashed)

6. FGGE Case

The budgets of heat and moisture, and the thickness tendency analysis have been also performed for the FGGE polar low. The heat budget results are presented in Fig. 3.21. The diabatic heating is inferred as the budget residual, which also includes computational uncertainty. At the initial time, there is a deep layer of cooling above a shallow surface layer of heating (Fig. 3.21 a). It is unlikely that a deep layer of diabatic cooling of such intensity would result from radiation or evaporation. Similarly, the layer of diabatic heating of 10° per day in the stratosphere at this time is also unrealistic. Thus, the diagnosis of heat budget terms using FGGE data is subject to much uncertainty. It is possible that strong radiational cooling which exists near the ice-covered, elevated terrain of Greenland during the long polar night may contribute to the negative residual at mid-levels. However, the shallow layer of surface heating in Fig. 3.21 a appears to contradict this explanation. This layer of heating is probably due to increasing surface fluxes as the disturbance moves from ice-covered terrain over warmer water and intensifies.

The inability to close the FGGE heat budget to an acceptably small residual appears to be a result of data uncertainty. Additional error may be introduced by the use of the archived temperature data which are from the ECMWF forecast model first guess (Paegle, 1983). These temperatures are not in hydrostatic balance with the analysed height fields. Wash and Calland (1985) compared these temperatures with those computed hydrostatically from the height fields. They found RMS differences in the troposphere of less than 2°C between the two estimates, while in the stratosphere, these differences were nearly 4°C. The larger departure in the stratosphere possibly accounts for the
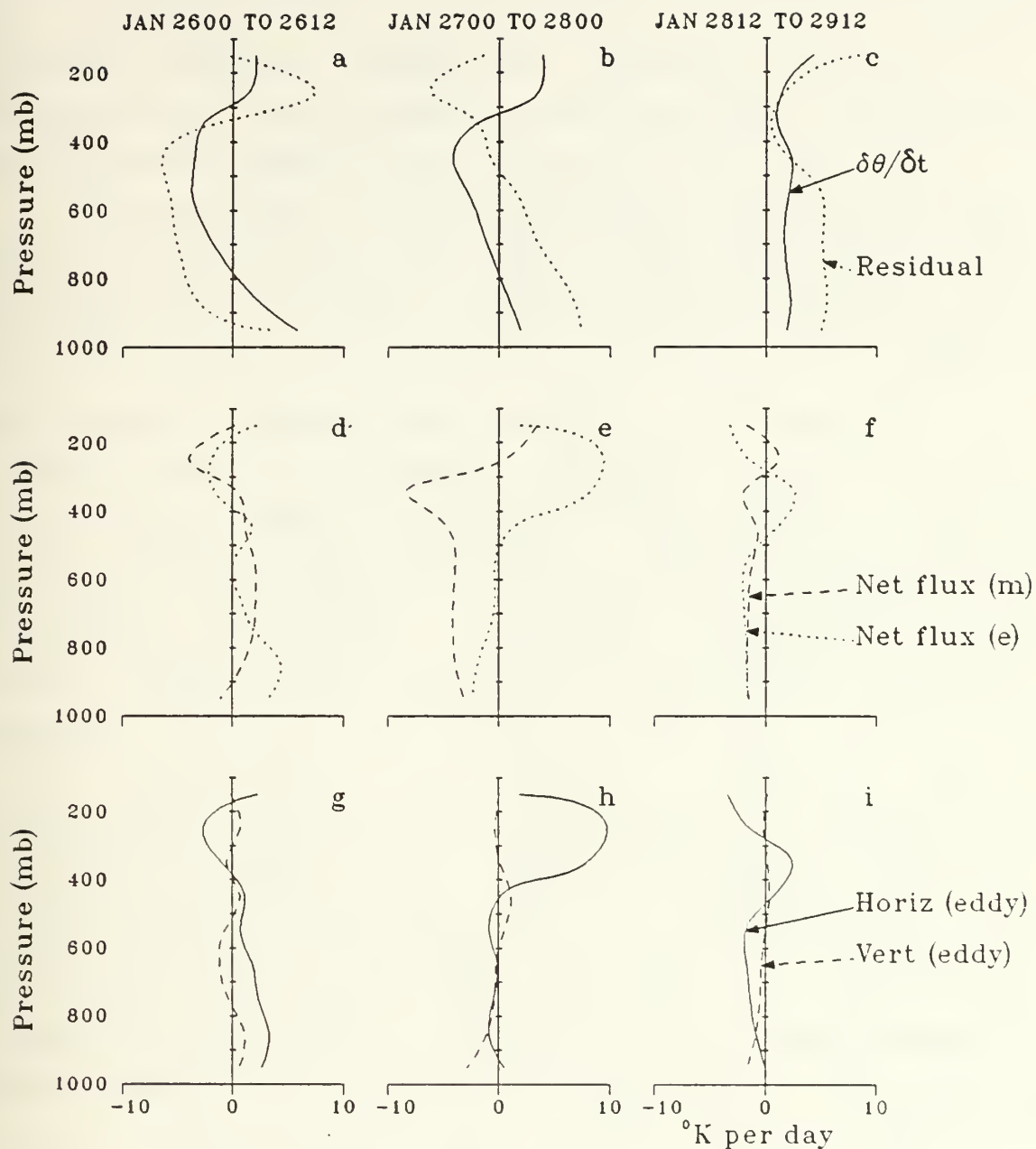
Fig. 3.21. As in Fig. 3.15 except for FGGE Type I.

large variability above 300 mb in the residual term in Figs. 3.21 a-c.

At later stages of development, diabatic heating (inferred from the heat budget residual) occurs throughout a deep layer (Fig. 3.21 b) and is countered by adiabatic cooling from the net mean fluxes (Fig. 3.21 e). This is similar to the heat budget result for the NOGAPS case (Fig. 3.15). In the FGGE case, the strength of the diabatic heating near the surface indicates large surface sensible heat flux.

The profiles of temperature tendency during the first 48 h (Fig. 3.21 a,b) are consistent with the rapid decrease in static stability during cyclogenesis which was discussed by Cook (1983). Following Sandgathe (1981), Cook used a stability index obtained by subtracting the 1000 mb potential temperature from that at 500 mb and dividing by the pressure difference. For the 4° radius budget volume used by Cook, this index decreased from 4.8°K per 100 mb at 1200 GMT 26 January to a minimum of 2.1°K per 100 mb at 0000 GMT 29 January. This minimum approaches the moist adiabatic value based on the area-averaged surface temperature at this time. For the NOGAPS case, the stability index is approximately 4.7°K per 100 mb. This is close to the moist adiabatic value of 4.8°K per 100 mb derived from the area-averaged surface temperature of 15°C. This is consistent with the near-cancellation of the diabatic heating and the adiabatic cooling in Fig. 3.16.

The time section of diabatic heating (Fig. 3.22 a) shows a deepening layer of heating with larger values nearer the surface. Strong surface heating is due to heat fluxes from the sea. At the initial time, the surface circulation is weak, and the fluxes are small, in spite of large initial air-sea temperature differences (Cook, 1983). However, as the cyclone develops, these fluxes rapidly become large and

result in an excess of 8° per day of surface heating at 1200 GMT 28 January. The later decrease of surface sensible heating is due to movement of the storm over Northern Ireland, with a large fraction of the budget volume over land. The SST gradient also is weaker south of 60° N.

Another factor which may account for the low elevation of the strongest heating is the initial vertical distribution of moisture. Because the air originated over ice-covered terrain, it would be expected to be rather dry prior to polar low formation. Large surface fluxes of heat and moisture quickly develop as this cold, dry air streams southward over the open water. Therefore, most of the moisture at early stages of development is confined to a shallow layer near the surface. Because of this moisture distribution, most of the latent heat release associated with ascent occurs at low elevations. This deepening layer of low-level heating contributes to the rapid destabilization described earlier.

The baroclinic conversion term (Fig. 3.22 b) is mostly positive above 800 mb, which supports the hypothesis that this cyclone grows through baroclinic processes. However, this term is smaller than for the NOGAPS case, and there is a layer of negative conversion near the surface. This reduced conversion is probably due to the much larger surface heat flux in the FGGE case, since strong heating in the cold sector tends to reverse the phase of the temperature wave near the surface. Thus, it appears that the surface sensible heat flux directly opposes baroclinic development.

The FGGE budget of vater vapor is presented in Fig. 3.23. At early stages of development, a deep layer of significant evaporation is implied by the positive budget residual. Such evaporation is unlikely except near the surface where cold, dry air moves over progressively warmer

HEAT BUDGET RESIDUAL (°C per day)
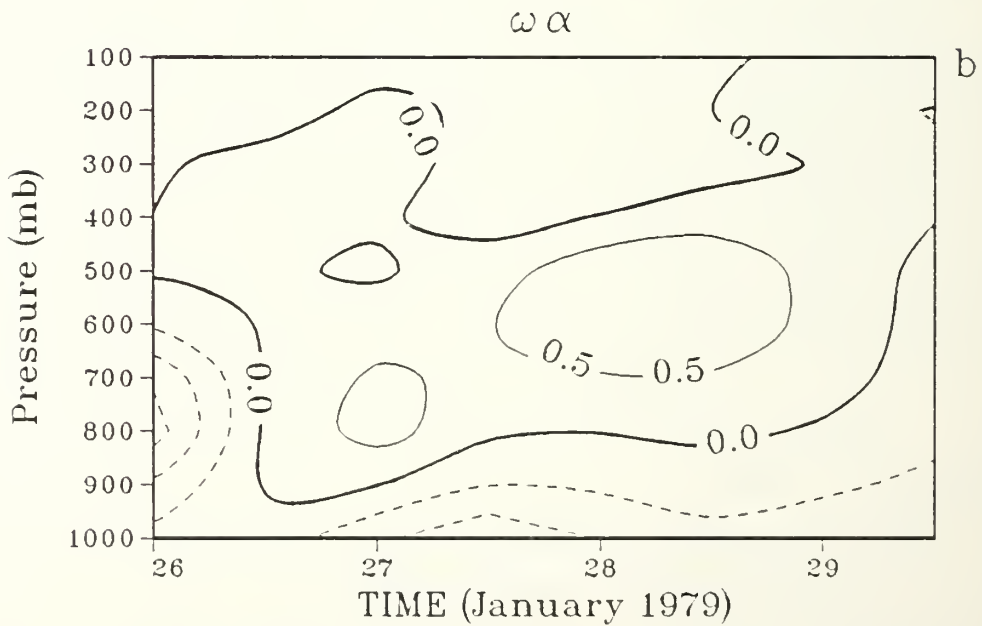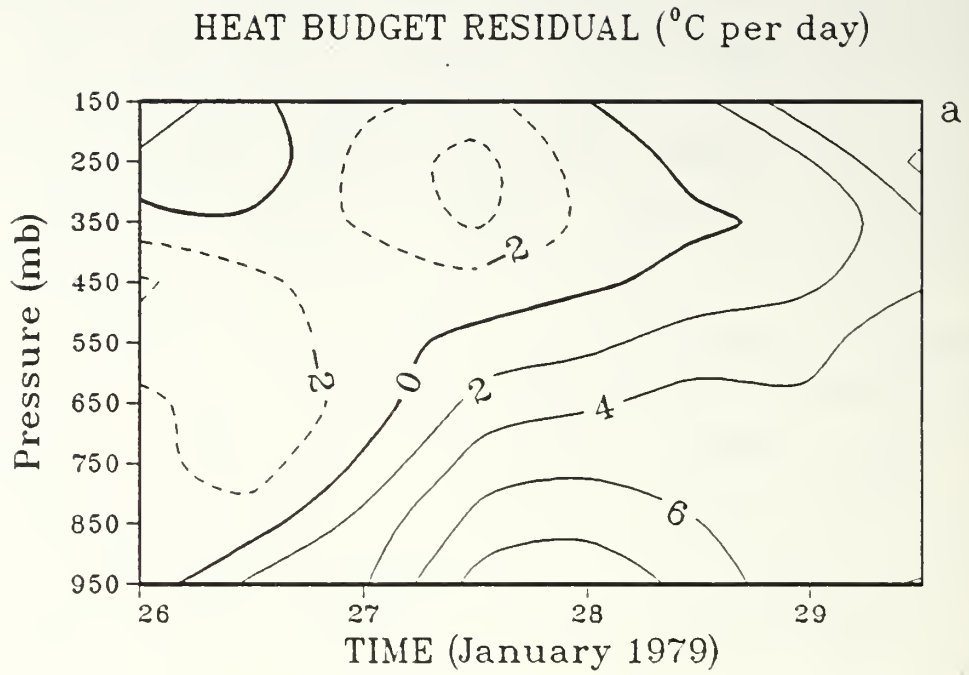
Fig. 3.22. (a) Heat budget residual for FGGE Type I.
(b) As in Fig. 3.18 b except for FGGE Type I.

82

water.   Problems with the FGGE humidity analysis contribute
to these   large residuals.   In the   ECMWF analysis   scheme,
humidity observations received a very large weight compared
with the model   first guess during the period of this storm
(Paegle,   1983).   These humidity observations were comprised
of   radiosonde data   and surface   observations of   sometimes
questionable quality, which led to very noisy analyses.

        At later times,   a net moisture sink due to precipi-
tation occurs above a shallow moisture source due to evapo-
ration from the sea (Fig.   3.23 b,c).   This precipitation is
associated with the diabatic heating in Fig. 3.22 a.   As for
the NOGAPS case,   most of the water vapor accumulation comes
from horizontal flux convergence near the surface,   and from
vertical flux convergence above about 900 mb (Fig.   3.23
e,f). Eddy terms (Fig.   3.23 h,i) are small.   Precipitation
amounts are about 30% of those for the NOGAPS case, even
though the mass circulations are of similar strength for the
two cases.   This is a result of the much lower temperatures
associated with the FGGE case.   It is also possible that the
NOGAPS model parameterization results in an overestimation
of precipitation.

        The thickness tendency analysis for this   storm is
presented in Fig.   3.24. The terms are calculated from (3.4)
as before,   except that the tendency term is computed
directly from the gridpoint tendencies, and the diabatic
term is inferred as a residual.   At the initial time, advec-
tive warming occurs to the south of the incipient low, with
cooling to the northwest (Fig.   3.24 a).   The net thickness
tendency (Fig.   3.24 j) shows cooling to the north of the
disturbance which is consistent with the southward movement
of the jet streak and associated baroclinic zone (Figs.   3.5
a,b and 3.6 a,b).   There is little indication of self-
development at this time. Adiabatic cooling (Fig. 3.24 d)
and diabatic heating (Fig. 3.24 g) occur to the north of the
low center.
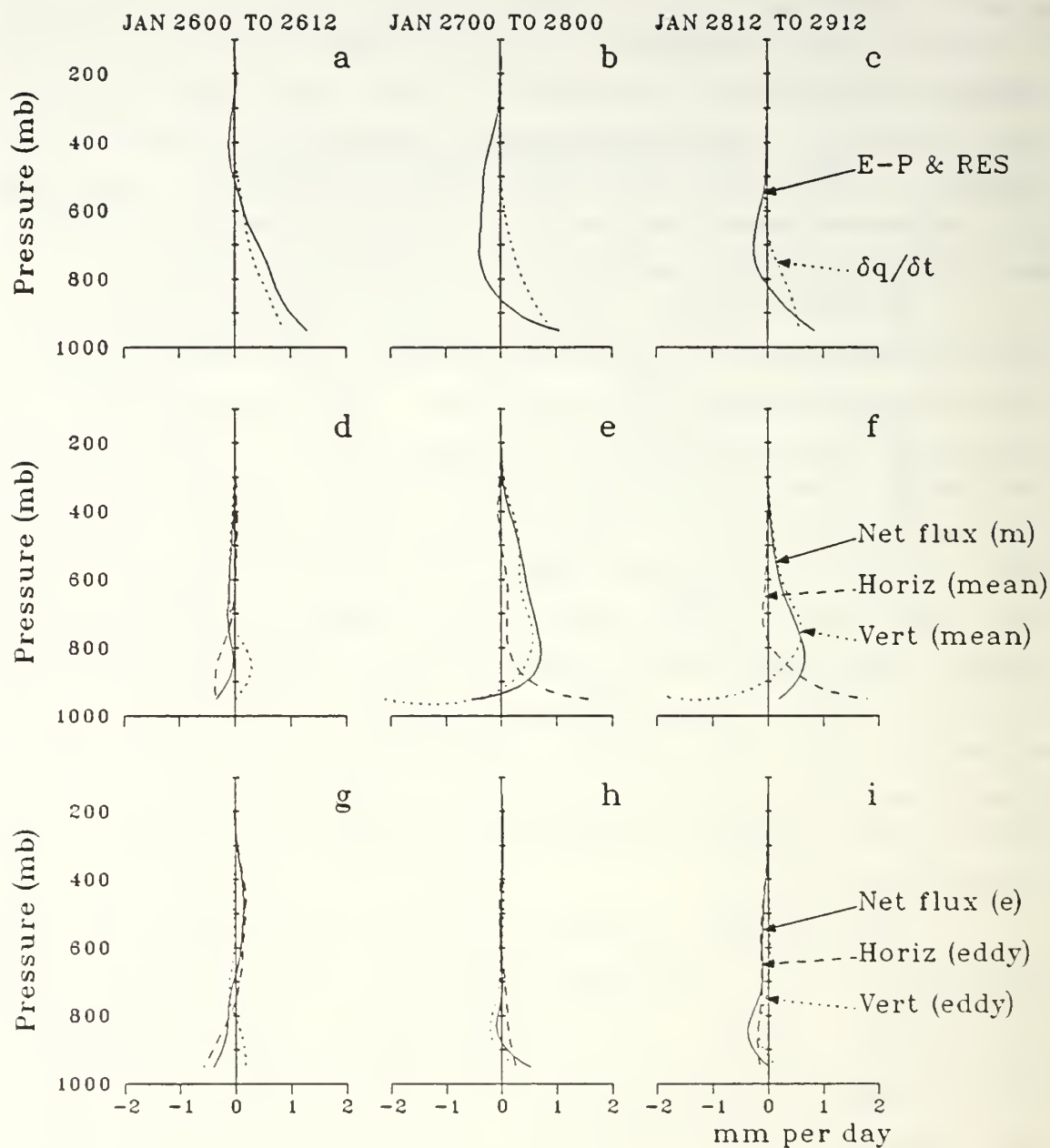
Fig. 3.23. As in Fig. 3.19 except for FGGE Type I.

84
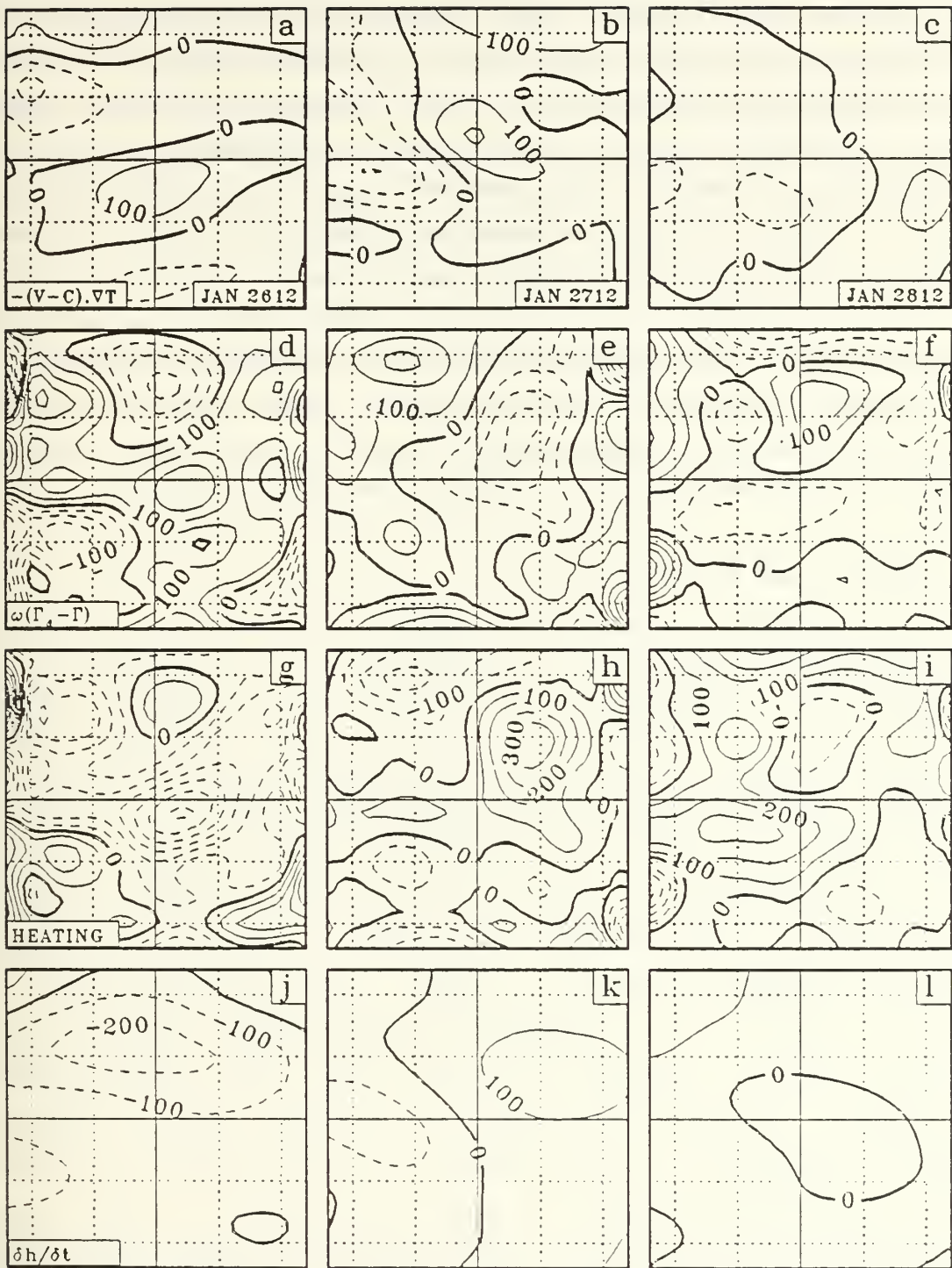
Fig. 3.24. As in Fig. 3.16 except for FGGE Type I.

At the time of most rapid development (1200 GMT 27 January, see Fig. 3.12), a net dipolar pattern of warming to the east and cooling to the west is evident (Fig. 3.24 k). This dipole is modulated by the thermal advection field (Fig. 3.24 b), and is indicative of self-development, as discussed earlier for the NOGAPS case. Diabatic heating (Fig. 3.24 h) offset by adiabatic cooling (Fig. 3.24 e) occurs to the northeast of the low center.

At maturity, cooling occurs throughout a broad area above the low center (Fig. 3.24 l). This tends to produce a more vertical structure to the system. The thermal advection dipole has weakened considerably due to the much reduced baroclinity of the system at this time (Fig. 3.5 c).

E. SUMMARY AND DISCUSSION

The development of the Type I polar low has been described using thermodynamic and vorticity balance considerations. The disturbance is triggered by low-level baroclinic processes. At genesis, weak warm advection associated with the initial baroclinic surface disturbance results in ascent ahead of the low. Associated latent heat release further contributes to ascent. Surface convergence leads to development of the surface low, which further strengthens low-level thermal advection. Thus, initial development of the polar low is a cooperative interaction between the growing vertical mass circulation and the thermodynamic processes. Since surface winds are light at early stages of polar low formation, the tendency of the surface fluxes to oppose development is small.

As development occurs, thermal advection, adiabatic cooling and latent heating combine to produce hydrostatic temperature changes which favor the formation of an amplifying upper-level geopotential wave. This wave is coupled

with the developing low-level cyclone. Thus, the sequence of self-development, which has been previously applied to larger scale mid-latitude extratropical cyclones, appears to apply on the smaller polar low scale. As self-development proceeds, vorticity advection becomes the leading term in the vorticity balance. The required increase in vorticity generation is accomplished by expansion of the upper trough, and the movement of the polar low to the cyclonic side of the jet.

During the final stages of development, the nonlinear effects of vorticity and thermal advection appear to generate conditions favorable for later secondary developments. Thermal advection results in progressive amplification of the thermal waves which contributes to frontogenesis in an area to the southwest of the low center and an area to the east. These areas are the expected locations of cold and warm fronts. Furthermore, hydrostatic geopotential changes which occur primarily as a result of advective thermal changes result in cyclogenesis aloft near these two regions. The PVA ahead of these two lobes of cyclonic vorticity is associated with upper-level divergence and vertical ascent, which will contribute to the future development of baroclinic disturbances near these locations.

Since the Type I low forms on the anticyclonic side of the jet, the upper-level divergent flow is initially inefficient in producing vorticity changes aloft. Thus, initial growth of the mass circulation is accompanied by only modest changes in the upper-level vorticity structure. This is similar to a cyclone described by Pagnotti and Bosart (1984) which formed beneath anticyclonic upper-level flow on the equatorward side of the jet streak, and was accompanied by significant precipitation. They found that the vertical ascent was forced predominantly by latent heating and thermal advection, with very little initial development of upper-level PVA.

Because the Type I polar low forms in the absence of PVA aloft, it is initially detected as a surface disturbance. In the NOGAPS case, a pre-existing low-level vorticity maximum provides the initial disturbance. In the FGGE case, the origin of the initial perturbation is unclear. Orographic (lee-side) effects associated with Greenland may be important. Strong surface heating as cold air moves off ice-covered terrain would also lead to falling surface geopotentials. However, understanding the deformation fields within the parent cyclone appears to be the key to successful prediction of Type I polar low cyclogenesis.

General synoptic features of the simulated polar low are consistent with the FGGE analyses (and earlier observational studies of maritime cyclogenesis). This demonstrates the realism of the model simulations and justifies the detailed analysis of model output. Because the model-generated data set is complete to computer accuracy, vorticity, heat and moisture budget terms can be diagnosed with confidence. In comparison, the FGGE analyses are rather noisy, as evidenced by the inability to satisfy the fundamental conservation equations. One source of uncertainty is that the archived temperature data are from the ECMWF forecast model, which was used for the first guess. The humidity observations, which were of poor quality, were given too much weight in the ECMWF analysis scheme during the period of the FGGE storm. In addition, the FGGE analyses appear to be especially deficient near steep topography such as Greenland.

In summary, it is evident that the Type I polar low grows through baroclinic processes. Locally reduced Richardson number in the vicinity of the disturbance, positive correlation between vertical motion and temperature, and the decreasing baroclinity which accompanies cyclogenesis appear to support this conclusion. In the cases presented here, the initial formation of the surface

88

disturbance is favored by reduced static stability and enhanced baroclinity, and occurs without the presence of significant upper-level PVA. The formation of the Type I polar low on the equatorward side of the upper-level jet appears to contradict the conclusion of Reed (1979) and Mullen (1979) that polar lows form on the cyclonic shear side of the jet. The complete record from the model simulation has permitted a detailed description of the Type I polar low, which does not initially have significant PVA aloft. A similar description of a Type II polar low which is triggered by PVA aloft will be given in the next section.

IV. CYCLOGENESIS UNDER DISTURBED UPPER FLOW

As described in the previous chapter, the Type I polar low forms under undisturbed upper-level flow on the equatorward side of the upper jet. Development is initiated by low-level baroclinic processes which couple to developing upper waves. Storm intensification results from a cooperative interaction between the increasing surface circulation and the amplifying upper-level features.

Type II polar lows typically form on the cyclonic side of the upper-level jet in a strong polar air stream, and are distinguished from Type I disturbances by the initial presence of appreciable upper-level PVA. The polar lows described by Mullen (1979, 1983) and Reed (1979) fulfill these criteria. These North Pacific disturbances form in the polar airstreams behind or poleward of major frontal bands. They are associated with strong baroclinity throughout the troposphere, and originate as areas of locally enhanced convection. A substantial depth of the troposphere is conditionally unstable and strongly heated from below, especially at early stages of development. As these storms develop, they acquire a comma-shaped cloud pattern, and are accompanied by a westward-tilting geopotential perturbation throughout the entire depth of the troposphere.

As with Type I disturbances, the Type II polar lows may attain considerable intensity and replace the primary low as the main circulation center. Occasionally, a wave develops on the polar front just ahead of the comma cloud (polar low). If the distance between the comma cloud and the frontal cloud band becomes small enough, the two features combine to form a cloud image which resembles a mature occluded cyclone. This is the so-called instant occlusion

process that was first described by Anderson et al., (1969). Sometimes, the polar low develops occlusion-like features separate from the main front (Locatelli et al., 1982). Mullen (1983) described examples of rapidly deepening cyclones in polar air streams which formed downstream of a mobile upper-level trough within or poleward of the upper-level jet. These North Pacific cyclones satisfied Sanders and Gyakum's (1980) criterion for "explosive deepening" (average central pressure falls in excess of 1 mb/h for 24 h).

Two examples of Type II developments will be presented in this chapter -one from the NOGAPS simulations by Sandgathe (1981) and the other from the FGGE data. Because a detailed description of the quasi-Lagrangian analyses was presented in the previous chapter, comparatively brief results will be presented for these cases.

A. SYNOPTIC OVERVIEW

1. NOGAPS Case

The model-generated surface polar low formed in a strong, initially undisturbed, cyclonically-curved northwesterly air stream behind a major cyclone (Fig. 4.1 a). This small disturbance grew as an intensifying trough within this flow and eventually became a closed circulation and replaced the parent low as the main low center (Fig. 4.1 b,c). The polar low formed beneath the PVA ahead of a developing 500 mb trough (Fig. 4.1 d-f). The upper trough attained considerable amplitude by the end of the period (Fig. 4.1 f) with little development of the downstream ridge. Except for the smaller horizontal scale of this system, this development appears very similar to the Petterssen (1956) description of cyclogenesis which occurs in reponse to PVA forcing aloft.
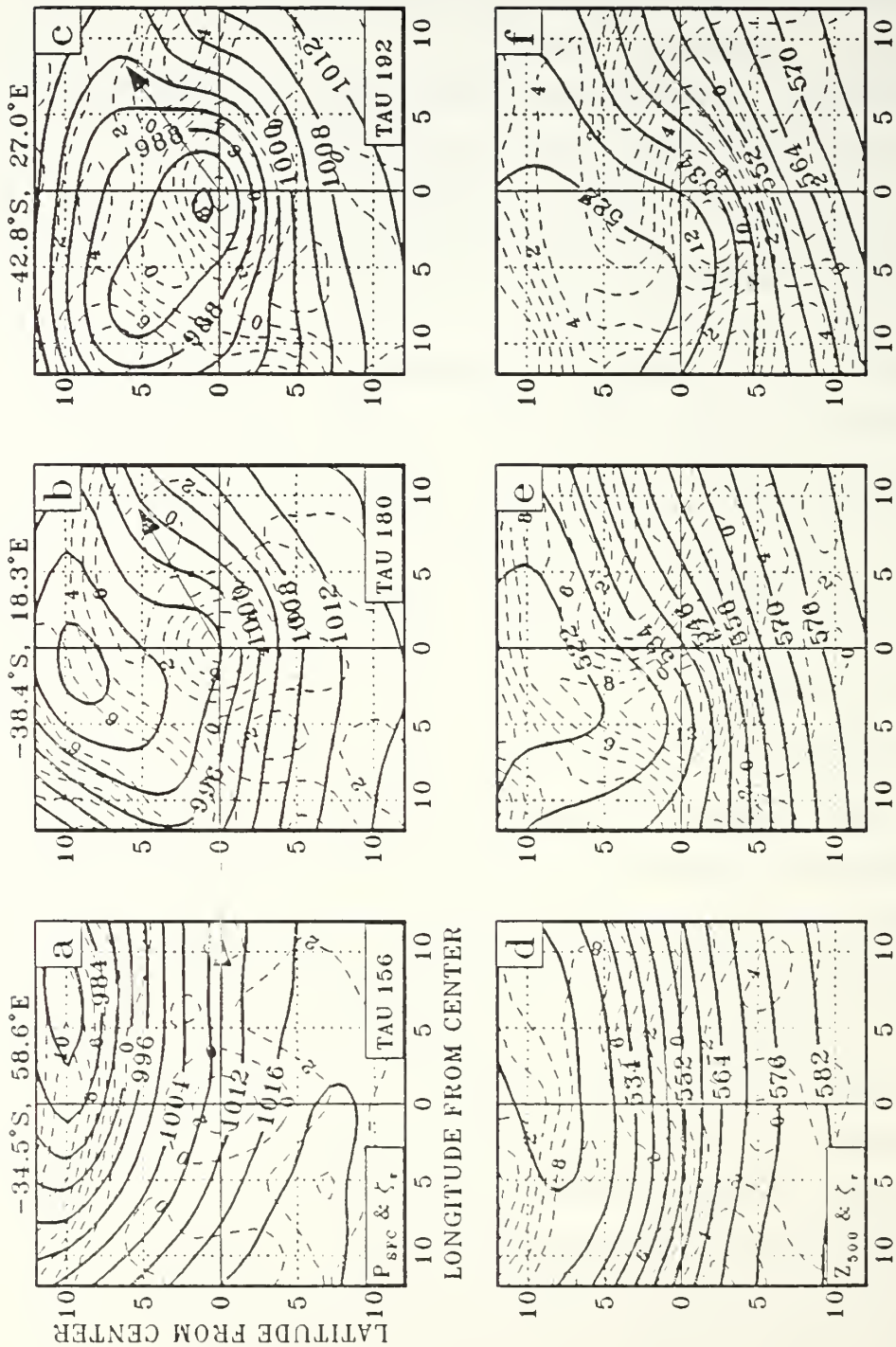
Fig. 4.1. (a-c) Surface pressure (mb, solid) and relative vorticity (10^{-5} s^{-1}, dashed); and (d-f) 500 mb heights (dam solid) and relative vorticity (10^{-5} s^{-1}, dashed) for NOGAPS Type II. The coordinates of the surface vorticity center are specified at the top of the figure and the translation velocity is indicated by the arrow such that 5° of latitude corresponds to 10 ms^{-1}. Time is indicated in the lower right corner.

This cyclone appears to be more vigorous than the NOGAPS Type I low. Whereas the Type I disturbance forms in an area of light surface wind, the Type II storm forms within a surface flow in excess of 15 m s^{-1}. At 300 mb, wind speeds in excess of 65 m s^{-1} occur above the low center (Fig. 4.2 a). The surface pressure at the disturbance center fell from 1010 mb to less than 981 mb over a 36 h period. During the final 12 h, an 11 mb fall occurred. This deepening rate is not far short of Sanders and Gyakum's (1980) criterion for explosive cyclogenesis.

Vertical motion fields (Fig. 4.2 d-f) for the model-generated polar low suggest development of the classical comma ascent signature. The similarity between these model-derived ascent fields and the usual satellite-observed extratropical cyclone cloud patterns is striking. Realistic features such as the appearance of a subsiding air slot and cyclonic rotation of the cloud system are reproduced. As for the Type I case, the strongest ascent occurs in the head of the comma, which is located within 100 km downstream of the surface vorticity maximum. For this disturbance, the minimum surface pressure tends to be located about 1-2 degrees of latitude poleward of the maximum surface vorticity (Fig. 4.1 b,c). Therefore, the minimum surface pressure occurs on the upstream poleward side of the comma head, as evident in Fig. 4.2 d-f. This conclusion also applies to the NOGAPS Type I polar low (see Fig. 3.2 d-f). The comma tail appears to lie within the surface trough, as also noted by Reed (1979).

The 300 mb isotach analysis (Fig. 4.2 a-c) shows that the cyclone forms in the exit region of a strong (65 m s^{-1}) advancing upper jet. As development of the surface low occurs, the jet becomes located about 500 km to the south of the surface cyclone (Fig. 4.2 c). The strongest vorticity in Fig. 4.1 d-f is found in the zone of enhanced
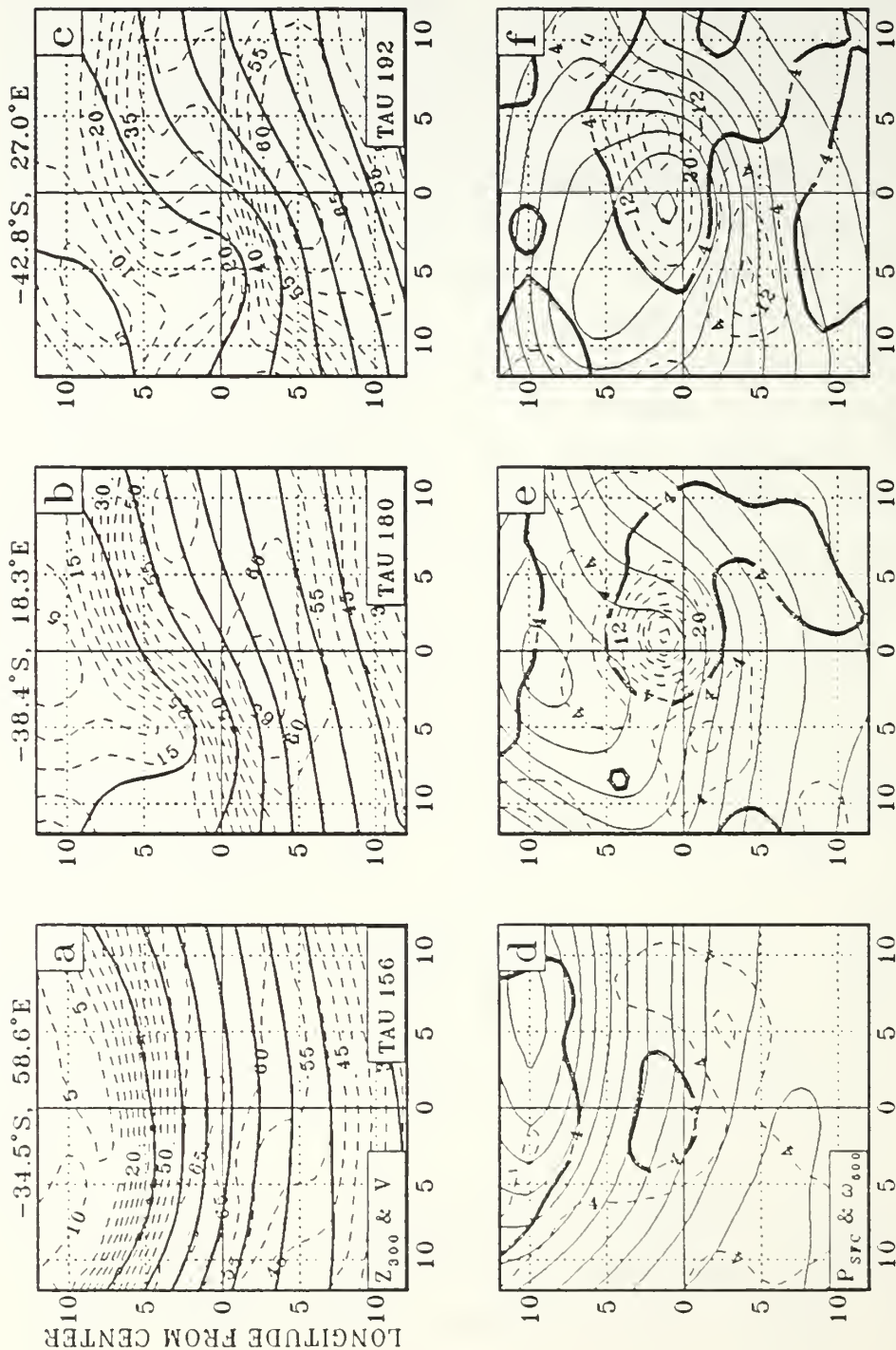
Fig. 4.2. (a-c) 300 mb heights (contours every 120 dam, solid) and wind speed (ms⁻¹, dashed); and (d-f) surface pressure (contours every 4 mb, solid) and 500 mb vertical p-velocity (mb h⁻¹, dashed, except that -4 mb h⁻¹ isoline highlighted for clarity) for NOGAPS Type II. Format as in Fig. 4.1.

94

shear vorticity immediately to the poleward side of the wind maximum (Fig. 4.2 a-c). In contrast to the Type I polar low, which spends a significant fraction of the early development stage on the equatorward side of the upper jet, the Type II disturbance forms and develops directly underneath the poleward side of the jet.

The strength and movement of the upper jet agree reasonably with Mullen (1979), who composited 22 cases of North Pacific polar lows. At genesis, the composite disturbance was located 500 km to the north of the jet stream, which had a mean speed of 65 m s^{-1}. At maturity, the mean center was located 750 km to the north of a weaker (55 m s^{-1}) jet streak. Mullen defined genesis as the stage prior to the appearance of a comma cloud configuration, when a solid area of enhanced convection was evident in the infrared (IR) satellite imagery. Maturity occurred when the cloud pattern was comma-shaped, but without excessive spiralling.

The main disparity between the NOGAPS Type II low and the observational cases of Mullen (1979) is the location of the upper-level jet at polar low genesis. In Mullen's composite, the jet lies 500 km to the south of the incipient disturbance. In the NOGAPS case, the low forms directly under the upper-level wind maximum. It is possible that genesis in Mullen's cases is detected much later than for the NOGAPS low, since considerable vertical ascent is already occurring at genesis in Mullen's cases. At later stages, the model jet coincides with the subsident slot, with the tail lying to the south of the jet. This agrees partly with Carr and Millard (1985), who composited the large scale environment for 68 comma-cloud systems over the Great Plains. They found evidence of two upper-tropospheric wind maxima -one aligned along the dry slot axis and the other cutting across the southern section of the comma tail.

Hodur (1984) initialized the Navy Operational Regional Atmospheric prediction System (NORAPS) with the composited data of Mullen (1979) that was typical of conditions during the genesis stage of North Pacific polar lows. With the full diabatic version of the model, he found that the simulated polar low developed about 750 km north of the jet, in agreement with Mullen's (1979) observations. When the adiabatic version of the model was used, the simulated polar low formed 1000 km north of the jet. This suggests that latent heating may account for development closer to the jet. In Mullen's data, the low formed with a mean surface temperature of 7°C while the NOGAPS Type II developed with a surface temperature of 14°C. Therefore, the effect of latent heating would be greater in the warmer NOGAPS storm, which may account for the development closer to the jet.

Thermal fields for the NOGAPS case (Fig. 4.3) show strong initial baroclinity, especially at 500 mb (Fig. 4.3 d). Development of the cyclone is accompanied by rapid amplification of the thermal wave, which results in a strong thermal ridge (trough) ahead of (behind) the surface low center. At later stages, the thermal patterns are quite similar to the classical frontal cyclone, with enhanced baroclinity to the southwest and to the east of the surface center (Fig. 4.3 b,c,e,f).

2. FGGE Case

The Type II FGGE case chosen for this study formed at 1200 GMT 27 December 1978 in the northwesterly air stream of a mature 972 mb cyclone which was located over the central North Pacific Ocean. Synoptic features of this polar low are similar to those for the NOGAPS case previously described. The surface disturbance developed as a trough in the polar air stream (Fig. 4.4 a) and migrated about the
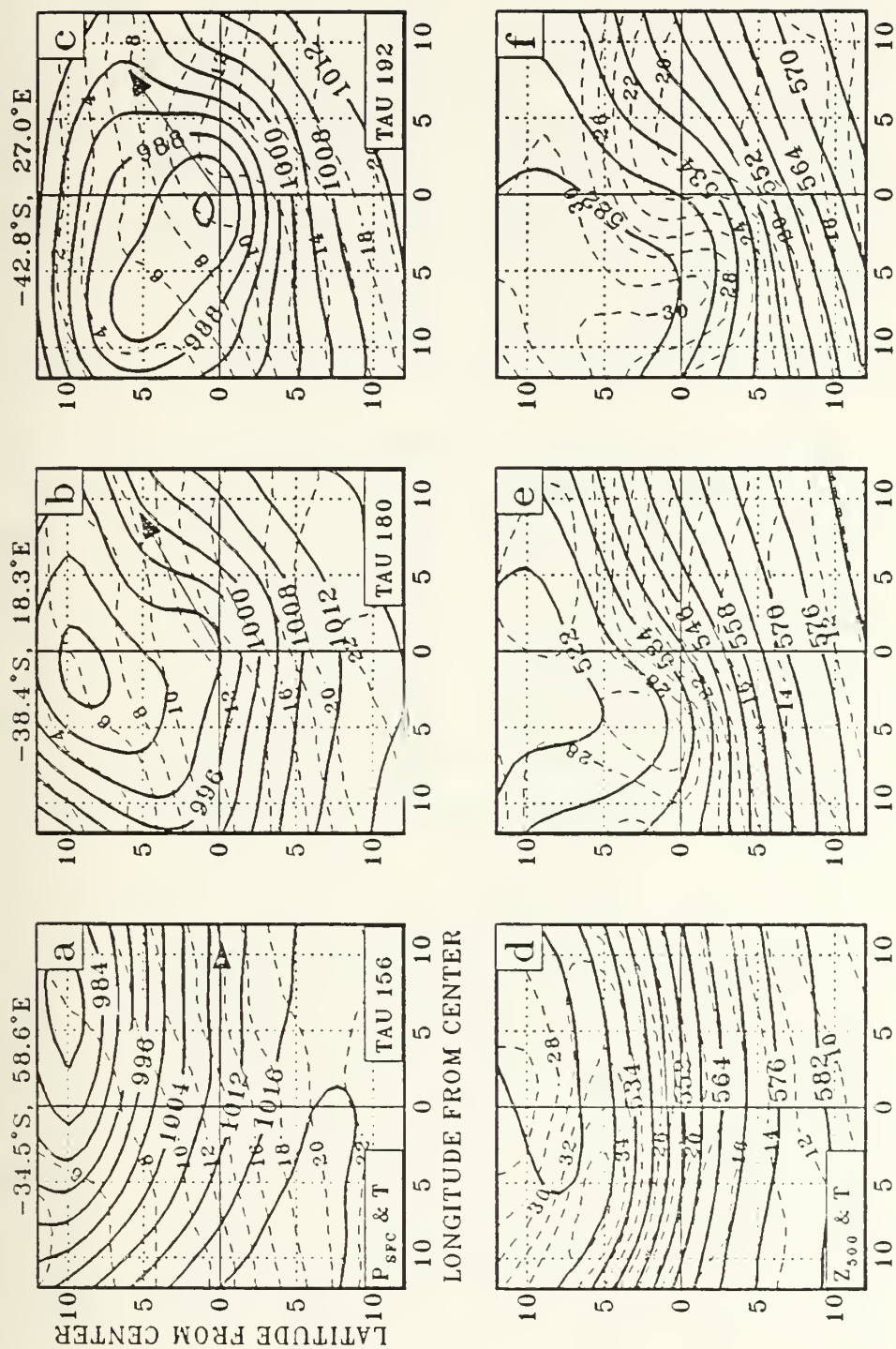
Fig. 4.3. (a-c) As in Fig. 4.1 a-c except surface temperature (°C, dashed); (d-f) as in Fig. 4.1 d-f except 500 mb temperature (°C, dashed).

parent low to eventually become a closed circulation (Fig. 4.4 b,c) in the southwestern Gulf of Alaska. Associated surface pressure falls were small, but the relative vorticity increased from around 4×10^{-5} s^{-1} to 8×10^{-5} s^{-1} at the low center. The surface trough in the earliest analysis (Fig. 4.4 a) is stronger than the corresponding initial NOGAPS disturbance (Fig. 4.1 a). In the NOGAPS case, the 3-hourly data permitted detection of the incipient polar low at a much earlier stage than for the 12-hourly FGGE data.

As in the NOGAPS case, the surface disturbance formed beneath the area of PVA ahead of a rapidly developing 500 mb trough (Fig. 4.4 d). At the end of the period, an almost-closed upper-level low was present directly above the surface low (Fig. 4.4 f). This vertically stacked orientation of the lower and upper features was not evident for the NOGAPS storm. In that case, the 500 mb low center was located 800 km to the northwest of the surface low at the final stages of development (Fig. 4.1 f).

Surface and 500 mb thermal fields (Fig. 4.5) showed that the polar low formed within a deep baroclinic zone. The convoluted patterns of surface temperature at later stages of development (Fig. 4.5 b,c) are probably due to data uncertainty. Since the model-generated surface temperature fields in Fig. 4.3 a-c are known to computer accuracy, they are smooth in comparison to the observed temperatures. At the initial stage, a cold pool with temperatures below $-32°C$ was evident at 500 mb. Based on Fig. 4.5 a,d, the static stability index at this time was $2.4°K$ per 100 mb. The moist adiabatic stability index corresponding to the surface temperature of $9°C$ was $3.5°K$ per 100 mb, which indicated that the incipient polar low environment was conditionally unstable. Later, the 500 mb cold center was located to the south of the surface low center (Fig. 4.5 f).
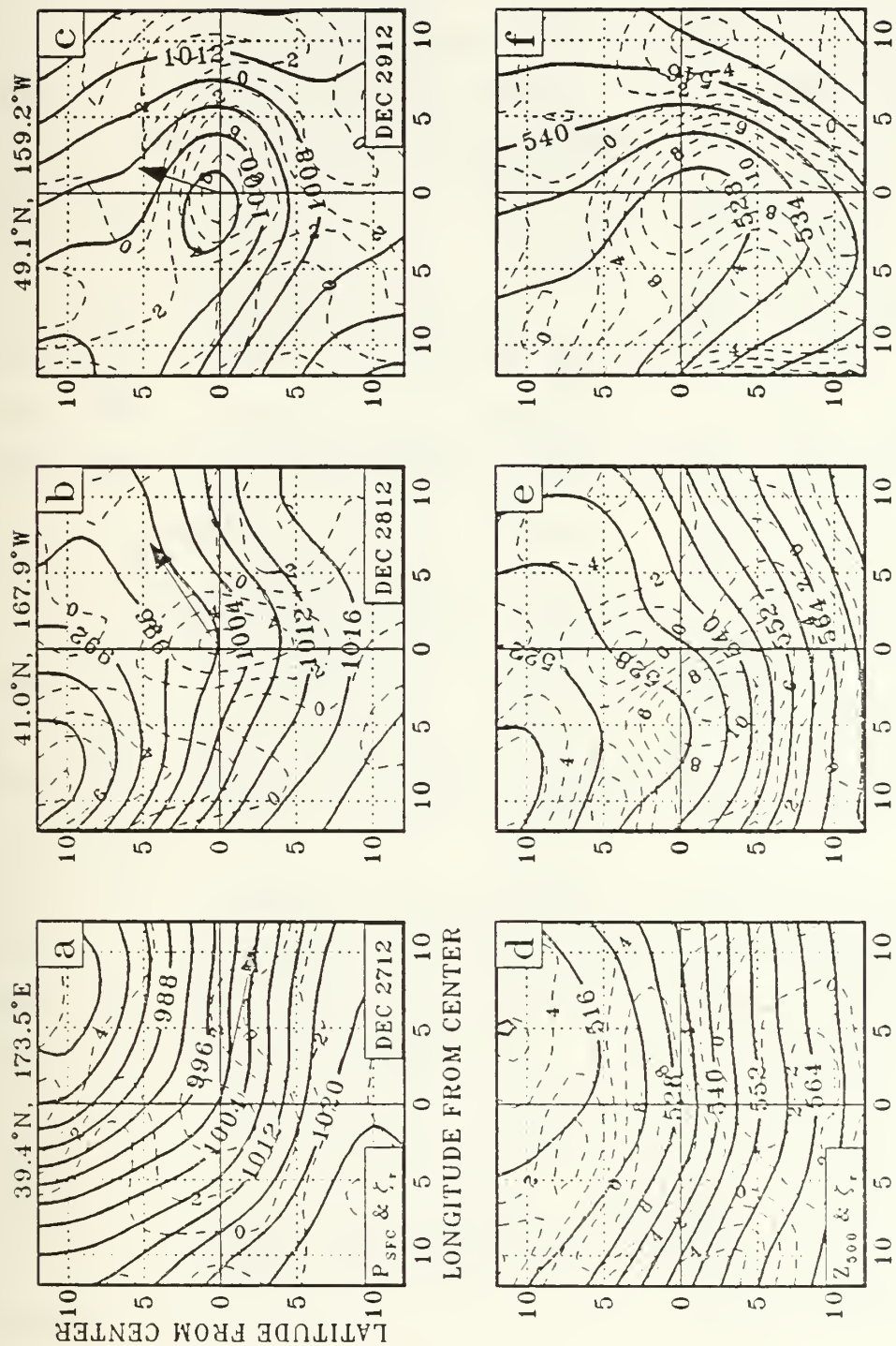
Fig. 4.4. (a-c) As in Fig. 4.1 except for FGGE Type II with dates indicated in lower right (2712 means 1200 GMT 27 December, 1978).
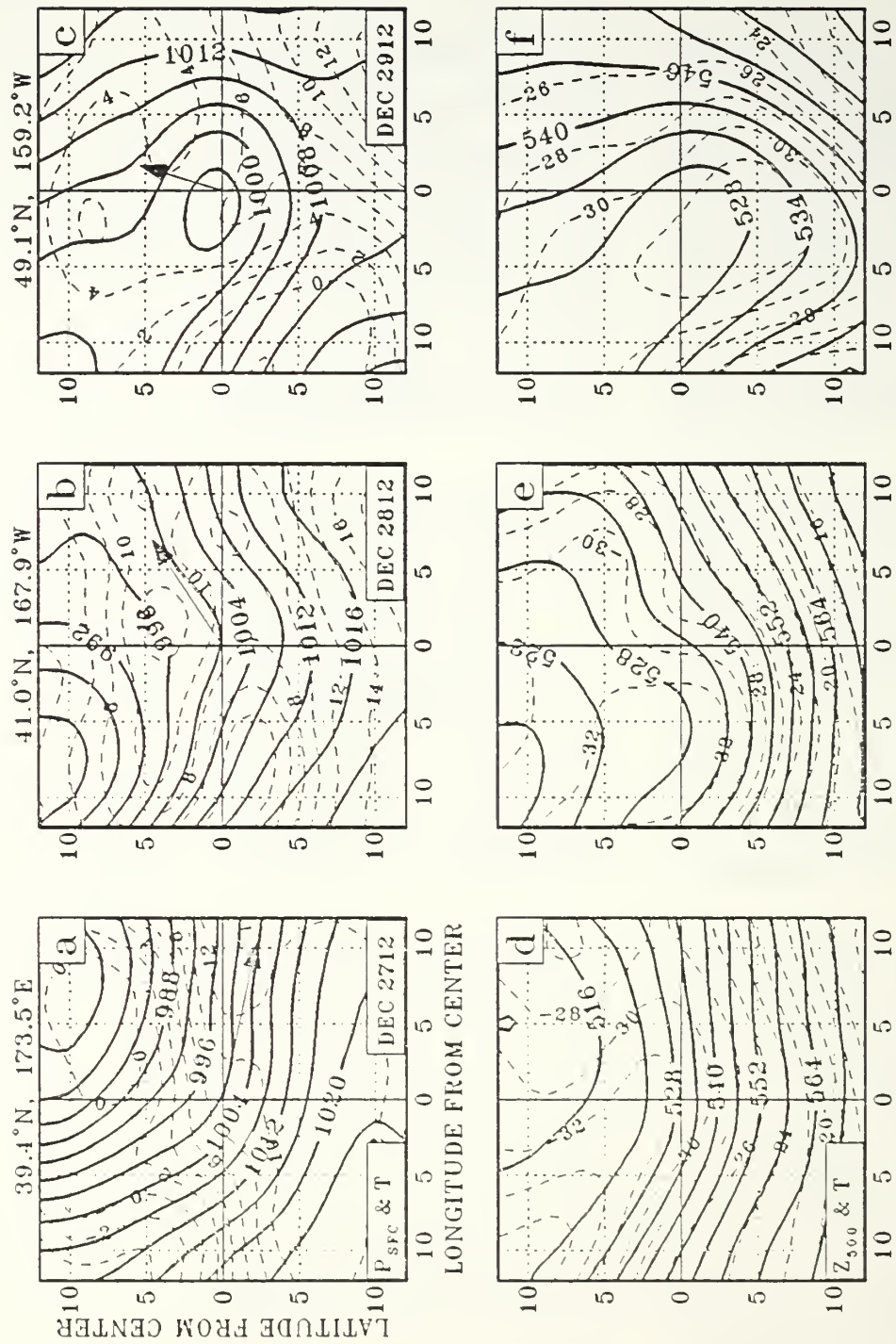
Fig. 4.5. As in Fig. 4.3 except for FGGE Type II.

100

The isotach analysis (Fig. 4.6 a-c) indicates that the polar low formed at the left exit region of a 50 m s^{-1} jet streak at 300 mb (Fig. 4.6 a). After 24 h, a 65 m s^{-1} jet streak was located about 1000 km to the south of the disturbance center (Fig. 4.6 b). The strength and position of the upper-level wind speed maximum is similar to that for the NOGAPS Type II case. The maximum wind speed aloft is nearly double that for the two Type I polar lows studied.

The ascent which occurred to the east of the surface development (Fig. 4.6 d-f) does not exhibit the comma-shaped signature shown by the NOGAPS case (Fig. 4.2 d-f). The more noisy FGGE analysis is probably due to data uncertainty. Upward motion is generally weaker than for the NOGAPS storm.

3. Summary

The Type II polar low forms in strong surface flow on the cyclonic side of the upper jet, and is accompanied by appreciable baroclinity throughout a deep layer. The use of model-generated data permits early detection of the incipient surface wave and the accompanying upper-level flow, and shows that a pre-existing upper-level trough and associated PVA are required for formation of the Type II disturbance in the model. Unlike the Type I lows described earlier, there is no initial closed circulation associated with the Type II surface disturbance. Thus, it may be difficult to detect the early stages of such a development with observational data. At later stages, it is not possible to discriminate between Types I and II, since an amplifying upper-level wave and associated PVA is coupled with the intensifying low-level cyclone in both cases.

A major difference between these Type II disturbances and the Type I polar lows studied earlier is the stronger initial flow in which the Type II low is embedded. Wind speeds vary from around 15-20 m s^{-1} at the surface to
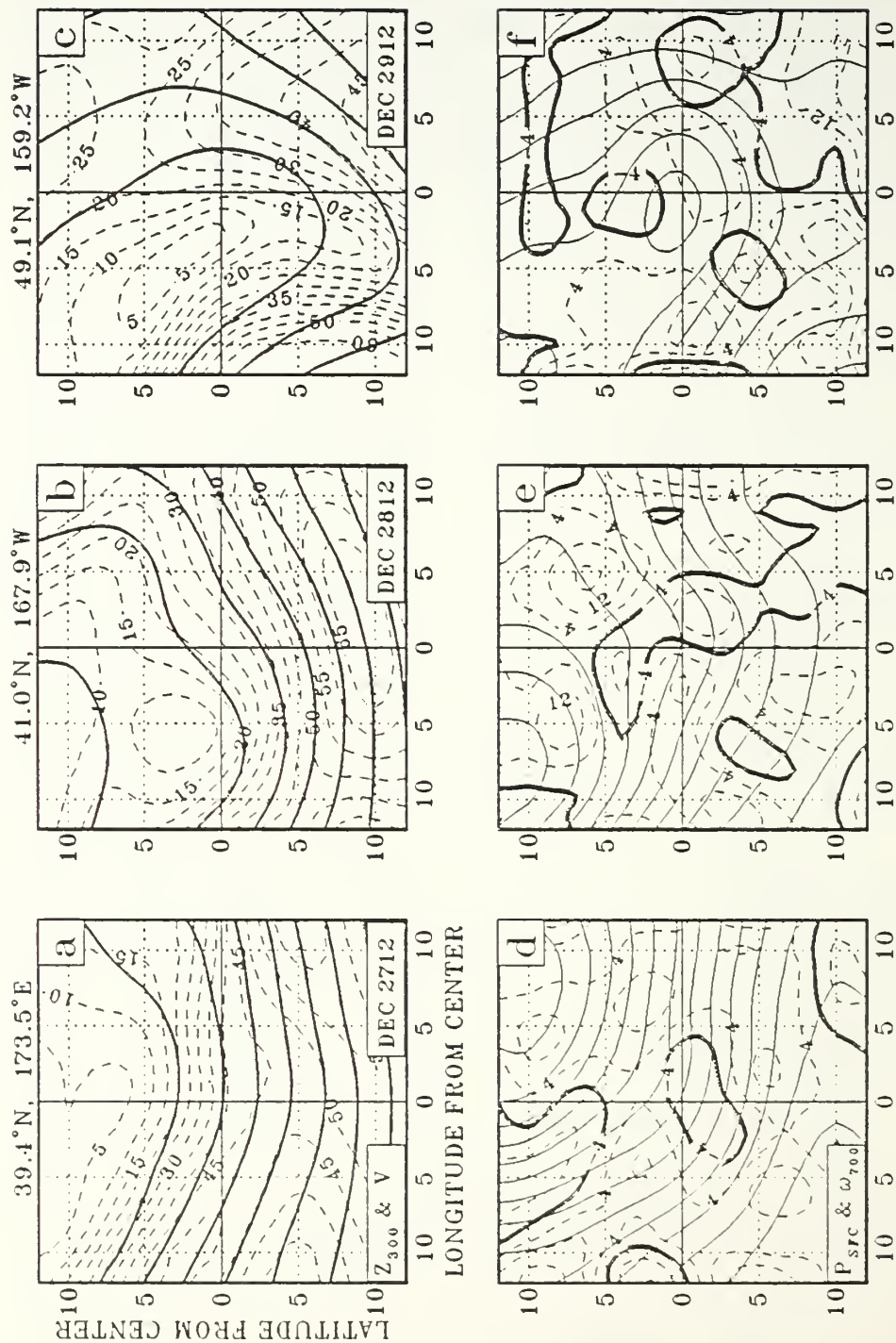
Fig. 4.6. As in Fig. 4.2 except for FGGE Type II.

102

50-60 m s⁻¹ at 300 mb. Corresponding typical values for the Type I polar lows are 0-10 m s⁻¹ at the surface to around 35 m s⁻¹ aloft. Although vertical wind shear (and therefore baroclinity) is similar for the two polar low types, the initial presence of strong surface wind suggests that surface fluxes of heat, moisture and momentum (friction) are important in the formation of the Type II polar low.

In the next sections, mass, vorticity, heat and moisture budgets will be presented to illustrate development of the Type II polar lows. An additional objective of this analysis is to determine the reasons why some polar lows form under straight upper flow (Type I) while others require the presence of upper-level PVA at genesis (Type II).

B. MASS AND VORTICITY ANALYSIS

1. NOGAPS Case

Mass transport terms for the simulated polar low are presented in Fig. 4.7. The horizontal mass flux convergence (Fig. 4.7 a) has a two-layer structure similar to the Type I disturbance (Fig. 3.7 a) with a deepening convergent layer below a layer of mass outflow. The kinematically-derived vertical velocities (Fig. 4.7 b) increase strongly during the first nine hours of development, and are accompanied by increasing low-level convergence (Fig. 4.7 a). This is followed by a period of weaker, but pulsating growth. Thus, growth of the mass circulation is more rapid than for the Type I case. As described earlier, the 12-h oscillation in the mass circulation is an artifact of the external gravity wave propagating within the NOGAPS model.

Cyclogenesis commences near the surface and later extends throughout the troposphere (Fig. 4.8). Initially, there is weak anticyclogenesis aloft. Vorticity increases in the low troposphere coincide with enhanced low-level

LATERAL MASS FLUX CONVERGENCE
(9.89×10^{14} kg per day)

ω (mb per hour)
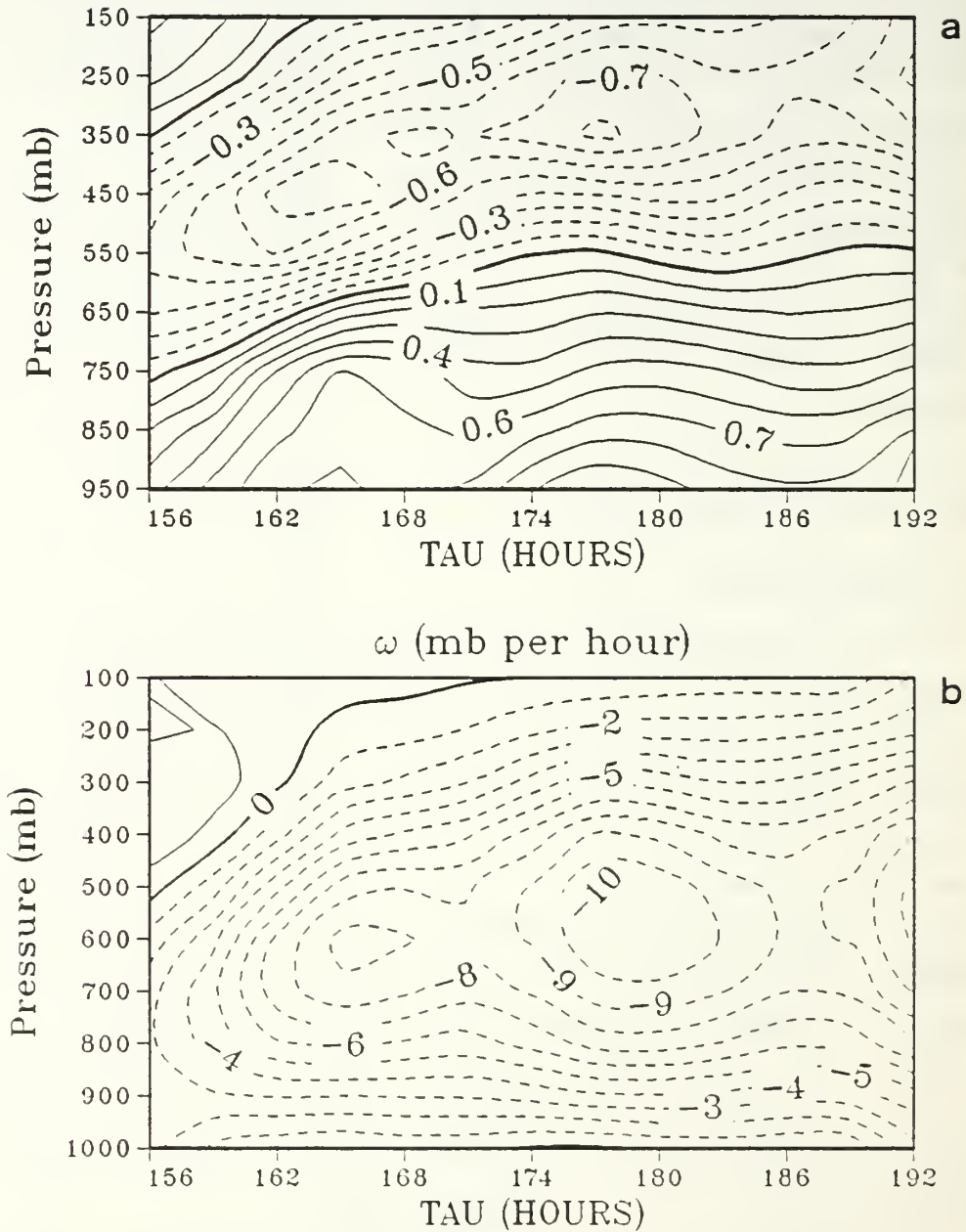
Fig. 4.7.   (a) Time evolution of lateral mass flux conver-
gence in 5° latitude radius volume for NOGAPS
Type II. Positive (solid) values indicate inflow.
(b) Area-averaged vertical p-velocity (mb h^{-1}).
Positive (negative) values are solid (dashed).

104

convergence (Fig. 4.7 a). Thus, development of the surface
cyclone appears to occur in response to the increasing mass
circulation evident in Fig. 4.7.

$$\delta\zeta/\delta t$$
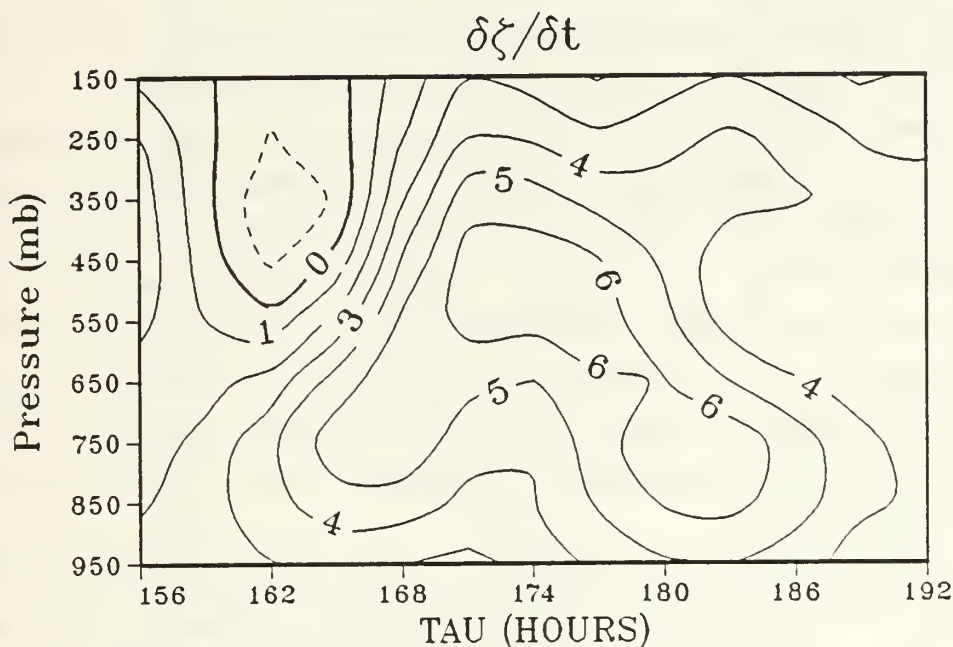
Fig. 4.8.   Time evolution of quasi-Lagrangian absolute
vorticity tendency (10^{-5} s^{-1}) for NOGAPS
Type II.

The peaks of low-level cyclogenesis at 168 h and at
180 h (Fig. 4.8) correlate well with the mass circulation
maxima (Fig. 4.7) at these times. However, this "pulsing" of
vorticity increases appears to be partially modulated by the
12-h gravity wave which is an artifact of NOGAPS. This
illustrates a disadvantage of the 3-h data resolution. At
this resolution, much of the inherent noisiness of the model
becomes evident. However, time averaging can be used to
filter out this undesirable noise, while preserving the
slower meteorological modes.

Vorticity budget results are presented in Fig. 4.9.
Over the first 12 h, the upper-level PVA term (Fig. 4.9 d)
exceeds 10 x 10^{-5} s^{-1} per day. It is this initial presence

of strong PVA which characterizes the Type II polar low. By comparison, the average PVA for the Type I storm is less than 4×10^{-5} s^{-1} per day over the first 21 h of development (Fig. 3.10 d). PVA for the Type I storm becomes large only at later stages of development as amplification of the upper waves occurs in conjunction with self-development.

The large PVA at early stages of storm development is offset by strong upper-level divergence (Fig. 4.9 d). This is consistent with the growth of the vertical mass circulation during this time, and the resulting generation of low-level vorticity. Twisting (Fig. 4.9 g) accounts for a significant loss of vorticity below 500 mb. This is a result of the localized nature of the initial vertical motion (large horizontal gradients of omega) in a strongly baroclinic environment.

As development occurs, vorticity increases occur throughout the depth of the troposphere (Fig. 4.9 b,c). Aloft, this generation is largely the result of PVA, and is partially offset by divergence (Fig. 4.9 e,f). Nearer the surface, generation is due to convergence with sinks arising from vertical eddy divergence (Fig. 4.9 h,i) and friction. Thus, the vorticity budget at later stages of this case is very similar to that for the Type I storm (Fig. 3.10).

The horizontal distributions of the terms in the vorticity equation at 500 mb are shown in Fig. 4.10. At the initial time, PVA (Fig. 4.10 a) dominates the area directly above and to the west of the surface disturbance. This is compatible with a strong vorticity gradient along the flow in these locations (Fig. 4.1 d). Since the wind velocity at this level exceeds the translation speed of the disturbance, the quasi-Lagrangian vorticity advection is large and positive. The maximum contribution from the divergence term (Fig. 4.10 d) occurs a little to the east of the center. Vertical advection and twisting effects (not shown) are
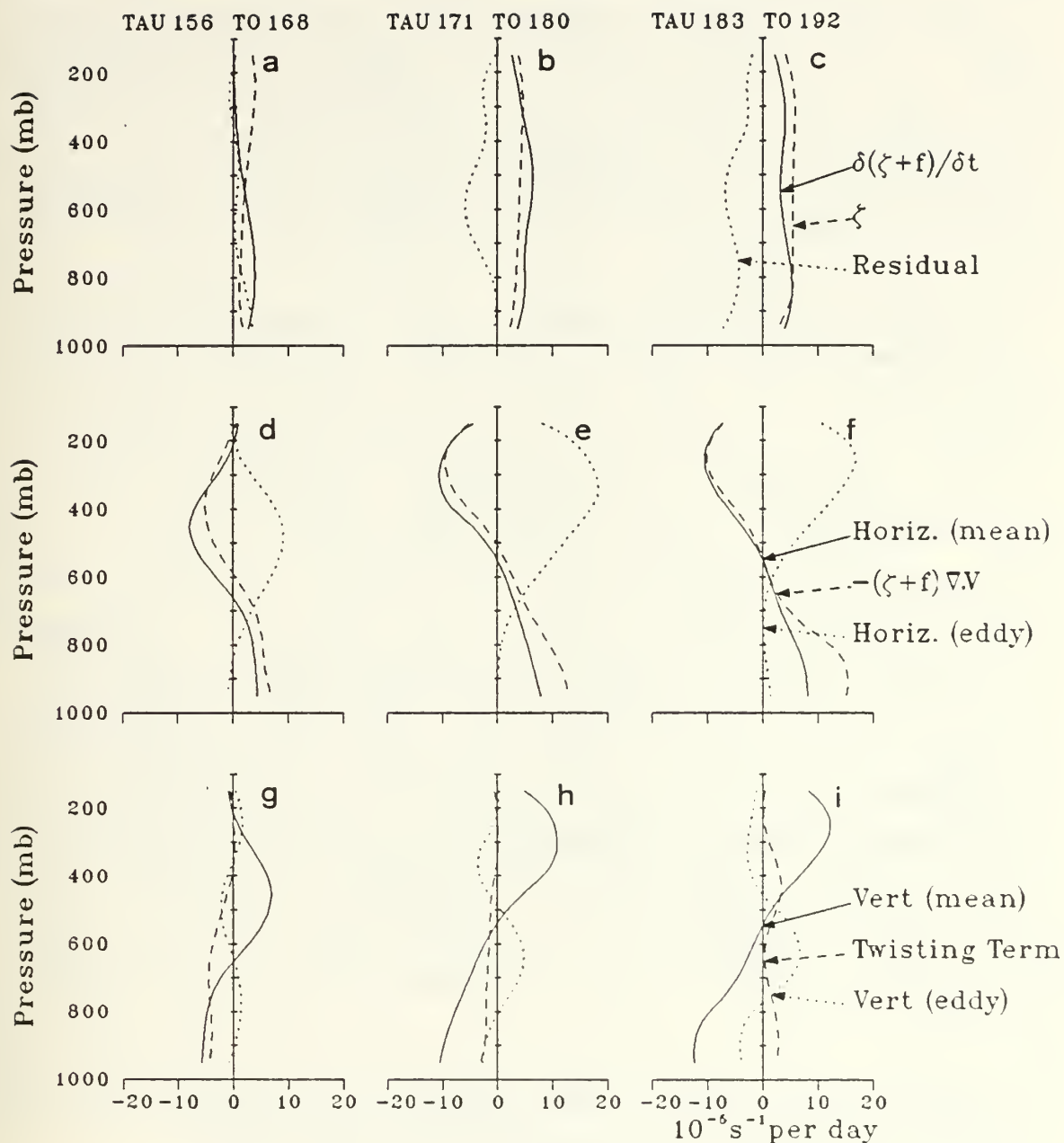
Fig. 4.9.   Vorticity budget terms for same volumes as in
             mass budget for NOGAPS Type II. Budget terms
             (described in text) are indicated in the legend
             on the right side. Times are indicated at the
             top of the figure.

107

small. The net quasi-Lagrangian vorticity tendency (Fig. 4.10 g) is an increasing (decreasing) vorticity to the west (east) of the center, which indicates amplification of the upper wave. This dipole of vorticity tendency is considerably larger than that at the initial stage of the Type I polar low (Fig. 3.11 g). This suggests that the amplification of the upper wave is more rapid for the Type II polar low.

At later stages in this storm, strong PVA extends in a band from directly above the surface low center to east of the low (Fig. 4.10 b,c). This is consistent with the eastward extension of the area of positive vorticity in Fig. 4.1 e. The strong PVA to the southwest of the low center is associated with a mobile short wave trough just off the western edge of the domain. The vigorous mass circulation causes a strong dipolar contribution from the divergence term (Fig. 4.10 e). In the trough, convergence is very efficient in generating vorticity due to the already high values of vorticity (see Fig. 4.1 e). Although the divergence sink exceeds PVA ahead of the storm, an additional positive contribution from both vertical advection and twisting (not shown) occurs in this location, and results in a net positive tendency (Fig. 4.10 h). The tendency patterns at this time, and at the end of the sequence (Fig. 4.10 i) are remarkably similar to those at the end of the Type I NOGAPS storm (Fig. 3.11 i), with positive tendency to the east and southwest of the center. This suggests that the later evolutions of the Type I and II storms are similar.

2. FGGE Case

The mass budget analysis for the FGGE case shows a deepening layer of convergence below upper-level outflow (Fig. 4.11 a). The strength of the mass circulation peaks at 1200 GMT 28 December, and decreases thereafter (Fig. 4.11
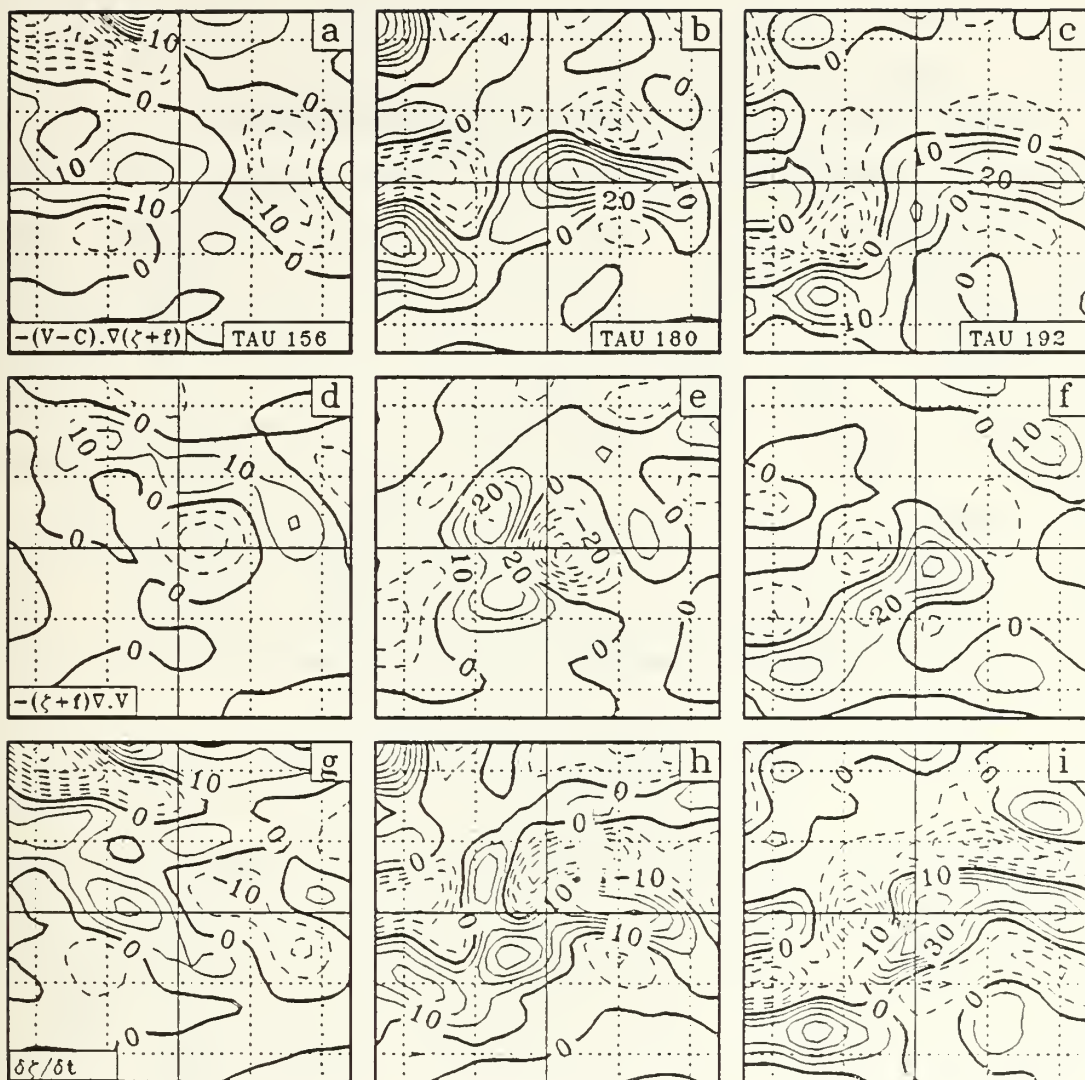
Fig. 4.10.   Vorticity equation terms at 500 mb for NOGAPS
Type II. (a-c) Absolute vorticity advection;
(d-f) convergence term; (g-i) quasi-Lagrangian
absolute vorticity tendency. Format as in Fig.
4.1 except axis labels and center coordinates
omitted for clarity. Units are 10^{-5} s^{-1} per
day. Heavy solid line is zero contour, and solid
(dashed) lines are positive (negative) values.

b). The minimum area-averaged omega of just under -5 mb per h is about half that for the NOGAPS case. In the NOGAPS case, a much broader maximum in the mass circulation is evident. Omega values below -8 mb per hour extend over a 30-h period (Fig. 4.7 b). A similar difference was observed between the FGGE and the NOGAPS Type I cases described earlier (compare Figs. 3.7 and 3.8). This difference highlights a model weakness. In nature, strong vertical ascent associated with a particular weather system is usually short-lived as the system undergoes the cycle of growth, maturity and decay. This is evidently the case for the FGGE examples (see Figs. 3.8 and 4.11). In contrast, the NOGAPS model appears to systematically sustain strong vertical ascent over a period of 2 to 3 days (Figs. 3.7 and 4.7). Another possible explanation for the weaker vertical motion in the FGGE case is that the vertical motion is averaged over a larger area due to data distribution.

The vorticity tendency time section for this Type II FGGE case (Fig. 4.12) s ows that cyclogenesis commences near the surface and extends throughout most of the troposphere by the end of the period. This cyclogenesis peaks at 0000 GMT 29 December, which is about 12 h after the maximum in the mass circulation. The strongest vorticity tendency is about half that of the more vigorous NOGAPS Type II case (see Fig. 4.8).

Vorticity budget results are shown in Fig. 4.13. During the first 12 h of development, a shallow surface-based layer of cyclogenesis occurs (Fig. 4.13 a, see also Fig. 4.12) as a result of low-level convergence (Fig. 4.13 d). This vorticity generation is strongly offset by friction, as inferred from the negative vorticity budget residual in Fig. 4.13 a. In most bulk representations of the PBL, friction appears in the momentum equation as the vertical gradient of the vector eddy stress, which in turn

110

LATERAL MASS FLUX CONVERGENCE
$(9.89 \times 10^{14}$ kg per day$)$

ω (mb per hour)
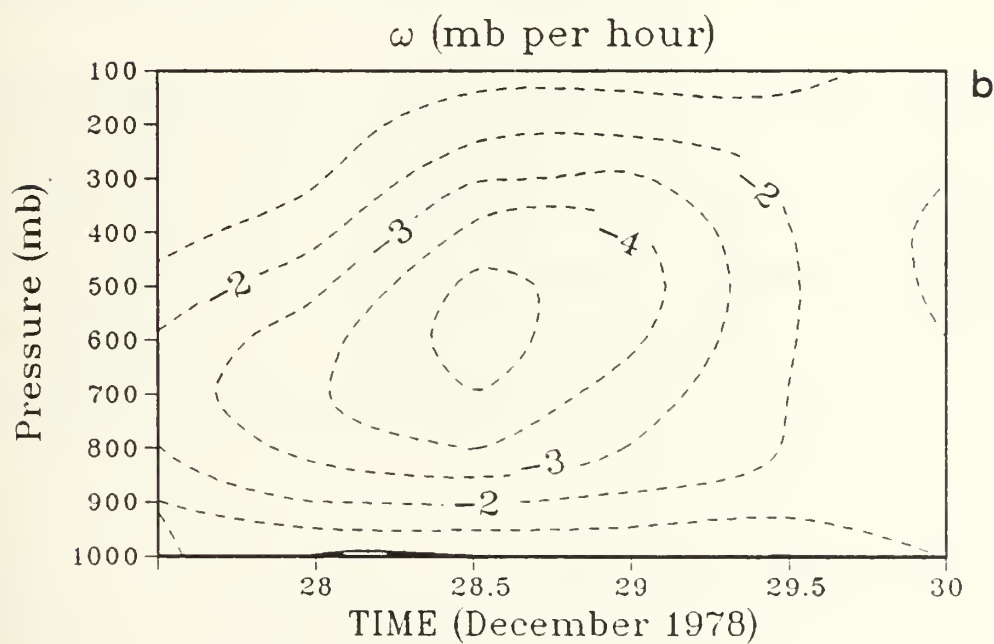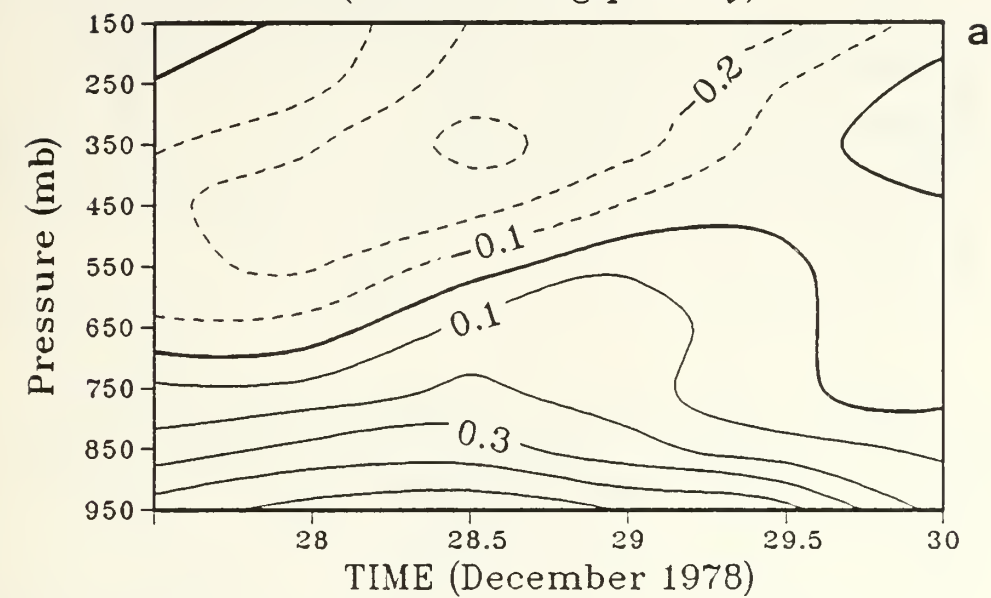
Fig. 4.11. As in Fig. 4.7 except for FGGE Type II.
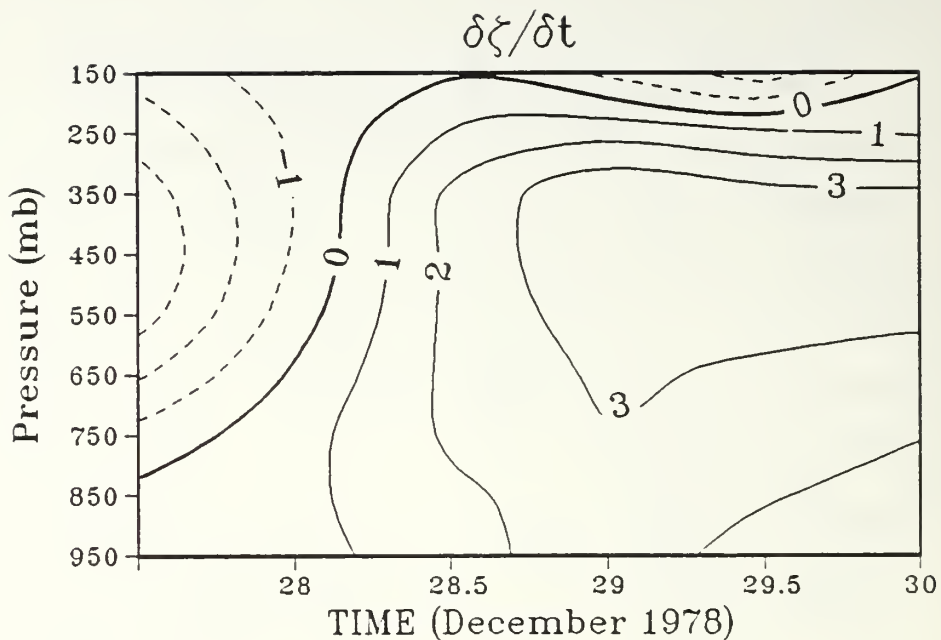
Fig. 4.12. As in Fig. 4.8 except for FGGE Type II.

is proportional to the product of the surface wind speed and the surface wind vector. As a first approximation, the frictional sink of vorticity is proportional to the product of the surface vorticity and the surface wind speed. Thus, frictional dissipation of cyclonic vorticity is largest when the surface flow is strong and cyclonic, as is the case in Fig. 4.4 a. Friction opposes development of a disturbance in the strong cyclonic surface flow such as in the initial stage of Type II polar lows. By contrast, surface friction is minimal at initial stages of the Type I polar low, since surface wind speeds are small.

The vorticity budget at early stages of the NOGAPS Type II polar low indicates a small positive residual (Fig. 4.9 a), which would appear to contradict this argument. However, in the NOGAPS case, the initial area-averaged vorticity is close to zero. It is possible that frictional
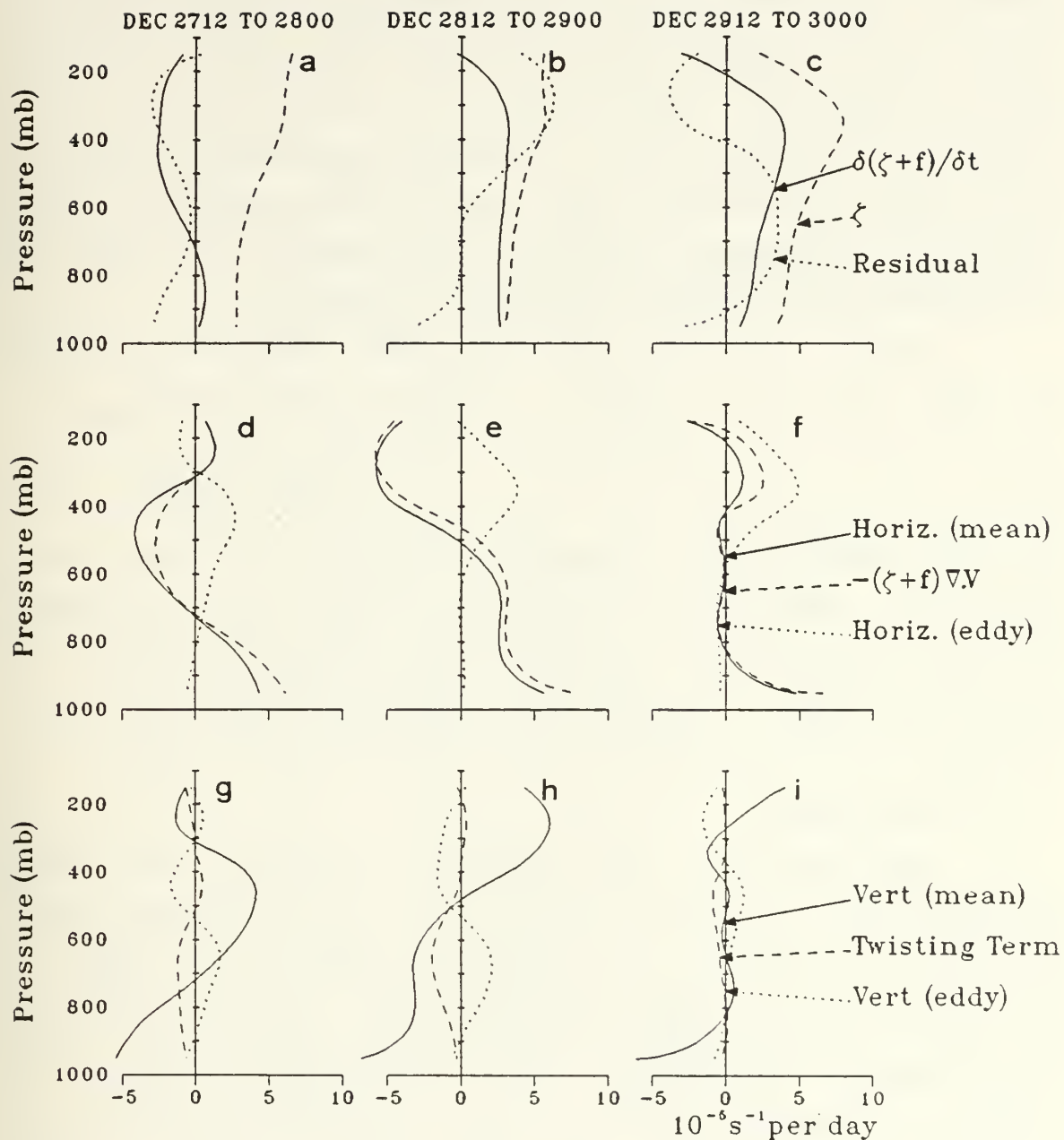
Fig. 4.13.   As in Fig. 4.9 except for FGGE Type II.

dissipation of cyclonic vorticity near the disturbance center is more than offset by dissipation of anticyclonic vorticity in surrounding areas included in the budget volume, which results in a small positive budget residual. In that case, and in both the Type I vorticity budgets (Figs. 3.10 a-c and 3.21 a-c), the budget residual becomes increasingly negative at later stages of development. This indicates increasing frictional dissipation of cyclonic vorticity as the surface circulation increases.

Aloft, the FGGE vorticity budget indicates a strong vorticity sink from divergence, which is offset by PVA (Fig. 4.13 d,e). At later stages, the contribution from the divergence term is smaller due to the reduced vertical mass circulation (see Fig. 4.11). The vorticity budgets for this case, and for the Type I FGGE case (Fig. 3.21) yield residuals of comparable magnitude to the leading terms. Therefore, the estimates of the various budget terms are of dubious accuracy. By contrast, the model-generated data permitted reliable diagnoses of vorticity budget terms.

3. Discussion

The evolution of vorticity features has been described for two Type II polar lows. The analysis shows that PVA associated with an advancing upper-level trough is important at early stages of development. Amplification of the upper wave is evident at early stages, especially in the trough where convergence is an efficient source of vorticity. In contrast, the Type I polar low forms under straight or anticyclonic upper flow with initial growth of the downstream ridge. Because the vorticity in the location of the upper trough is comparatively low for the Type I polar low (see Fig. 3.1 d), convergence is less effective in amplifying the initial trough. In the Type I case, the upper ridge and the divergence are co-located, so the ridge

114

intensifies rapidly at early stages, in spite of the low
vorticity. In the Type II case, the initial presence of PVA
offsets the divergence sink, and development of the down-
stream ridge is minimal. At later stages, evolution of the
upper waves progresses similarly for both types. Finally,
surface friction appears to strongly oppose development of
the Type II disturbance due to the strong surface flow. The
presence of this strong surface flow represents an important
difference between Type I and II polar lows.

C.   THERMODYNAMIC ANALYSIS

    1.   NOGAPS Case

        Results of the heat budget calculation are shown in
Fig. 4.14. At initial stages of development, potential
temperature rises occur throughout a deep layer (Fig. 4.14
a). This warming is hydrostatically consistent with the
initial vorticity tendency profile (Fig. 4.9 a), which has
the strongest cyclogenesis near the surface. The largest
contribution to this warming is from the diabatic heating,
which is offset by the mean and eddy flux divergence terms
(Fig. 4.14 d). The diabatic heating at initial stages of
the Type I polar low (Fig. 3.15 d) is small by comparison.
This reflects the more rapid growth of the vertical mass
circulation in the Type II case. The budget results at
later stages of development are very similar to those for
the Type I low (see Fig. 3.15). The leading terms at this
stage are diabatic heating and the offsetting mean heat flux
convergence (Fig. 4.14 e,f). The eddy term (Fig. 4.14 h,i)
is small because the budget volume includes both cold and
warm advection.

        The heat budget shows that the most significant
differences between Type I and II polar lows occur at early
stages of development. The diabatic heating for the Type II

115
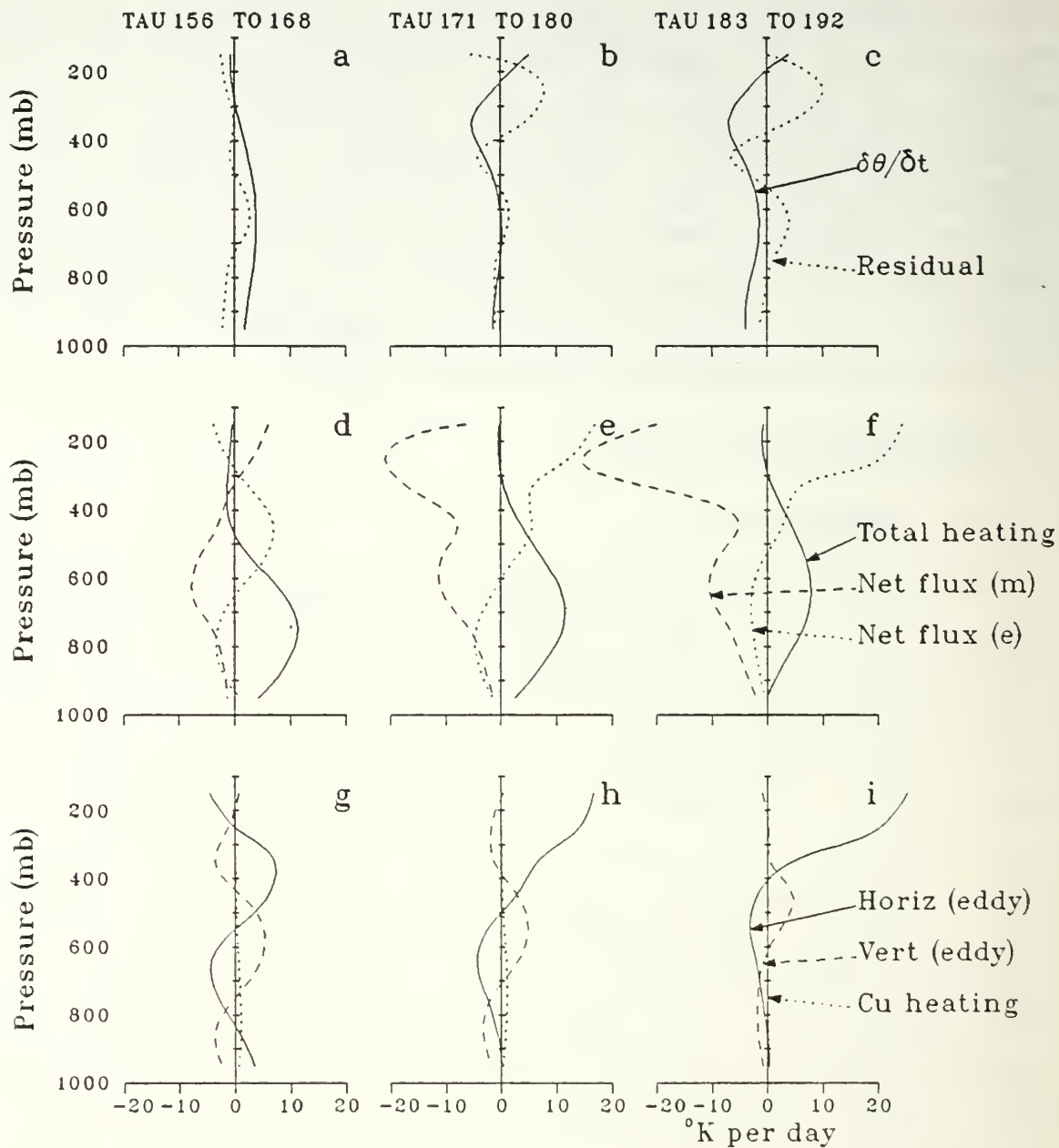
Fig. 4.14. Heat budget terms for NOGAPS Type II. Format as in Fig. 4.9.

polar low is significant at genesis and reaches a maximum during the first 6-8 h of development (Fig. 4.15 a). By contrast, much slower growth of diabatic heating is exhibited by the Type I storm (Fig. 3.18 a). At later stages of development, evolution of heat budget terms is similar for the two polar low types.

The Type II NOGAPS case appears to develop more rapidly at early stages than the Type I case. The early peaks in cyclogenesis (Fig. 4.8), diabatic heating (Fig. 4.15 a) and mass circulation (Fig. 4.7 b) correlate well with the strongest baroclinic conversion (Fig. 4.15 b). A later maximum of baroclinic conversion coincides with the second "pulse" of cyclogenesis. This correlation between storm intensification and the baroclinic conversion suggests that the storm grows as a baroclinically unstable wave.

A notable feature of the diabatic heating distribution in Fig. 4.15 a is the large surface heating rate of $7°K$ per day at polar low genesis. Large surface heat fluxes (Fig. 4.16 a) are caused by high surface winds (in excess of 15 m s^{-1} near disturbance) moving over warmer water (see Fig. 4.3 a). Since the fluxes are largest in the coldest air, their effect is to reduce the horizontal temperature gradient in Fig. 4.3 a. At later times, a dipolar pattern of surface heating (cooling)(Fig. 4.16 b,c) develops behind (ahead of) the intensifying surface trough. This heating pattern is in antiphase with the amplifying surface temperature wave (Fig. 4.3 a-c) and therefore opposes development. By comparison, surface fluxes for the Type I polar lows are weak because of light surface winds, especially at early stages of development. The presence of large surface heating is an important characteristic of the Type II polar low during formation and early development.

The moisture budget (Fig. 4.17) indicates that large accumulations of water vapor occur primarily as a result of

DIABATIC HEATING (°C per day)
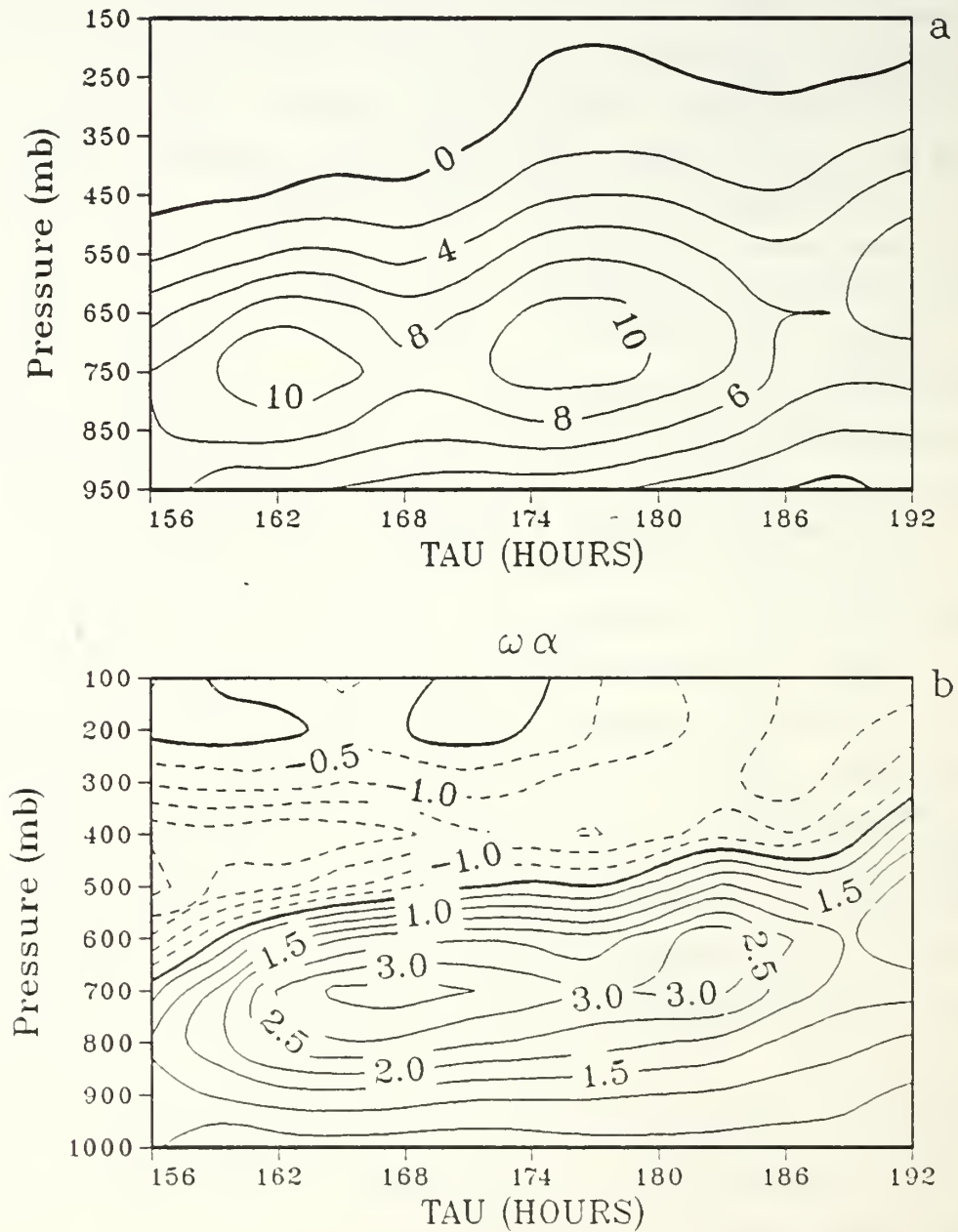
Fig. 4.15. (a) Time evolution of diabatic heating (°C per day) and (b) baroclinic conversion (mW Kg^{-1}) for NOGAPS Type II. Format as in Fig. 4.7.

118
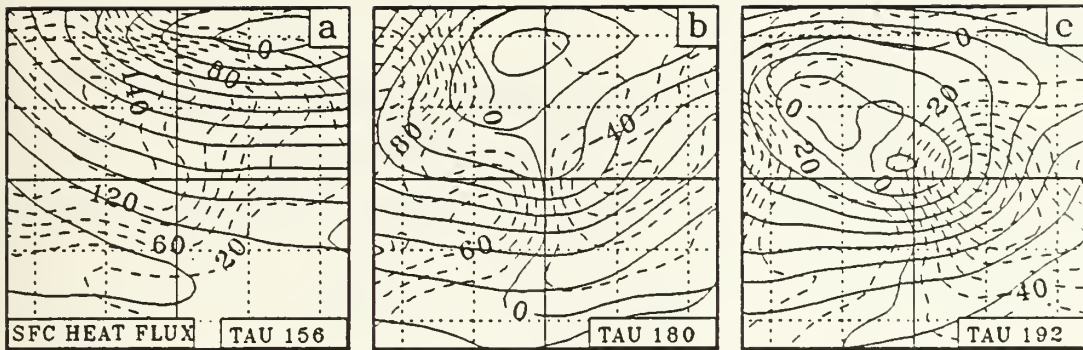
Fig. 4.16. (a-c) As in Fig. 4.1 a-c except surface sensible heat flux (Wm^{-2}, dashed)

the convergence of horizontal and vertical mean fluxes (Fig. 4.17 d-f). The eddy terms (Fig. 4.17 g-i) are weak by comparison. As this accumulation of water vapor exceeds the increase in vapor content, a strong sink (precipitation) exists in low-mid layers (Fig. 4.17 a-c). At the initial stage, the mean vapor content of the budget volume is increasing (Fig. 4.17 a). This is consistent with the initial warming trend (Fig. 4.14 a), since the saturation specific humidity increases with temperature. Therefore, a significant fraction of the flux convergence of water vapor contributes to an increase in the moisture content. The shallow surface layer of positive residual (Fig. 4.17 a) indicates that evaporation from the ocean is responsible for some of this moistening. Above the surface layer, the effects of horizontal convergence at lower levels, and vertical flux convergence at higher levels (Fig. 4.17 d) are

119

sufficient to ensure continued precipitation.   These flux
convergences in turn are the result of the increasing
vertical circulation.   The surface evaporation ensures that
the low-level inflow is sufficiently moist to sustain
continued precipitation.

The terms in the thickness tendency equation (3.4)
have been computed for the model-generated Type II distur-
bance (Fig.   4.18).   Quasi-Lagrangian thermal advection
patterns at the initial time (Fig.   4.18 a) present a dipole
of warming ahead of and cooling behind the developing
cyclone. Although this seems to contradict Fig. 4.3 a (which
indicates cold advection in all sectors), the thermal advec-
tion in Fig.   4.18 a is calculated relative to the storm,
which is translating to the east at about 23 m s^{-1}. When
this translation velocity is subtracted from the winds, the
storm relative motion ahead of (behind) the cyclone is
toward the cold (warm) air.   The intense warm advection to
the northwest of the center is also a consequence of the
quasi-Lagrangian calculation.   The diabat c heating to the
east of the low center (Fig.   4.18 g) almost exactly cancels
the adiabatic cooling (Fig.   4.18 d).   As a consequence, the
pattern of net thickness change (Fig.   4.18 j)   closely
matches the thermal advection (Fig.   4.18 a).   Since cooling
(warming) of a column results in falling (rising) geopoten-
tial at the top of the column,   these patterns result in
amplification of the upper waves.   This amplification is
evident in Fig.   4.10 g as discussed earlier.   Thus, the
contributions of thermal advection and diabatic effects to
self-development as described earlier for the Type I polar
low also apply to the Type II disturbance.

These self-development tendencies occur in a favor-
able environment of low static stability. Averaged over the
budget volume, the stability index is 3.7°K per 100 mb at
genesis, which is very close to the moist adiabatic rate.
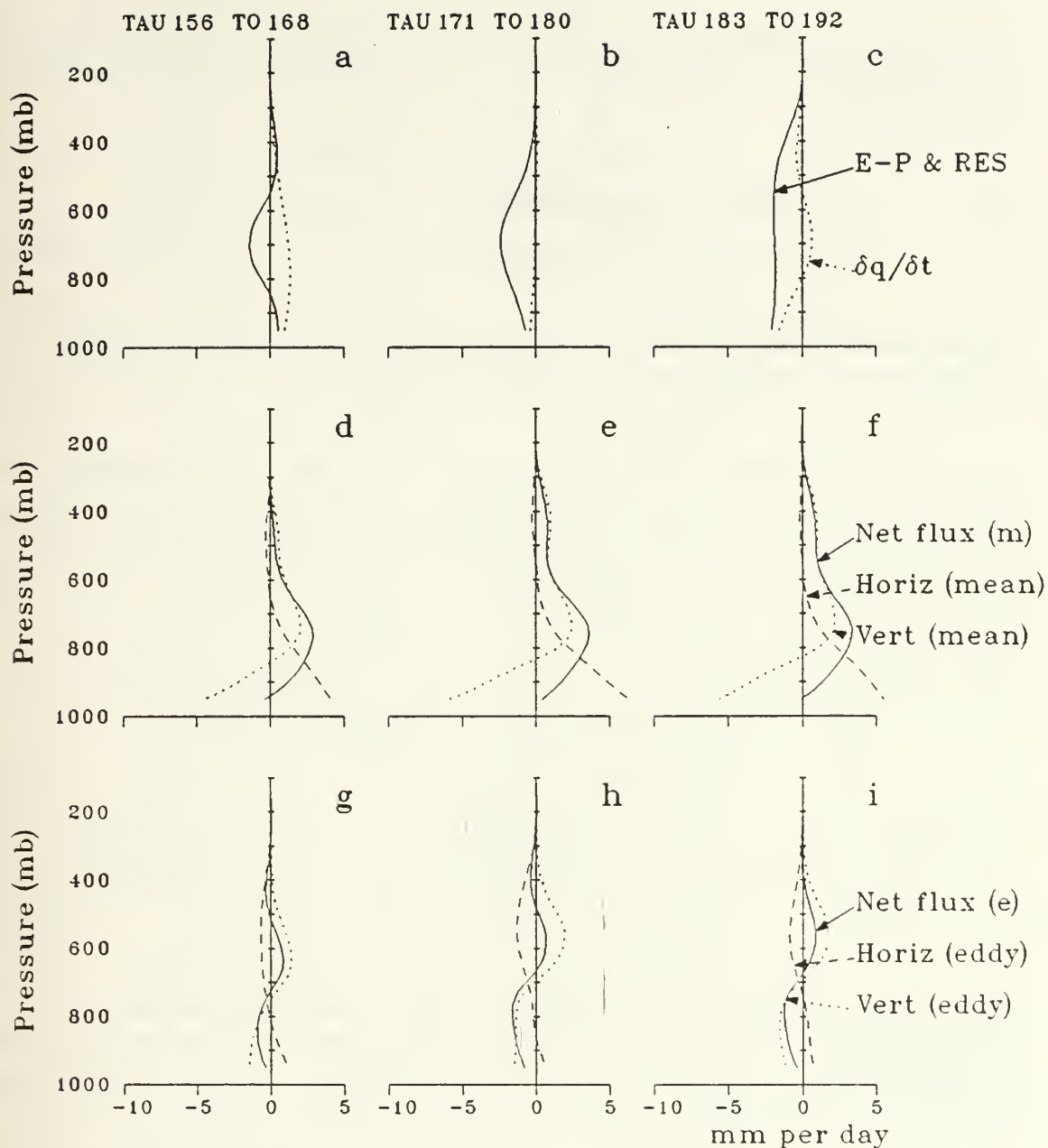
Fig. 4.17.   Moisture budget terms for NOGAPS Type II. Format as in Fig. 4.9.
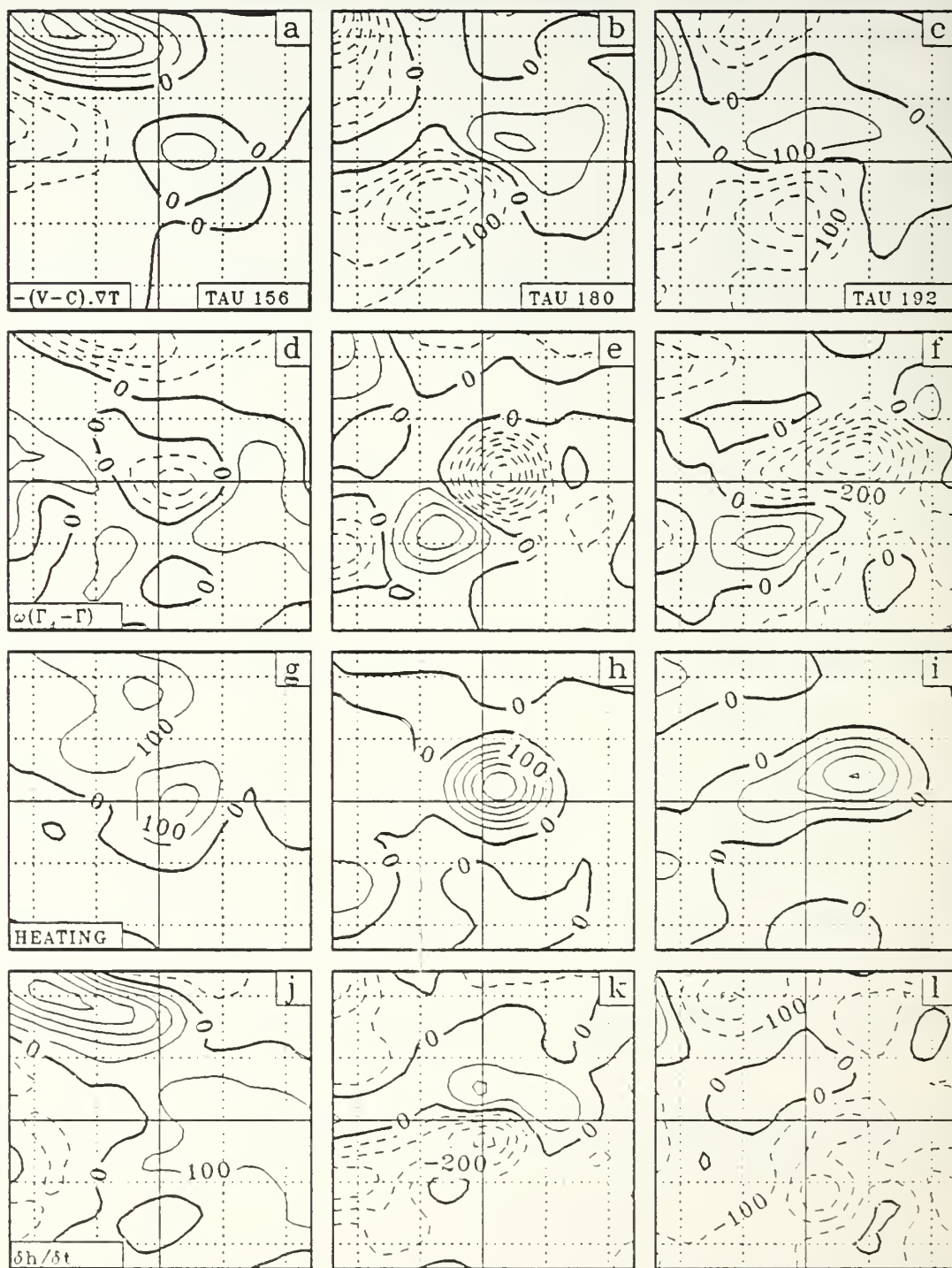
Fig. 4.18. Thickness tendency equation terms for NOGAPS
Type II. (a-c) horizontal thermal advection;
(d-f) vertical advection; (g-i) diabatic heat-
ing; (j-l) quasi-Lagrangian thickness tendency.
Format as in Fig. 4.10. Units are m day^{-1}.

122

Adiabatic warming associated with subsiding air near the western boundary of Fig. 4.18 d opposes the cold advection. Because this area is in the cold air where surface fluxes are large (see Fig. 4.16 a), the static stability is reduced and the braking effect due to subsidence is also reduced.

At later stages of development, there is a cyclonic rotation of the thermal advection patterns. This rotation is associated with amplification of the thermal wave. The net thickness tendency pattern (Fig. 4.18 k) is strongly fronto-lytic in the vicinity of the storm center, and frontogenetic to the south and southwest. This is consistent with the southward displacement of the upper jet streak relative to the center, since the largest thermal and geopotential gradients occur with the jet. Since the 500 mb flow above the low is southwesterly at this time, the thickness changes in Fig. 4.18 k indicate continued self-development of the upper-level features.

At final stages of the storm, the net tendency dipole (Fig. 4.18 l) has rotated further with largest cooling to the southeast of the center and weak warming to the northwest. This tends to produce a more vertical geopotential structure. Averaged over the domain, net cooling exists, in accordance with the heat budget (Fig. 4.14 c).

Cross-sections of potential temperature and Richardson number through the storm center at genesis are presented in Fig. 4.19. The reduced static stability in the western sector of Fig. 4.19 a, as implied by the widely spaced potential temperature contours, is consistent with the area of low Ri to the west of the low center. This is consistent with the preferred development of the upper trough and is a result of the strong surface heating in this sector. The deep layer of low Ri to the north of the low position (Fig. 4.19 d) is a combination of low static stability below about 600 mb, and enhanced baroclinity

aloft. The jet is located directly above the surface low position at this time. Therefore, the favored location for baroclinic development is in the reduced Ri layer just pole-ward of the jet.

2. FGGE Case

Heat budget results for the FGGE case are presented in Fig. 4.20. As with the Type I FGGE heat budget, the residual (Fig. 4.20 a-c) includes the effects of diabatic heating as well as data uncertainty and interpolation error. The horizontal eddy term (Fig. 4.20 g-i) is small because the translating budget area includes both cold and warm advection. The large contribution in the upper troposphere from the net mean flux convergence (Fig. 4.20 e,f) is not balanced by any other budget term. Since the mass budget is balanced, uncertainty in the temperature data may contribute to the anomalous magnitude of this term. In the NOGAPS heat budgets, a similar large negative contribution from the mean fluxes is offset by strong warm advection aloft (Figs 3.15 f and 4.14 f).

The time evolution of the heat budget residual term is presented in Fig. 4.21 a. Occurrence of diabatic heating in the upper troposphere of the intensity implied in Fig. 4.21 a is unrealistic. Therefore, this residual reflects data and computational uncertainty. In the heat budgets involving the complete model-generated data, considerable computational error occurred in the upper troposphere (Figs. 3.15 b,c and 4.14 b,c). This error occurs during the inter-polation from sigma to pressure levels, as suggested earlier. In the production of the FGGE level III-B data set used in this study, the first-guess predictions were obtained in sigma coordinates from the ECMWF numerical model (Bengtsson et al., 1982). Interpolation of these fields to pressure levels used cubic splines, as for the NOGAPS
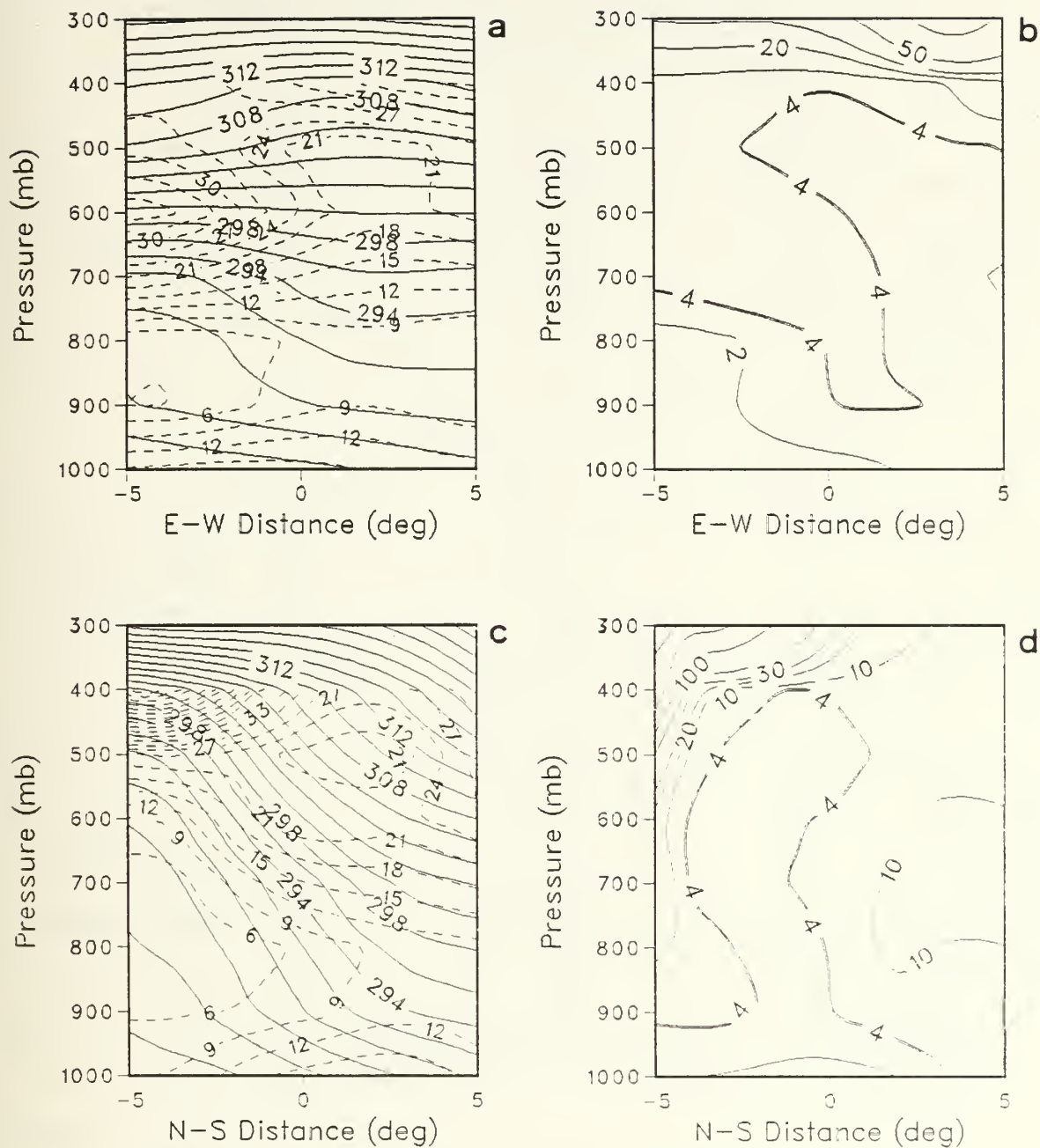
Fig. 4.19. (a) East-west cross-section of potential tem-
perature and static stability parameter (10^{-5}
$Pa^{-2}m^2s^{-2}$); (b)east-west cross-section of
Richardson number; (c) as in (a) except north-
south; (d) as in (b) except north-south.

125
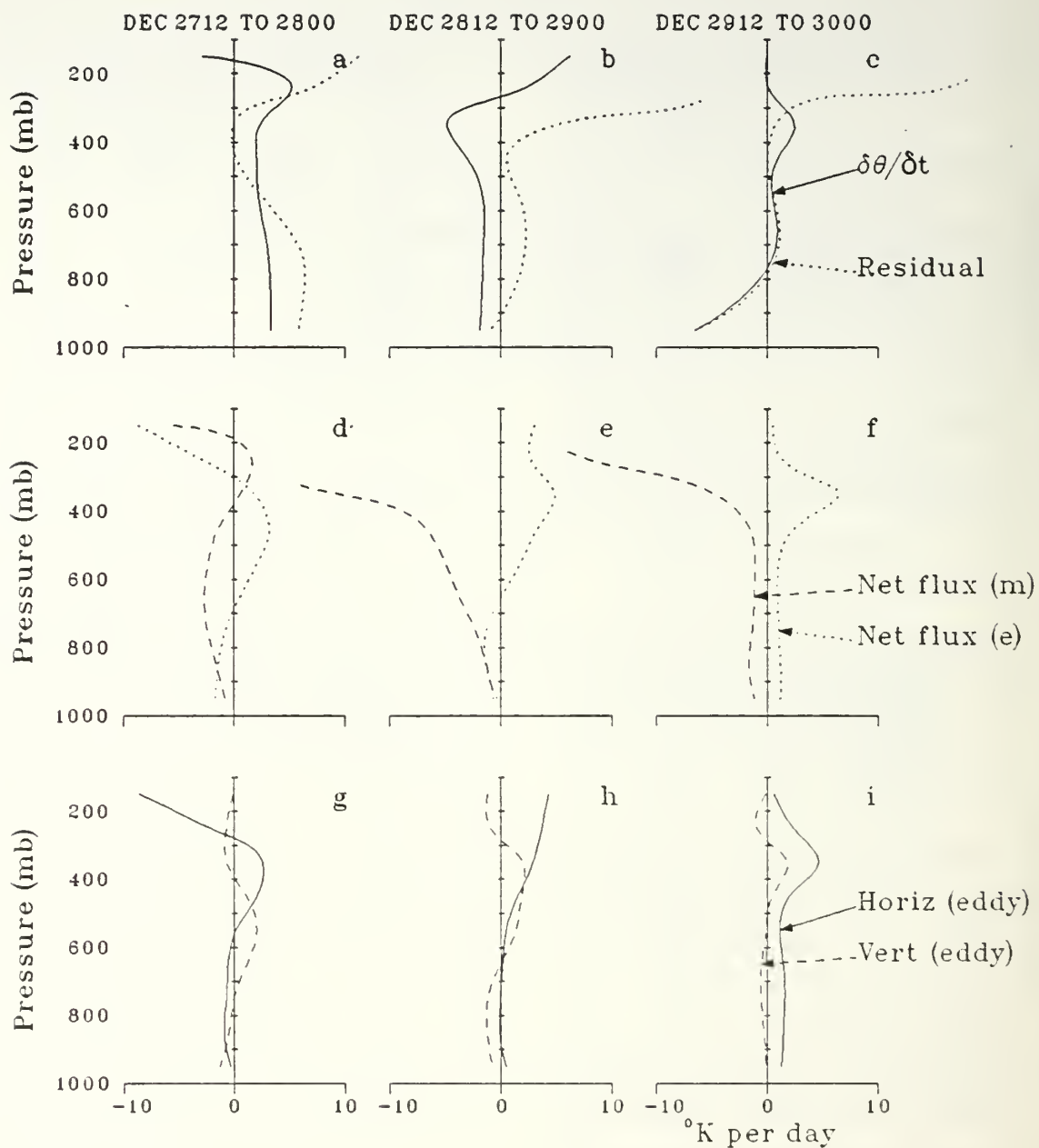
Fig. 4.20. As in Fig. 4.14 except for FGGE Type II.

126

fields. A possible additional source of uncertainty is the use of ECMWF model initialized temperatures in this study. The departure of these temperatures from layer temperatures computed hydrostatically from the geopotential data is largest in the stratosphere (Wash and Calland, 1985). This temperature uncertainty aloft undoubtedly contributes to the large residuals in Fig. 4.21 a.

At lower levels in the troposphere, diabatic heating from latent heat release and surface heat fluxes contributes to the heat budget residual in Fig. 4.21 a. In the NOGAPS cases, the diabatic heating was strongly modulated by the vertical velocity (note the similarity between Figs. 3.7 b and 3.18 a, and between Figs. 4.7 b and 4.15 a). The dissimilarity between the time sections of the heat budget residual (Fig. 4.21 a) and omega (Fig. 4.11 b) for this FGGE case shows that the residual is contaminated by data uncertainty. Strong surface fluxes at early stages possibly contribute to the positive residuals near the surface. At later stages, the negative residual at low levels appears to indicate surface cooling as the storm moves rapidly poleward (see Fig. 4.5 c).

The baroclinic conversion term (Fig. 4.21 b) indicates a thermally direct circulation (warm air rising, cold air sinking) throughout most of the troposphere. This is consistent with the previous cases studied and shows that this low grows through baroclinic processes. The magnitude of this term is about half that of the more vigorous Type II NOGAPS storm (Fig. 4.15 b).

The terms in the thickness tendency equation (Fig. 4.22) indicate the possibility of self-development. Although the braking term (Fig. 4.22 d-f) and the diabatic heating (Fig. 4.22 g-i) are rather noisy, patterns of thermal advection (Fig. 4.22 a-c) and net thickness tendency (Fig. 4.22 j-l) are more coherent. Thermal advection contributes

HEAT BUDGET RESIDUAL (°C per day)
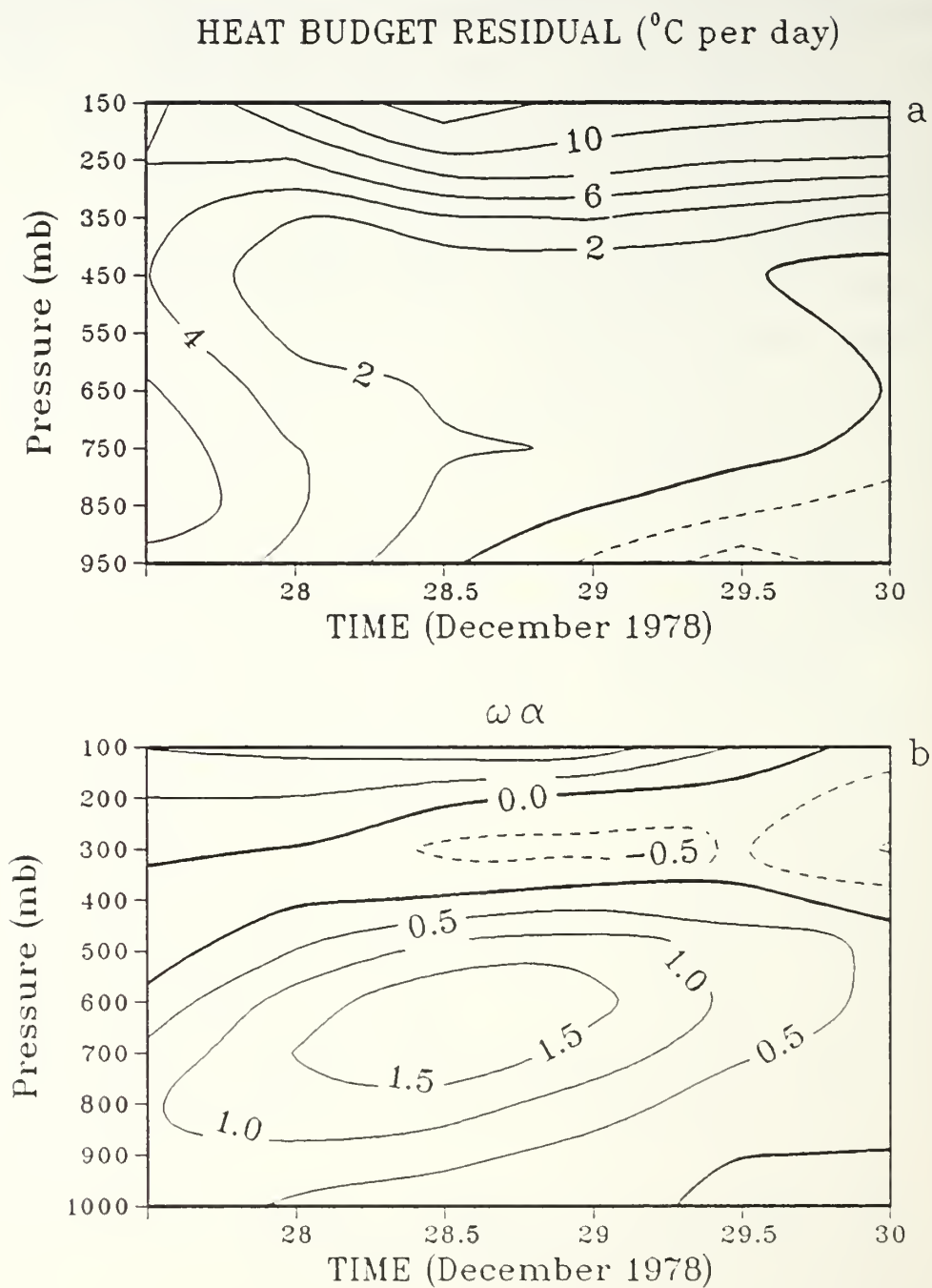
Fig. 4.21.   (a) Heat budget residual for FGGE Type II.
             (b) As in Fig. 4.15 b except for FGGE Type II.

warming (cooling) ahead (to the rear) of the surface low, which is favorable for self-development. As in previous cases examined, these patterns rotate cyclonically with time.

This analysis is subject to considerable uncertainty. Of the four terms in the thickness tendency equation, probably only the thermal advection is derived with any degree of confidence. The braking term is the product of two terms (vertical velocity and static stability) which involve horizontal and vertical differentiation and vertical integration. The diabatic term is obtained as a residual. Comparison of Figs. 4.22 d and g indicates that diabatic heating exceeds adiabatic cooling in the ascent region near the low center. This is consistent with the conditionally unstable lapse rates noted earlier. Only the net thickness tendency in Fig. 4.22 k shows thickness changes which are indicative of self-development. Because thickness tendencies are computed directly, tendencies at the beginning and end of the sequence (Fig. 4.22 j,l) are less reliable than those during the sequence (Fig. 4.22 k). In both the Type I and Type II NOGAPS examples, net thickness changes occurred which were in phase with the advective term. Using the model results as a guide to the interpretation of the FGGE case, it is probable that the sequence of self-development also occurred in this observed Type II polar low, as suggested by Fig. 4.22 k.

D. DISCUSSION

The quasi-Lagrangian analysis has shown that the Type II polar low is a baroclinic phenomenon initiated by upper-level PVA and intensified by low-level thermal processes. Continued storm intensification results from self-development, as for the Type I case. Because of the
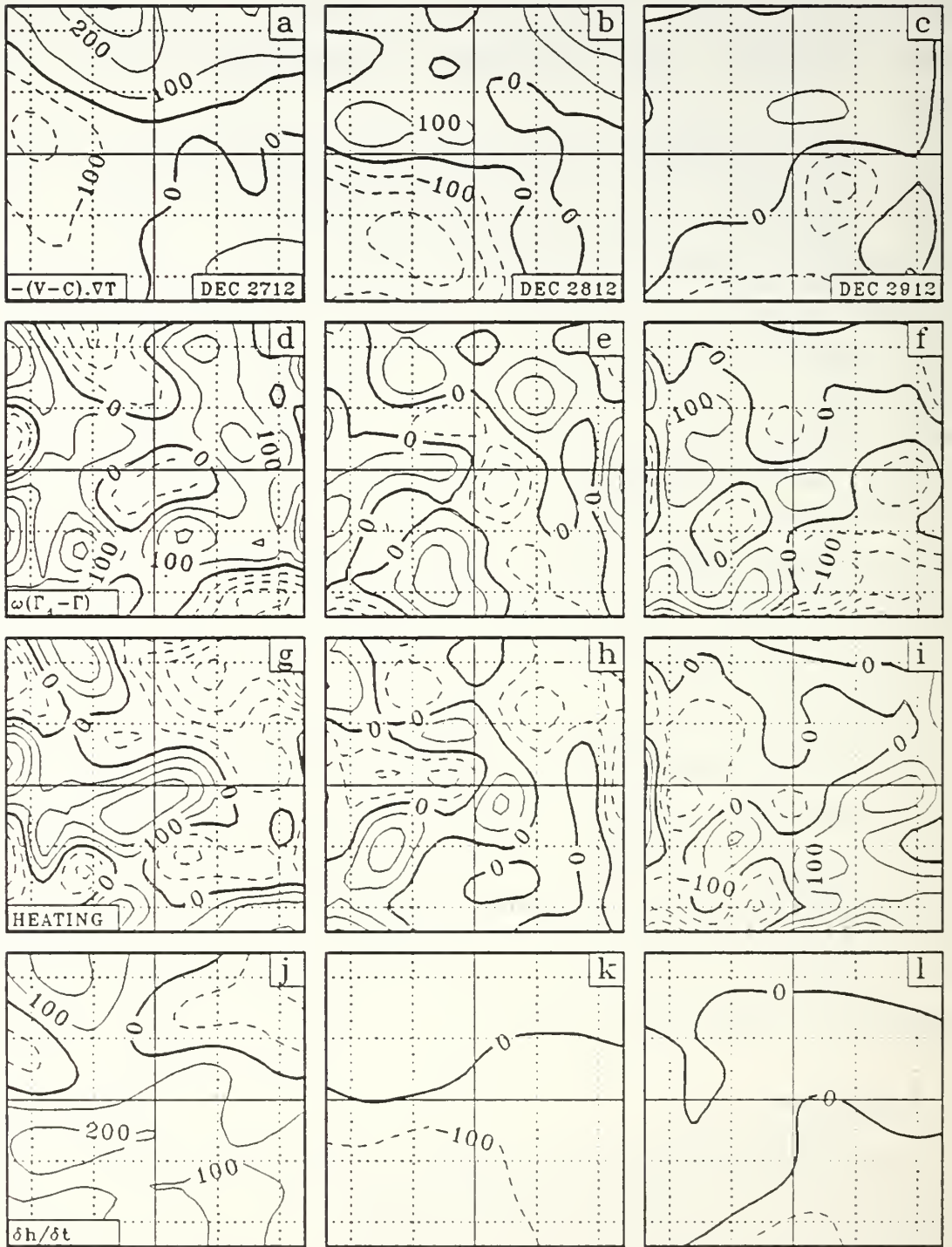
Fig. 4.22. As in Fig. 4.18 except for FGGE Type II.

initially strong surface winds, surface friction, heat and moisture fluxes are important at early stages of development.

In spite of the larger translation speeds of the Type II storms, the quasi-Lagrangian analyses yield vorticity and thickness tendency patterns that are qualitatively similar to the slower Type I polar low. In an Eulerian frame, local thermal and vorticity changes result from both wave amplification and translation. However, when viewed from a quasi-Lagrangian perspective, the large translation contribution is removed, and wave amplification is similar for the two types. Because baroclinic development is dependent on vertical wind shear, there is little apparent difference between a rapidly moving storm growing in a strong surface flow beneath a stronger upper jet (Type II) and a slow-moving disturbance in weak surface flow beneath a moderate upper jet (Type I).

In the maritime atmosphere, surface fluxes of momentum, heat and moisture strongly modify the large-scale environment. Because these fluxes are dependent on the surface wind velocity, they represent an important difference between Type I and II disturbances. In strong cold air outbreaks similar to Figs. 4.1 a and 4.4 a, enhanced surface friction opposes polar low development. Strong surface heating on the cold side of an intense baroclinic zone tends to reduce the surface temperature gradient to a magnitude comparable to the SST gradient. In addition, the heat fluxes oppose the thermal advection dipole associated with a perturbation in the surface flow. Therefore, the surface heat flux tends to exert a stabilizing influence on weak perturbations in the surface flow. This is consistent with Sandgathe (1981), who found that addition of the NOGAPS sensible heat flux weakened the low-level temperature gradient and resulted in less vigorous secondary lows. The damping effects of friction and

surface heating may explain why polar low developments do not occur in all strong cold outbreaks. However, Mansfield's (1974) conclusion that polar lows develop only when the surface winds are light is not supported by the cases studied here.

The tendency of friction and surface heat fluxes to stabilize the low-level flow suggests why the short-wave trough and associated PVA are required for the Type II polar low. When a perturbation in a strong surface flow develops in spite of the stabilizing influence of the large heat fluxes, an upper-level divergence maximum is required to sustain a vertical mass circulation. Surface convergence induced by this ascent causes low-level vorticity generation that leads to formation of a surface trough. As this low-level circulation increases in strength and vertical extent, the growing thermal advection eventually results in the onset of self-development.

A second contribution of the strong surface heating is suggested when the development occurs in a low static stability environment. An advancing trough aloft (with PVA ahead of it), coupled with strong surface heating, results in a further reduction of static stability in the column below the trough. Consequently, the subsidence heating which would have offset the strong horizontal advection aloft is reduced. With larger net cooling aloft, rapid growth of the upper trough occurs. Thus, surface sensible heating may play a dual role when the environmental static stability is already rather low, as is usually the case with the polar low (Mullen, 1979; Reed, 1979). Addition of heat near the surface in antiphase with the growing thermal perturbation opposes self-development at low levels. However, strong surface heating in a near-neutral environment may lead to further reductions in static stability throughout a deep layer of the troposphere. For the proper combination of

132

environmental static stability and strong surface heating, the self-development of the upper-level trough may be enhanced. In these special circumstances, it is hypothesized that strong surface heating in the cold air may indirectly contribute to surface low development.

Since formation of the Type II polar low is triggered by the vertical mass circulation, the reduced static stability region on the cold side of the jet is a favored location for development, especially when the surface heating is large. For a balanced upper-level jet, divergence is co-located with the PVA maximum near the left exit. For these reasons, the Type II low forms below an area of PVA on the poleward side of the upper jet. Intensification of this low-level cyclone occurs as it becomes coupled to a developing upper-level wave.

In the Type I polar low, the initial surface winds are light and the air-sea fluxes are small. In a baroclinic environment, the thermal advective effects are not significantly modulated by the stabilizing effect of the surface fluxes and the perturbation grows. Therefore, the disturbance forms near the maximum surface baroclinity. Because the baroclinic zone slopes toward the cold air, the surface low will form on the equatorward side of the upper jet. Since the Type I low forms as a low-level baroclinic disturbance, no initial PVA aloft is required. Subsequent development occurs in conjunction with an amplifying upper-level wave which is coupled to the developing surface cyclone.

Evaporation from the surface is an essential contribution to the moisture budget of the developing polar low. These fluxes ensure an adequate supply of moisture for precipitation. At later stages of development, latent heat release is essential for continued development. When Sandgathe (1981) withheld surface moisture fluxes, the secondary lows formed, but failed to develop significantly.

133

The heat and moisture budgets in this study verify that surface moisture flux is essential for polar low development.

V. COMPARISONS WITH NON-DEVELOPING CASES

In Chapters III and IV, it was shown that Type I and II polar lows grow through baroclinic processes and are modified by surface fluxes and latent heat release. Formation and growth of these disturbances is favored by the presence of reduced static stability, strong baroclinity and high humidity. However, before it can be concluded that these conditions are necessary and sufficient for cyclogenesis, the hypothesis that the absence of one or more of these conditions inhibits cyclogenesis is examined. For this purpose, two non-developing polar lows from the model-generated data set are examined.

In nature, there are many non-developing polar lows that remain as secondary disturbances and exhibit pressure deficits of only a few mb (Forbes and Lottes, 1982). Such non-developing disturbances may initially resemble Type I or II polar lows, but do not develop to the same degree. These disturbances continue to migrate about the parent low and are eventually absorbed into the mean flow. Comparisons between the initial state of these weakly developing disturbances in the numerical simulations and the more vigorously developing Type I and II cyclones will help to confirm the role of various physical processes in the growth of polar lows.

A. NON-DEVELOPING TYPE I DISTURBANCE

1. Synoptic Description

Selected synoptic fields for a non-developing Type I polar low are shown in Figs. 5.1 and 5.2. This disturbance forms in a strongly baroclinic surface environment (Fig. 5.1

a) under the right exit region of a 50 m s^{-1} jet streak (Fig. 5.2 a). The disturbance subsequently becomes embedded in the northwesterly flow (Fig. 5.1 b) around the parent cyclone, which is situated far to the northeast, and is eventually absorbed into the mean flow (Fig. 5.1 c) without significant development. The surface disturbance remains well to the equatorward side of the 300 mb jet (Fig. 5.2 b,c) throughout this period.

The initial 500 mb flow (Fig. 5.1 d) is only weakly disturbed, with the highest vorticity to the northwest in a broad tongue on the poleward side of the jet streak. NVA prevails directly above the low center, with an area of weak PVA centered about 200 km to the south. This PVA is associated with decreasing shear vorticity on the equatorward side of a weak secondary jet maximum just southeast of the disturbance center (Fig. 5.2 a). An area of weak upward motion (Fig. 5.2 d) occurs in this area. This area of ascent persists east of the surface center without intensification (Fig. 5.2 e,f). Subsequent development of upper features is slight, with a weak trough to the west of the disturbance center by the end of the period (Fig. 5.1 f). The areas of upper-level cyclonic vorticity and upward motion near the eastern boundary of Figs. 5.1 d and 5.2 d are associated with another more vigorous disturbance which is just visible on the eastern boundary of Fig. 5.1 a.

Initial conditions for this case are similar in some respects to the FGGE Type I storm described in Chapter III. Strong baroclinity and a location near the right exit region of an advancing upper-level jet are evident at the genesis stage of the vigorously developing FGGE case (Fig. 3.5 a) and the non-developing case described here. However, the subsequent evolution of the disturbance in Fig. 5.1 differs markedly from both the FGGE and the NOGAPS Type I cases in Chapter III. It is the objective of this section to determine why this disturbance failed to intensify.
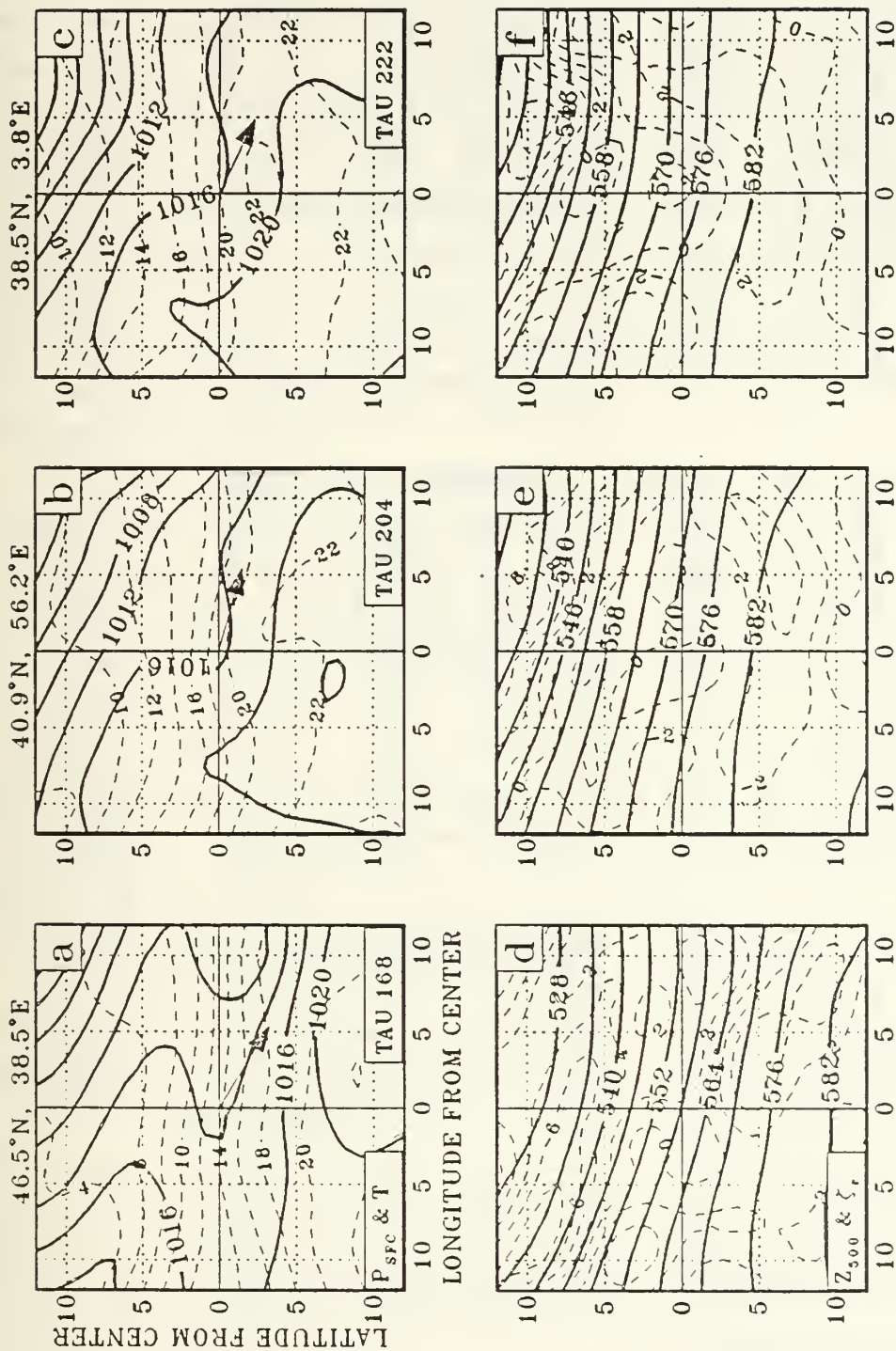
136

Fig. 5.1. (a-c) Surface pressure (mb, solid) and temperature (°C, dashed); and (d-f) 500 mb heights (dam, solid) and relative vorticity (10^{-5} s^{-1}, dashed) for non-developing NOGAPS Type I.

137
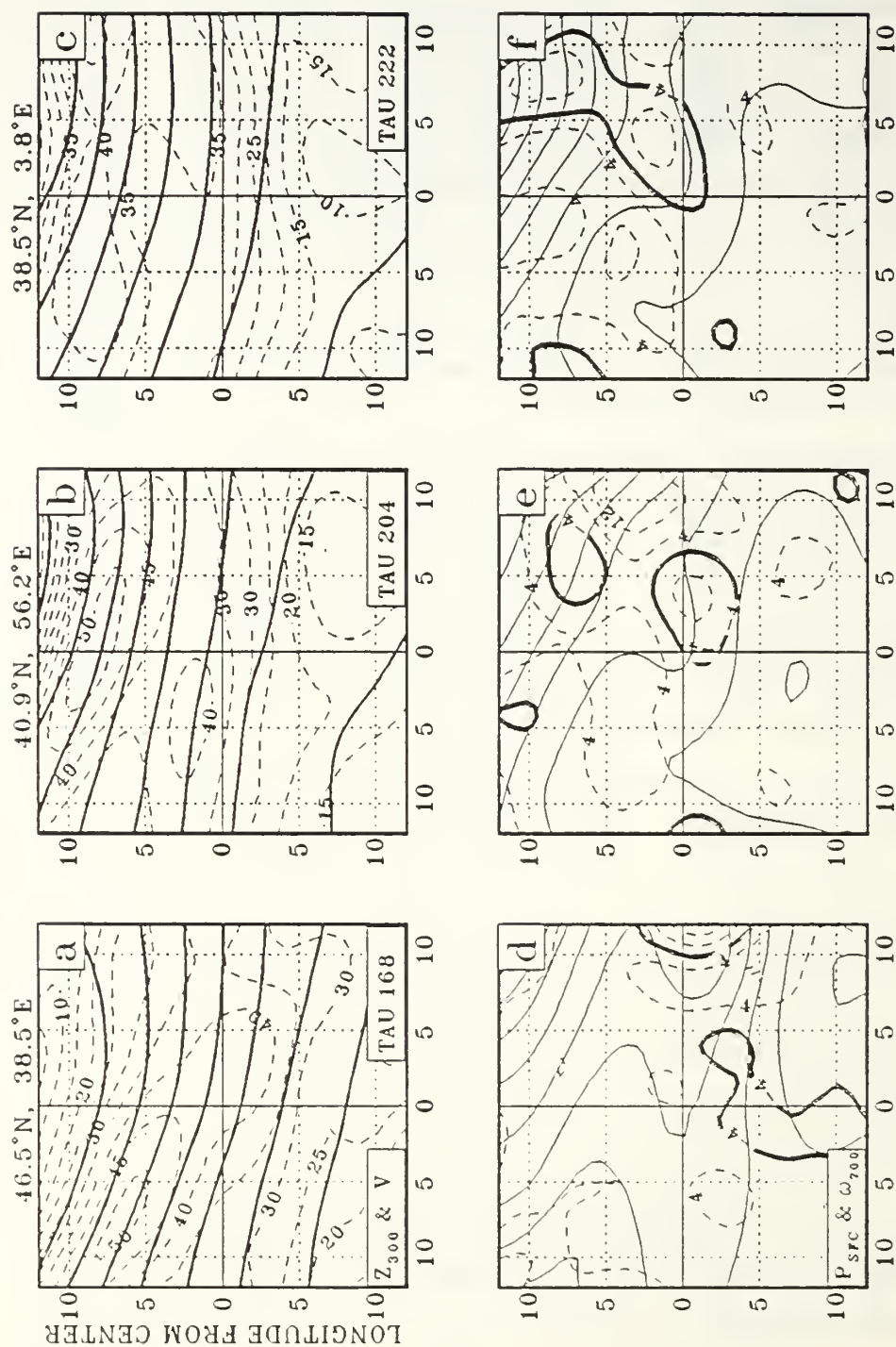
Fig. 5.2. (a-c) 300 mb heights (contours every 120 dam, solid) and wind speed (ms^{-1}, dashed); and (d-f) surface pressure (contours every 4 mb, solid) and 700 mb vertical p-velocity (mb h^{-1}, dashed) for non-developing NOGAPS Type T. Format as in Fig. 5.1.

2.   Vorticity and Heat Budget Analysis

To gain insight into factors which hinder development of the Type I disturbance described in this section, the results of the quasi-Lagrangian budget analysis of this case will be compared with the more vigorous Type I storms analyzed in Chapter III. Since reliable estimates of budget terms are obtained from the model-generated fields, discrimination between developing and non-developing disturbances should be possible. Since the FGGE data budgets presented earlier were not closed to an acceptably small uncertainty, the analysis of non-developing cases will be confined to the NOGAPS simulations.

The vorticity budget analysis for this non-developing Type I disturbance shows a deep layer of decreasing vorticity (Fig. 5.3 a). Near 300 mb, this is due to strong NVA, while a weaker divergence sink is evident at mid-levels (Fig. 5.3 d). Near the surface, generation by convergence is more than offset by the effects of friction (negative residual in Fig. 5.3 a) and eddy transport losses. The initial surface convergence in Fig. 5.3 d is only a fraction of that in Fig. 3.10 d for the developing case. This weak low-level inflow is consistent with the feeble vertical mass circulation (see Fig. 5.2 d-f).

The strong NVA aloft at early stages of this non-developing case has no counterpart in the developing storms. Weak PVA is evident at early stages of both developing Type I storms (see Figs. 3.10 d and 3.13 d). The similarity of the time series of quasi-Lagrangian vorticity tendency and vorticity advection aloft (Fig. 5.4) suggests that vorticity changes are primarily the result of advection. This indicates a lack of in-situ vorticity generation. Thus, vorticity changes aloft occur as the budget volume migrates to an area of different upper-level vorticity. This

139
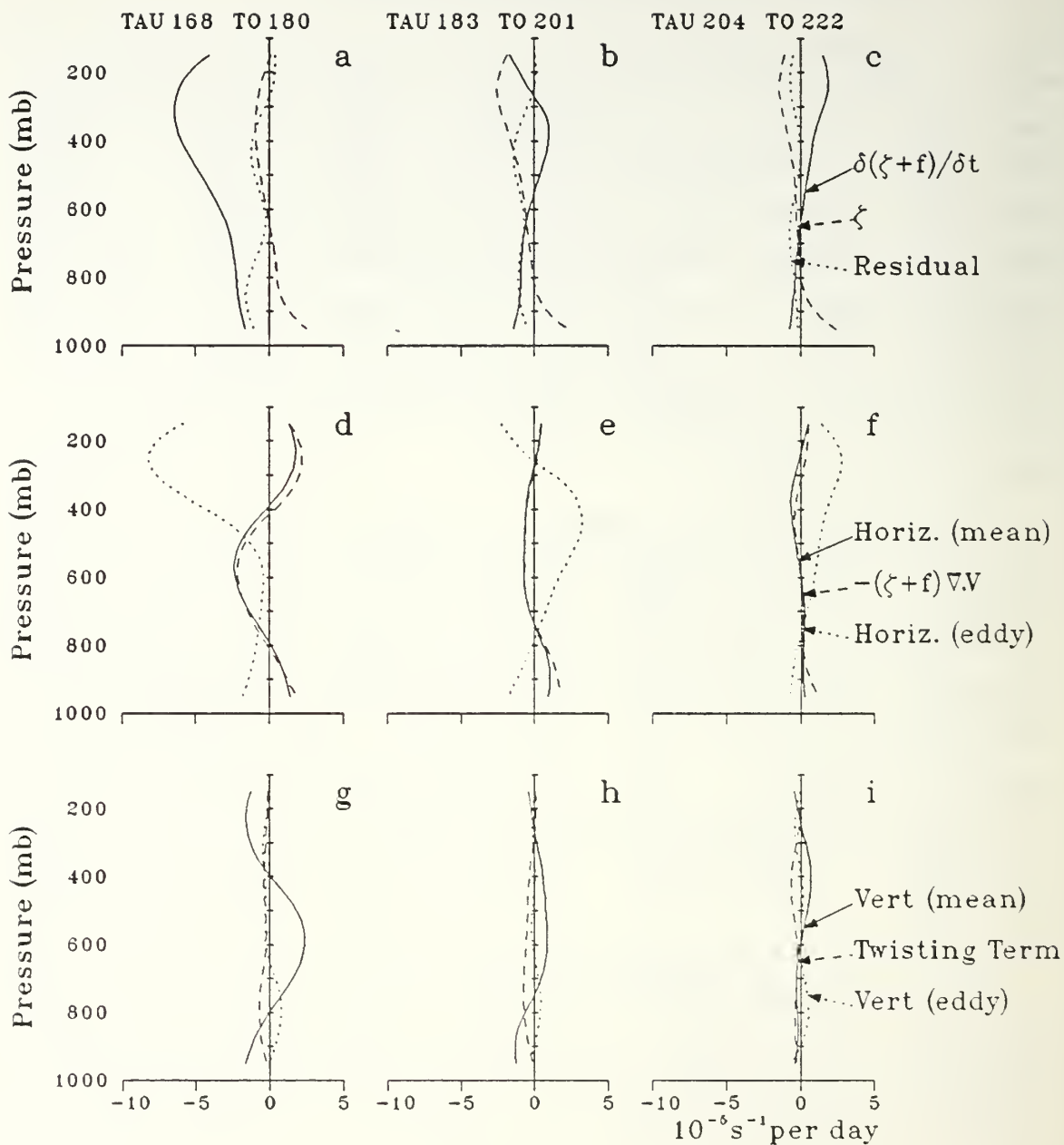
Fig. 5.3.   Vorticity budget terms for 5° latitude radius
volume for non-developing NOGAPS Type I. Budget
terms are indicated in the legend on the right.

140

suggests a lack of coupling between the surface disturbance
(which is used to locate the budget volume) and upper-level
features. Vertical coupling occurs via the secondary mass
circulation when changes in the upper-level vorticity struc-
ture (increasing PVA aloft) occur in conjunction with
changes (increases) in the strength of the vertical mass
circulation. The juxtaposition of lower and upper features
in this case is unfavorable for such coupling. The continued
location of the surface disturbance beneath the upper-level
convergence quadrant of the primary 300 mb jet is not condu-
cive to vigorous mass circulation increases, such as
occurred in the developing cases.
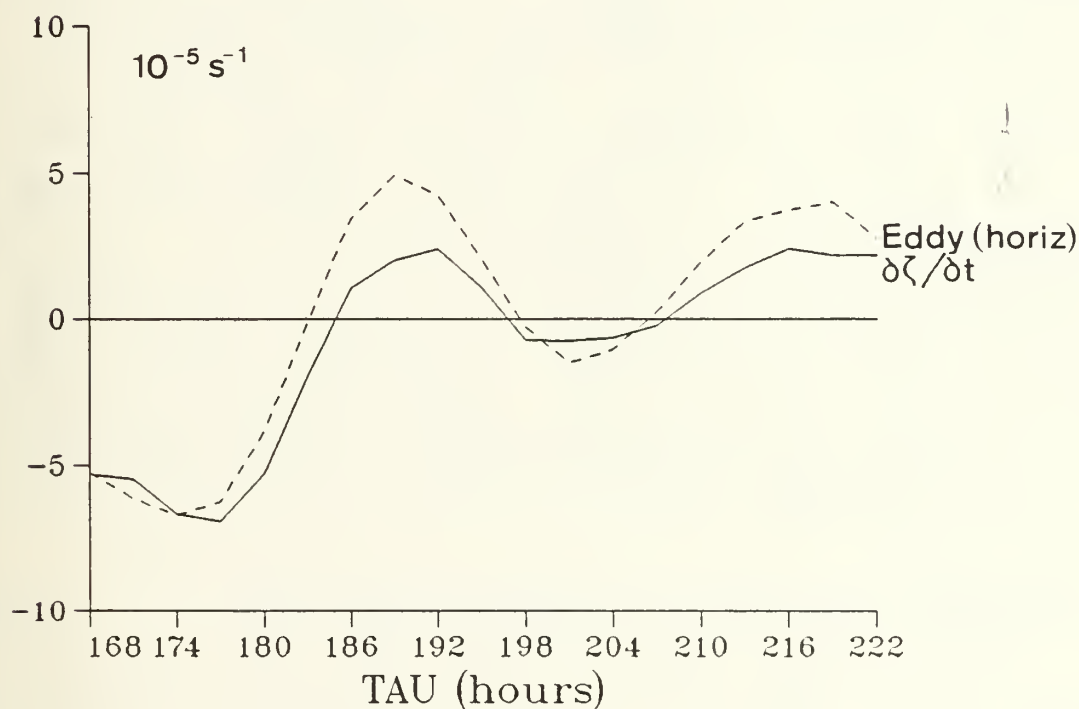
Fig. 5.4.   Time series of quasi-Lagrangian vorticity tend-
ency (solid) and horizontal eddy flux (dashed)
averaged between 200 mb and 500 mb for NOGAPS
non-developing Type I.

141

The FGGE storm also formed beneath the upper-level
convergence (Fig. 3.14 d) associated with the equatorward
exit region of the jet streak aloft (Fig. 3.6 a). However,
strong vertical coupling in that case was established as the
jet streak rapidly migrated to a position southwest of the
surface disturbance (Fig. 3.6 b). The vigorous mass circu-
lation increases (Fig. 3.8) coincided with the incursion of
the divergent exit region of the jet into the budget volume
(Cook, 1983). The presence of a downstream ridge (Fig. 3.4
d) contributed to rapid growth of PVA. In the non-
developing case, the jet remains well to the north (Fig. 5.2
a-c) and the vertical mass circulation remains weak (Fig.
5.2 d-f). The maintenance of cyclonic vorticity aloft to the
east appears to inhibit the development of PVA.

The heat budget shows large temperature increases
throughout the troposphere (Fig. 5.5 a,b) that are almost
entirely due to the horizontal eddy transport term (thermal
advection) in Fig. 5.5 g,h. Budget terms associated with
the vertical mass circulation (diabatic heating and adia-
batic cooling) in Fig. 5.5 d-f are small. This is consistent
with the lack of thermal wave amplification in Fig. 5.1 a-c.
Thus, warming is primarily the result of the southeast move-
ment of the surface disturbance to a warmer location (see
Fig. 5.1 a). By contrast, the leading terms in the heat
budget for the developing Type I NOGAPS polar low (Fig.
3.15) are diabatic heating and adiabatic cooling. This indi-
cates that temperature changes are not entirely due to
advective effects, which is consistent with the amplifica-
tion of thermal features in that case (Fig. 3.3).

The heat budget residual (Fig. 5.5 a-c) is remark-
ably small at all stages of this non-developing disturbance.
This attests to the accuracy of the numerical schemes used
to compute the leading terms of horizontal eddy flux (which
includes the budget volume translation velocity) and
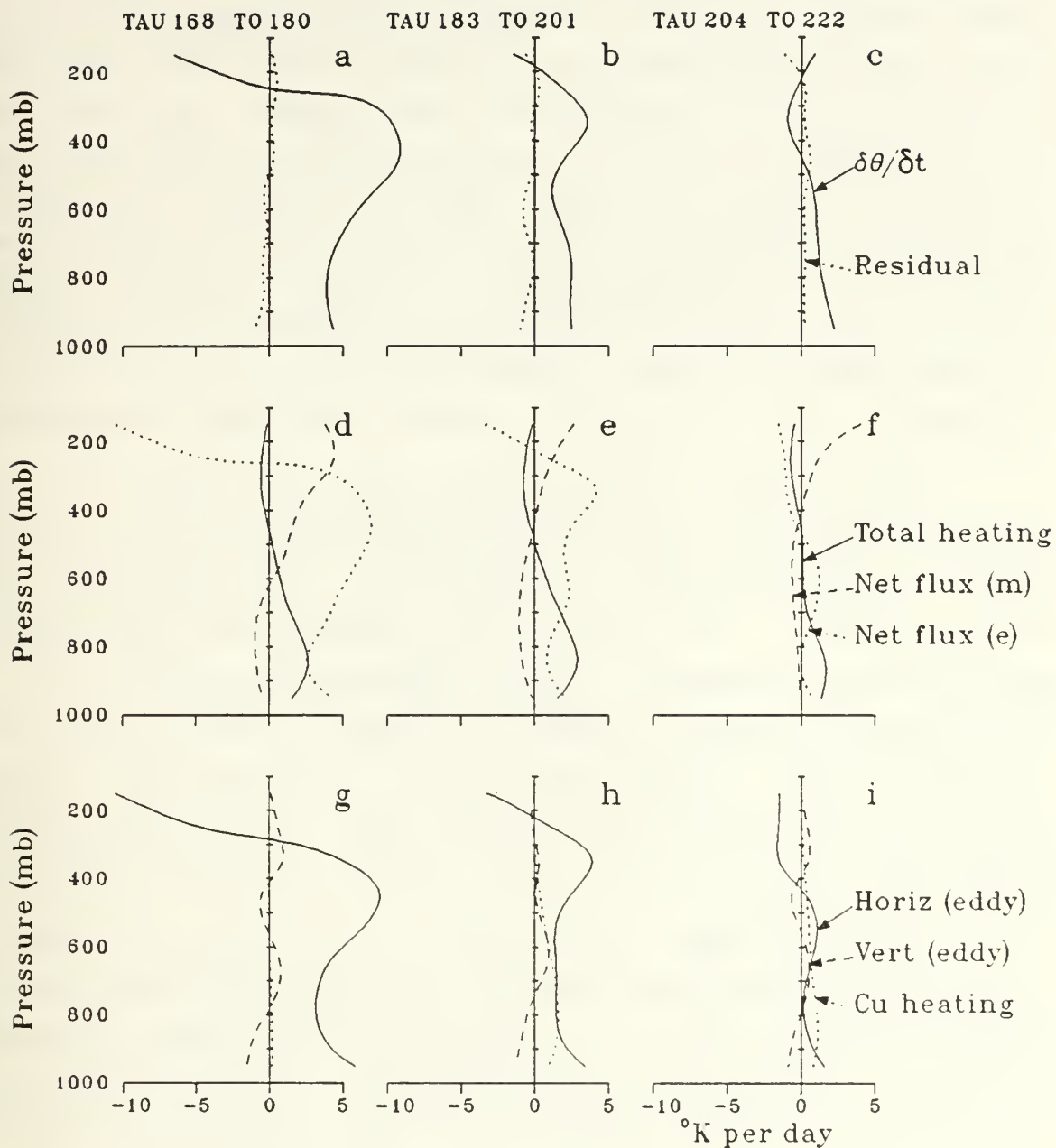
Fig. 5.5.   Heat budget terms for non-developing NOGAPS Type
I. Format as in Fig. 5.3.

143

quasi-Lagrangian potential temperature tendency. The much larger residual for the developing case (Fig. 3.15 a-c) arises from uncertainty introduced during the vertical interpolation of temperatures from sigma to pressure surfaces. This residual is correlated with the net mean flux convergence (Fig. 3.15 d-f). Since this term is the small difference between the horizontal and vertical mean flux terms (which separately amount to several hundred degrees per day), this temperature error is magnified considerably. In comparison, the mean mass circulation for the non-developing case is small, which results in smaller uncertainty.

These budget analyses indicate that vorticity and thermal changes are largely the result of translation of the budget volume relative to features of the vorticity and thermal fields. The budget terms responsible for in-situ geopotential and thermal wave amplification are comparatively small and are confined to lower levels. This is consistent with the weak development of the upper trough (Fig. 5.1 e,f). The analysis shows that this non-developing disturbance is shallow and only weakly coupled to the flow aloft.

The thickness tendency fields for this case (Fig. 5.6) are quite different from those of the developing cases (Figs. 3.16 and 3.24). In the developing cases, thermal advection contributes warming (cooling) ahead of (behind) the developing wave. As the low-level circulation becomes more intense, the amplitude of this dipole increases. Because adiabatic cooling and diabatic heating tend to balance to a high degree, net thickness changes in the developing cases occur which are approximately in phase with the advective contributions. Such changes are associated with geopotential increases (decreases) in the upper ridge (trough) which indicate self-amplification of the upper

144

wave. Thus, lower and upper-level features are strongly coupled in the developing cases. In contrast, the thermal advection patterns for the non-developing case (Fig. 5.6 a-c) have no strong dipole structure. Rather, a general warming trend at the initial time (Fig. 5.6 j) results from translation of the disturbance toward a warmer environment. The adiabatic cooling (Fig. 5.6 d) and diabatic heating (Fig. 5.6 g) are small, in accordance with the heat budget (Fig. 5.5 d). This is consistent with the weak secondary mass circulation (Fig. 5.2 d-f). The resulting surface convergence does not produce the low-level circulation increases required for a strong thermal advection dipole. Only at 204 h is there any hint of a self-amplification pattern (Fig. 5.6 k). However, the dipole amplitude is less than 100 gpm per day and the resulting amplification of the upper wave is slight (Fig. 5.1 e,f).

This analysis suggests that a characteristic of the developing polar low which is absent for the non-developing case is the diagnosis of self-development, which is indicated by patterns of net warming (cooling) ahead of (behind) the low center throughout a deep layer. Self-development indicates a cooperative interaction between the growing surface circulation and the amplifying upper-level features. In the non-developing case, thickness changes which indicate self-development are not present. This is consistent with the weak vertical mass circulation and indicates a lack of vertical coupling in the non-developing case.

Self-development is a manifestation of baroclinic development, and is favored in regions of low static stability, enhanced baroclinity and high relative humidity. Therefore, a key to understanding differences between developing and non-developing disturbances may lie in diagnosing these conditions. In consideration of these three criteria, an attempt was made to discriminate between developing and non-developing disturbances at early stages of formation.
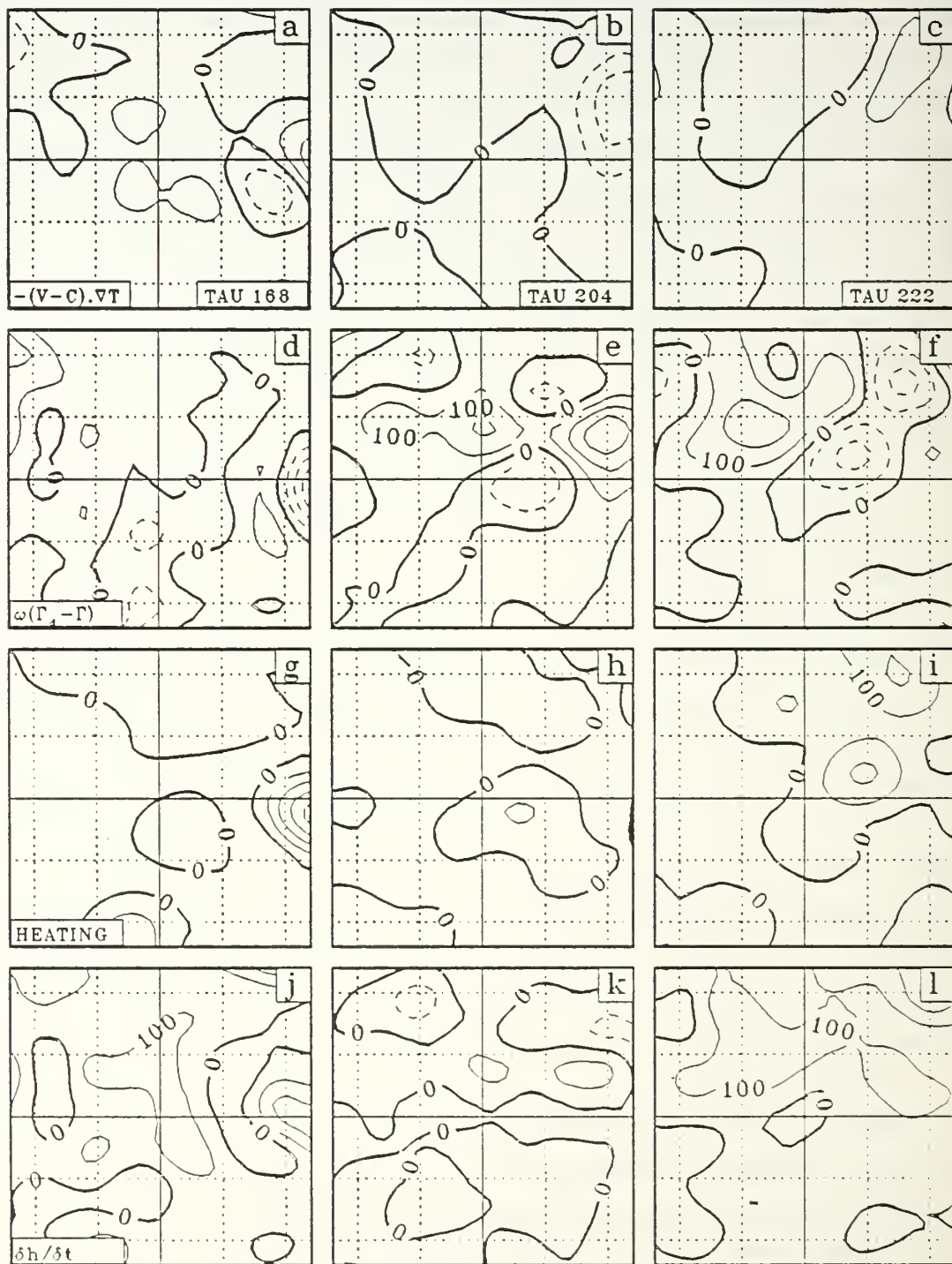
Fig. 5.6.   Thickness tendency equation terms (m day^{-1})
for non-developing NOGAPS Type I. (a-c) Hori-
zontal thermal advection; (d-f) vertical advec-
tion; (g-i) diabatic heating; (j-l) quasi-
Lagrangian thickness tendency.

146

At the incipient stage, the static stability index for the developing NOGAPS Type I case was 4.7°K per 100 mb, which is close to the moist adiabatic value appropriate to the surface air temperature. For the non-developing disturbance, the index increased from 4.5 to 5.2°K per 100 mb during the first 12 h. The moist adiabatic rate for the same period increased from 4.6°K to 5.2°K per 100 mb as a result of the increasing surface temperature. Thus, there is little difference between the static stabilities of the developing and the non-developing cases. In both cases, the stability is close to the saturated adiabatic value.

Another consideration is the initial baroclinity in the region of the two disturbances. A surface temperature difference of 14°C occurs between points 5° lat. to the north and 5° to the south of the non-developing disturbance center (Fig. 5.1 a). For the developing case (Fig. 3.3 a), this difference is 12°C. Another measure of the baroclinity is the vertical wind shear. The wind speed increases from less than 5 m s^{-1} at the surface to nearly 50 m s^{-1} at 300 mb for the non-developing case. The corresponding upper-level wind maximum for the developing polar low is only 35 m s^{-1} (Fig. 3.2 a). Thus, the baroclinity of the non-developing disturbance is slightly stronger than for the developing case.

Another important property of the initial state is the ambient relative humidity. The largest latent heat release in ascent regions of extratropical cyclones would be expected to occur when the low-level air is nearly saturated. At the initial times, the relative humidity in the vicinity of the non-developing case (Fig. 5.7 d) is around 85% compared with 80% for the developing storm (Fig. 5.7 a). At later stages, the relative humidity of the developing storm approaches about 90% (Fig. 5.7 b) while that for the non-developing case decreases (Fig. 5.7 e). This difference

is because significant precipitation (not shown) occurs with the developing storm whereas none occurs with the non-developing case. Thus, the near-saturation in Fig. 5.7 b is the result of the condensation occurring in the ascending air.

This analysis appears to suggest that the initial conditions for the non-developing case were also favorable for baroclinic development, as in the developing case. That is, large baroclinity, high humidity, and low static stability were present at the initial stages of the Type I non-developing polar low. This suggests that other factors are involved in the development of the Type I polar low. The location of the non-developing polar low beneath the convergence quadrant of the upper-level jet appears to inhibit the growth of the vertical mass circulation. This is consistent with the lack of coupling between upper and lower features discussed earlier.

B. NON-DEVELOPING TYPE II DISTURBANCE

1. Synoptic Description

The storm described here is a slowly decaying surface vorticity maximum (Fig. 5.8 a-c) that is embedded within a strong northerly flow on the western periphery of a deep cyclone. This case has many of the characteristics of the Type II lows described above, and is quite similar to observed polar lows that form as cyclonic vorticity lobes on the poleward side of the parent low. The vorticity center in this case had earlier been the primary surface low center, but it had decayed as a new, more vigorous low developed to the southeast. It is of interest that this new low was the mature stage of the Type II storm described earlier (compare Figs. 4.1 c and 5.8 a). Polar lows occasionally develop from the old vorticity centers associated with decaying

148
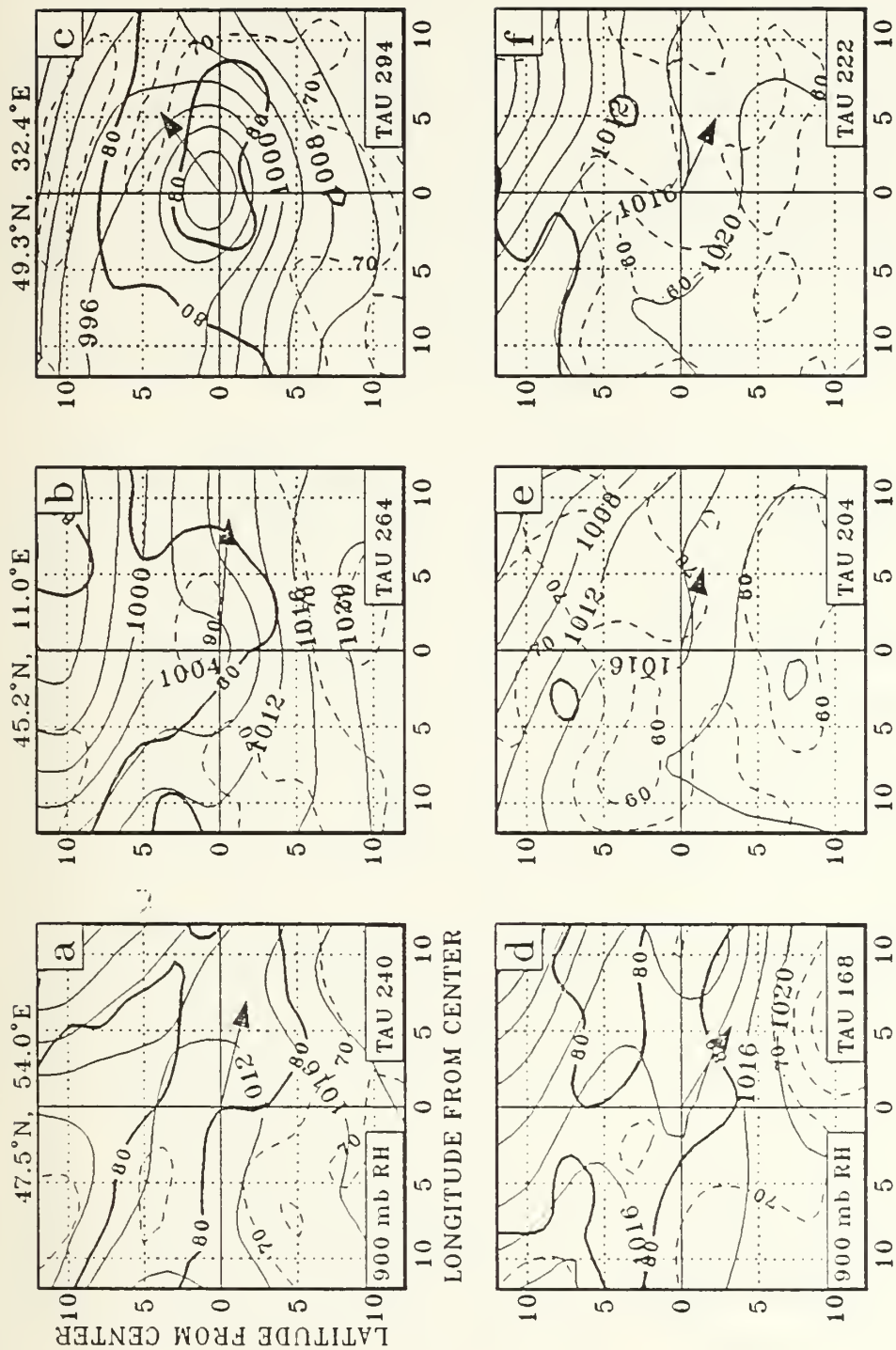
Fig. 5.7. (a-c) Surface pressure (contours every 4 mb, solid) and relative humidity (%, dashed, except 80% isopleth highlighted for clarity) for developing NOGAPS Type I. (d-f) As in (a-c) except for non-developing NOGAPS Type I.

149

occluded systems.   Given the rather similar location and
initial conditions as for the developing Type II case, the
purpose of this section is to determine why this center did
not develop while it was in the polar air stream.

The non-developing vorticity center migrates cyclon-
ically about the parent low and is eventually absorbed into
the mean flow (Fig. 5.8 c).   At the start of this case,
surface vorticity values in excess of 8×10^{-5} s^{-1} are
present, with surface winds up to 20 m/s near the center.
The surface vorticity center is located beneath a broad 500
mb trough (Fig. 5.8 d). A fast-moving short-wave trough and
an associated 300 mb wind speed maximum (Fig. 5.9 a) are
located about 700 km to the west of the surface center.
After 24 h, the upper-level vorticity maximum has moved to a
position southeast of the surface center (Fig. 5.8 e). This
upper-level short-wave trough appears to be coupled with a
rapidly developing surface trough that forms 1000 km south
of the center (Fig.   5.8 a) and translates cyclonically
around the parent low ahead of the decaying center described
here.   This trough to the south is thus another example of a
developing Type II polar low which forms in response to PVA
aloft.   Although the northern (dissipating) vorticity center
lies poleward of the 300 mb jet (Fig. 5.9 a-c), a favorable
coupling with a mid-tropospheric PVA center does not occur.
Some upper-level support is initially present, as a center
of upward vertical motion (Fig. 5.9 d) is located over the
surface center. However, this vertical motion weakens with
time (Fig. 5.9 e,f).

Very little baroclinity is associated with the weak-
ening disturbance (Fig.   5.10).   In contrast, the horizontal
temperature gradients associated with both the developing
Type II disturbances (Figs. 4.3 and 3.3) are larger, espe-
cially at early stages.   The enhanced baroclinity to the
south in Fig.   5.10 a is associated with the developing

150
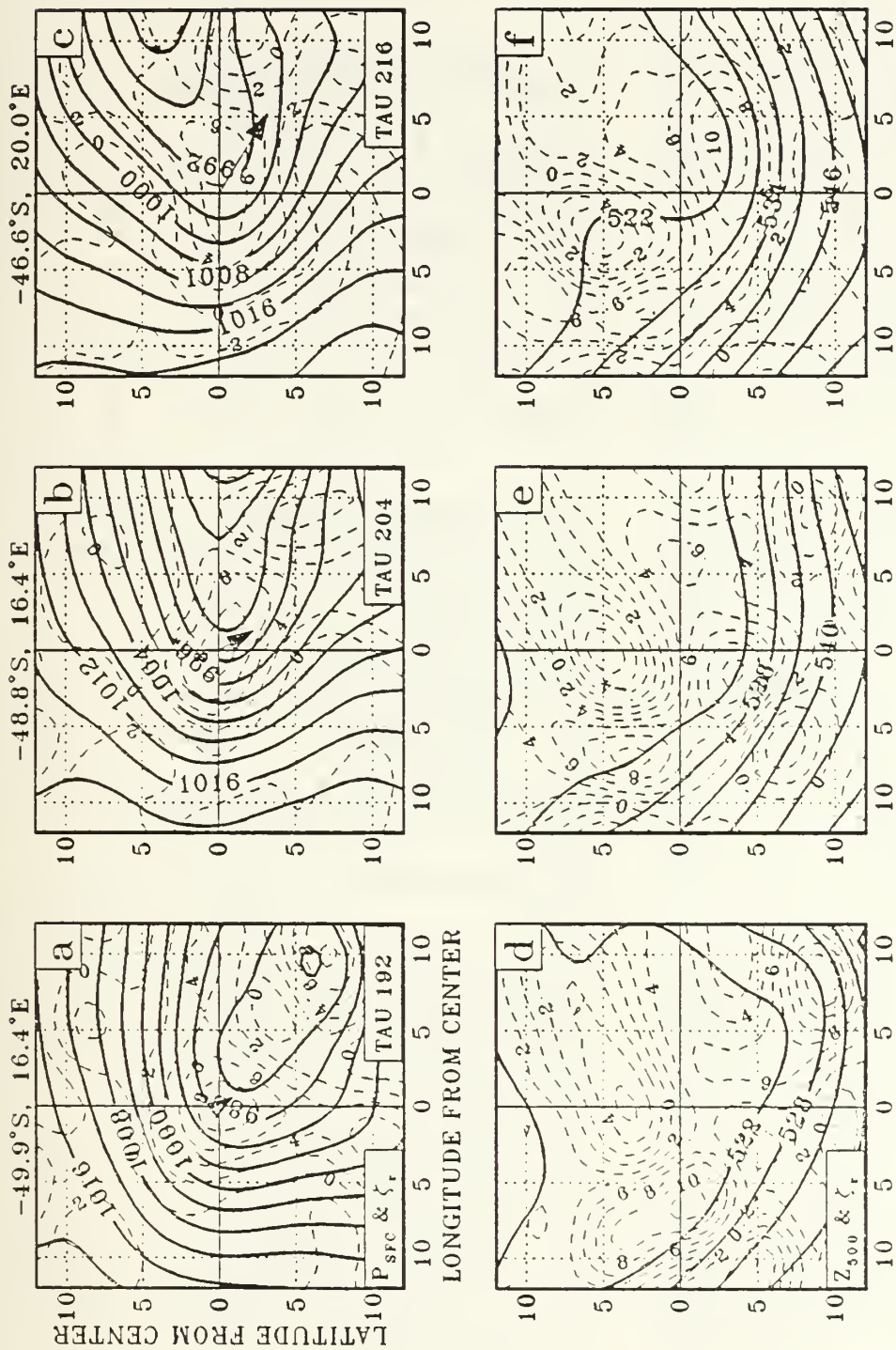
Fig. 5.8. (a-c) Surface pressure (mb, solid)- and relative vorticity (10^{-5} s^{-1}, dashed); and (d-f) 500 mb heights (dam, solid) and relative vorticity (10^{-5} s^{-1}, dashed) for non-developing NOGAPS Type II.
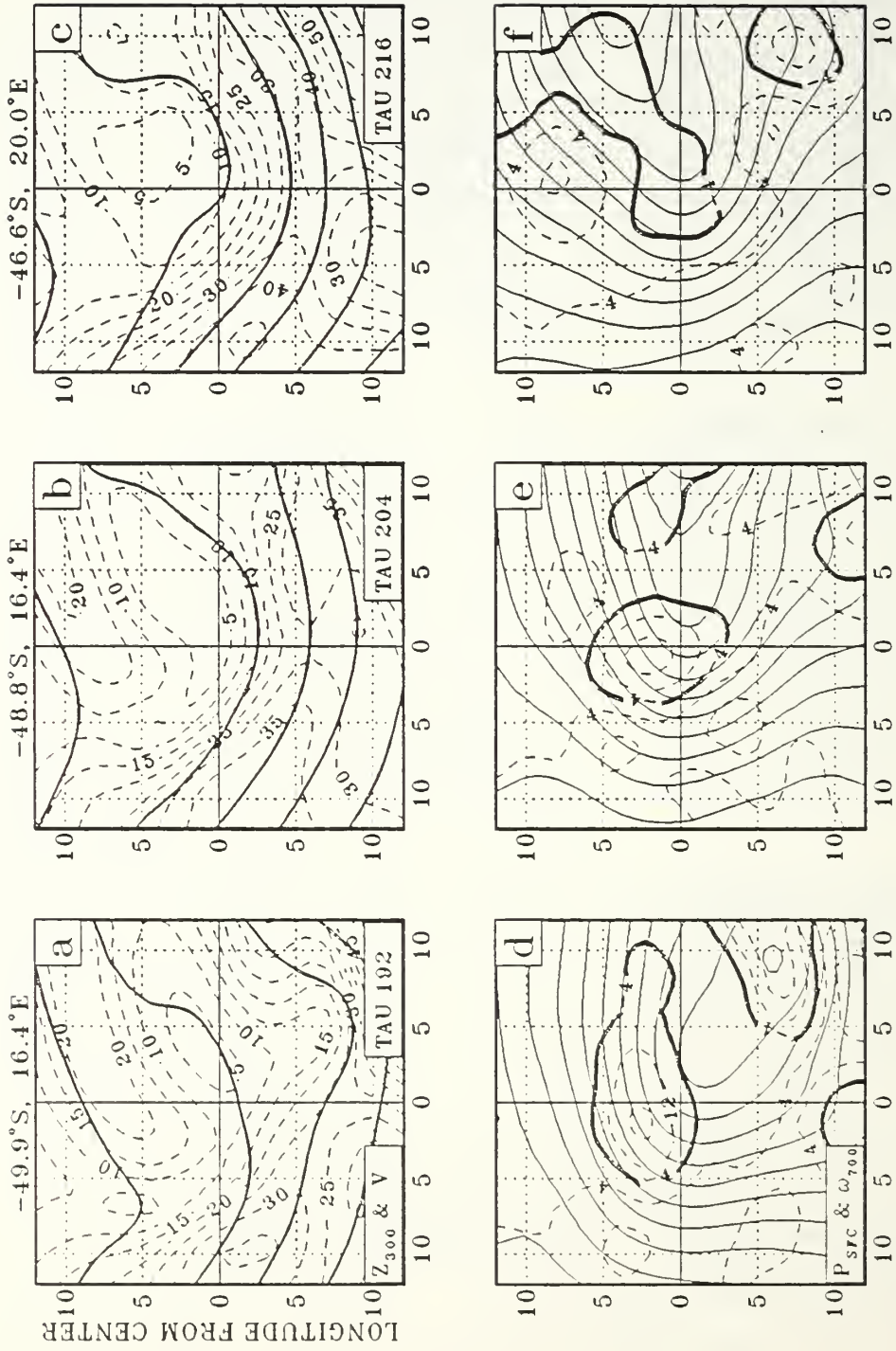
Fig. 5.9. As in Fig. 5.2 except for non-developing NOGAPS Type II.

disturbance there. The surface center at the initial time is located in the thermal ridge ahead of a thermal trough (Fig. 5.10 a,d). Thus, the thermal patterns at the early stages of this non-developing disturbance are similar to those at the final stages of both Type I and Type II developments (Figs. 3.3 c,f, 4.3 c,f, 3.6 c,f and 4.5 c,f). This is consistent with the previous history of this non-developing disturbance as an occluded primary low center.

Another indication of the baroclinity is the vertical wind shear. The 300 mb wind speed directly above the initial surface vorticity center is less than 10 ms^{-1} (Fig. 5.9 a-c). The wind speed maximum in the jet does not exceed 40 ms^{-1}. By contrast, wind speed maxima in the upper troposphere exceeded 55 ms^{-1} above both the developing Type II disturbances (Figs. 4.2 a-c and 4.6 a-c).

The surface circulation of this decaying storm is initially large. However, the lack of favorable coupling with the upper-level jet and weak baroclinity appear to inhibit further development of this disturbance.

2. Quasi-Lagrangian Budget Analysis

The quasi-Lagrangian budgets of mass, vorticity and potential temperature were calculated to determine the physical processes that led to decay of this system. Although the horizontal analyses depict fields to 240 h, the quasi-Lagrangian analyses extend only to 216 h. After 216 h, a maximum of surface vorticity is no longer available to position the budget volume.

The mass budget illustrates a layer of slowly decreasing convergence (Fig. 5.11 a) beneath a weakening outflow above about 700 mb. The deep layer of convergence at the initial time reflects this disturbance's previous history as a major circulation center. The weakening vertical velocity (Fig. 5.11 b) and the decreasing elevation
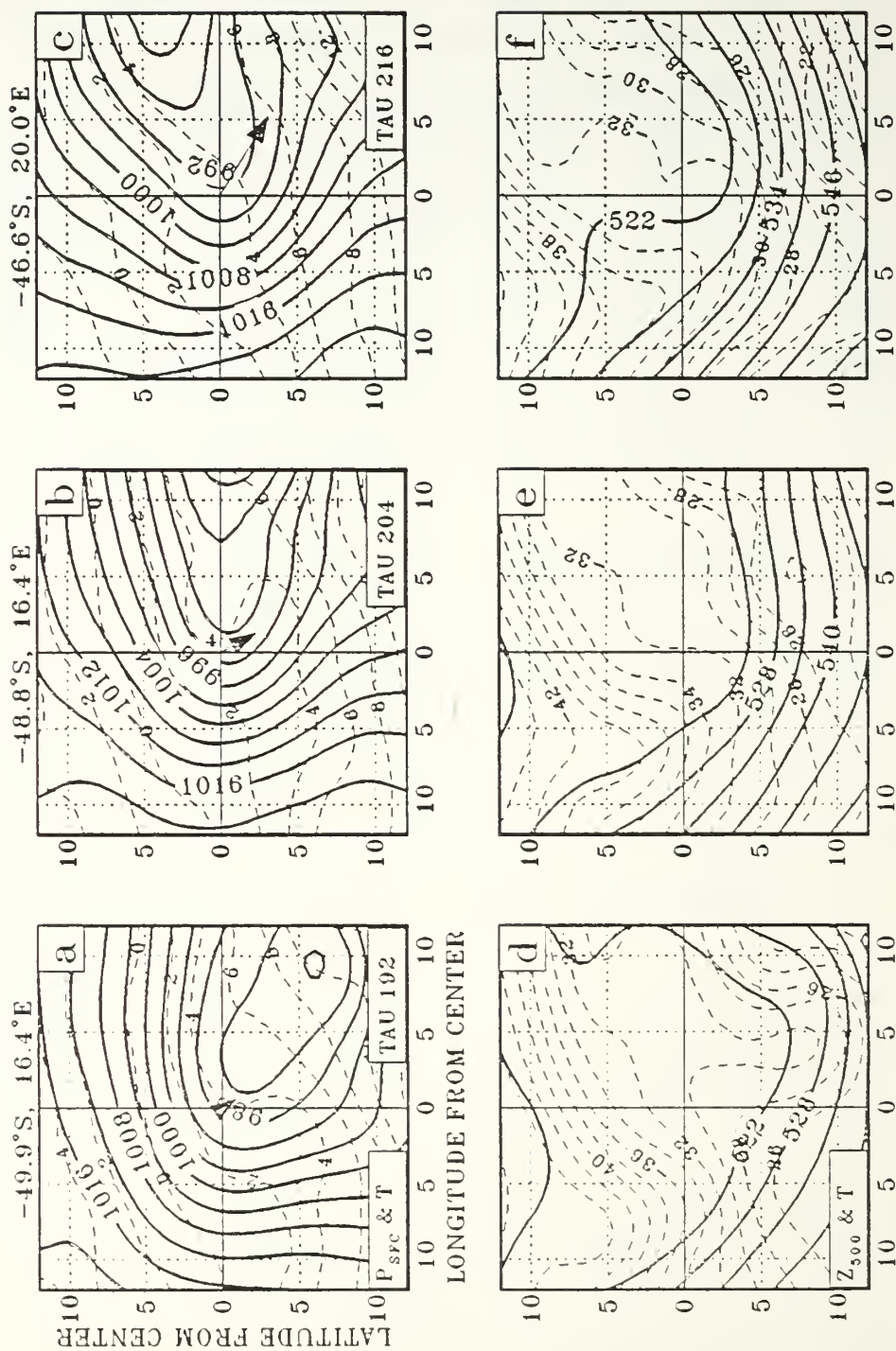
Fig. 5.10. (a–c) Surface pressure (mb, solid) and temperature (°C, dashed); and (d–f) 500 mb heights (dam, solid) and temperature (°C, dashed) for non-developing NOGAPS Type II.

154

of the LND reflects the dissipating nature of this distur-
bance and is consistent with the significant but weakening
upward motion in Fig. 5.9 d-f. Positive values of omega at
the surface are consistent with increasing surface pressure
that is associated with the vorticity center. In contrast,
the developing cases exhibit a rapidly growing mass circula-
tion which sustains a deepening and strengthening convergent
layer (Figs. 4.7 and 4.11) and spinup of vorticity. In the
developing cases, the increasing ascent is coupled with
increasing PVA aloft near the poleward exit region of a
significant upper-level jet. Such coupling does not occur
in the non-developing case since the area of largest PVA
aloft is coupled to the developing disturbance to the south.

The vorticity budget is presented in Fig. 5.12. The
strong, pre-existing vertical mass circulation tends to
maintain a large, but slowly decreasing, convergence source
term (Fig. 5.12 c,d) near the surface. This low-level
vorticity source is opposed by large frictional dissipation,
which is implied by the large negative budget residual (Fig.
5.12 a,b). The friction is large because of the combination
of high surface winds and large positive vorticity. Even
though the existing low-level convergence tends to sustain
the vortex, the low-level vorticity decreases slowly (Fig.
5.12 a,b). In comparison, the convergence source for the
developing Type II case increases rapidly (Fig. 4.9 d-f) and
surface friction becomes large only at later stages of
development (Fig. 4.9 d-f).

Increasing vorticity aloft (Fig. 5.12 a) is the
result of PVA which is partially offset by divergence (Fig.
5.12 c,d). The PVA is initially larger than that which
accompanies the formation of the developing Type II storm
(Fig. 4.9 d). This large PVA would seem to be favorable for
low-level cyclogenesis. However, an examination of Fig. 5.8
d-f indicates that this large PVA is actually associated

LATERAL MASS FLUX CONVERGENCE
(9.89 x 10^{14}kg per day)
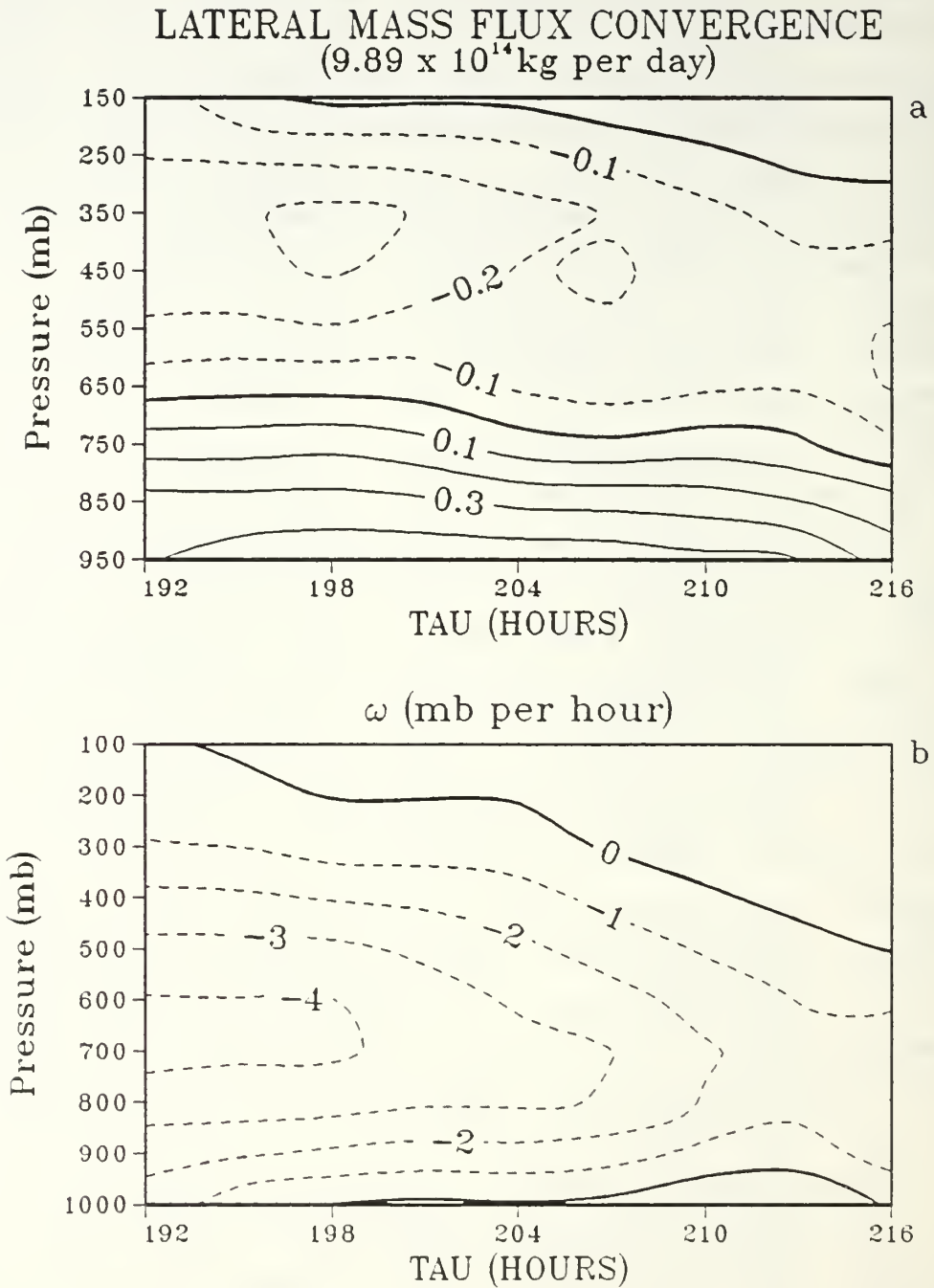
Fig. 5.11. (a) Time evolution of lateral mass flux con-
vergence for non-developing NOGAPS Type II.
Positive (solid) values indicate inflow. (b)
Area-averaged vertical p-velocity (mb h^{-1}).
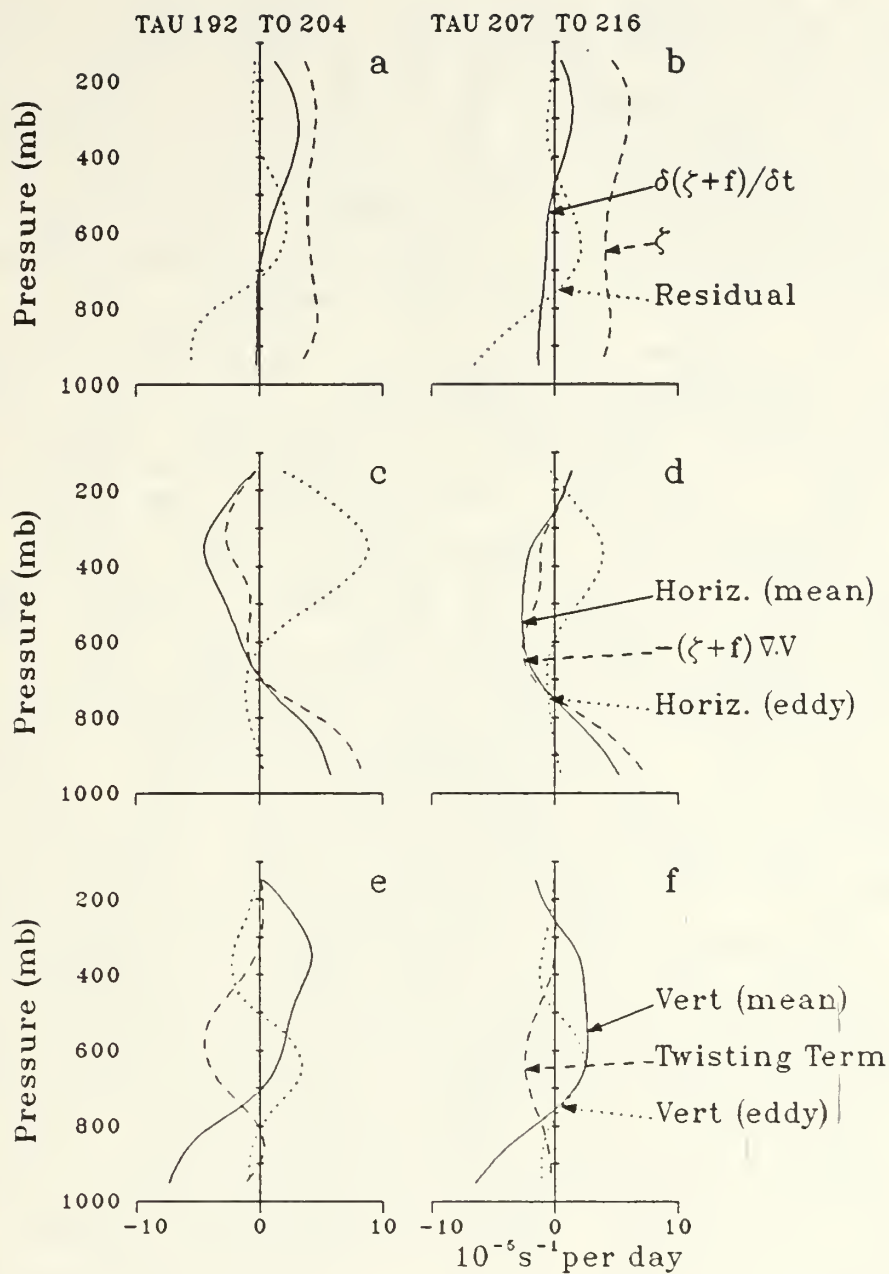
Fig. 5.12. As in Fig. 5.3 except for non-developing NOGAPS Type II.

with the migrating short-wave trough that is strongly coupled with the developing disturbance to the south. In fact NVA occurs directly above the non-developing center. Thus, the seemingly favorable features of cyclogenesis and PVA aloft in the vorticity budget are associated with the developing system to the south that is also incorporated into the 5° latitude radius budget volume.

The leading terms in the heat budget are diabatic heating and adiabatic cooling (Fig. 5.13 c,d). These terms are about half those from the developing NOGAPS Type II storm (Fig. 4.14 d-f), which reflects the larger vertical mass circulation for the developing case. Model cumulus heating (Fig. 5.13 e,f) is negligible for this case. This may indicate a model deficiency, since in cold polar outbreaks similar to Fig. 5.8 a,b, cumulus convection is common. It may be that the type of convective overturning that occurs in nature also occurs here, but because it is confined to the lowest model layer it is labelled in NOGAPS as large-scale precipitation (e.g., Bosse, 1984). The hori- zontal eddy term (thermal advection) is initially negative (Fig. 5.13 e). This is consistent with the cold advection to the south of the disturbance at low levels (Fig. 5.10 a) and the cold advection aloft that is associated with the short- wave to the west of the surface center (Fig. 5.10 d). At later stages, the horizontal eddy term is smaller (Fig. 5.13 f) due to the more rapid southeastward movement of the disturbance (see Fig. 5.8 a,b). Another difference between the heat budgets at early and later stages of this distur- bance is the decrease in the net mean flux convergence (compare Figs. 5.13 c,d). This decrease arises from the increasing contribution from subsidence warming to the south of the disturbance center (Fig. 5.9 e) which is partially included in the budget volume. This subsidence is associ- ated with the developing disturbance to the south. Thus, the

change from net cooling (Fig. 5.13 a) to warming (Fig. 5.13 b) is due to increases in both the horizontal eddy and the net mean heat flux terms. As was the case with the vorticity budget, features associated with the developing storm are incorporated into the budget volume. This suggests that a smaller budget volume is required to better resolve the physical processes that are associated only with the dissipating vorticity center.

The time section of diabatic heating (Fig. 5.14 a) shows an initial increase in heating followed by a diminishing layer of heating which is strongest near the surface. Large surface fluxes that result from strong northerly flow over warmer water account for near-surface heating rates of around 4°C per day. For the developing Type II disturbances, it was hypothesized that large surface heating combined with cooling aloft could enhance development of the upper trough. In this dissipating case, the upper-level trough is not coupled with the surface vorticity center, so such a cooperation between the surface heating and the amplifying upper-level trough cannot apply.

The pattern of baroclinic conversion (Fig. 5.14 b) is rather surprising in that the maximum conversion does not occur until 204 h. A small positive conversion would be expected for the dissipating disturbance from the correlation of ascent (Fig. 5.9 d) with the thermal ridge (Fig. 5.10 a,c). The magnitude of both the thermal wave and the vertical circulation decrease at later stages seem to indicate reduced conversion. Thus, the increasing conversion in Fig. 5.14 b during the first 12 h is probably due to the incorporation of the subsidence (Fig. 5.9 e) which occurs within the amplifying cold trough (Fig. 5.10 b,e) to the south. This is coupled with the developing southerly system. Thus, the large baroclinic conversion in Fig. 5.14 b is due to the large budget volume that includes more than just the circulation of the non-developing disturbance.
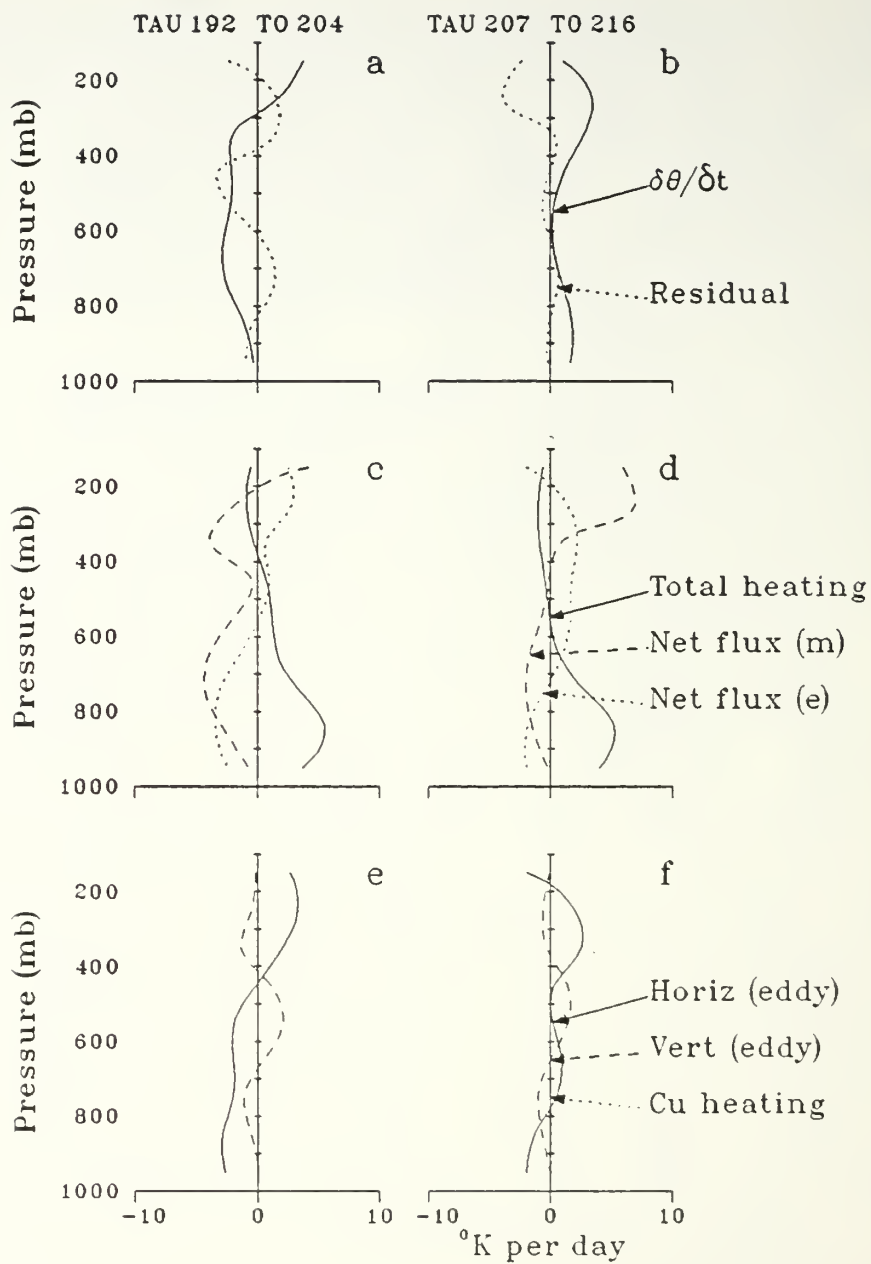
Fig. 5.13.   As in Fig. 5.5 except for non-developing NOGAPS
             Type II.

160

DIABATIC HEATING (°C per day)

a

ω α

b
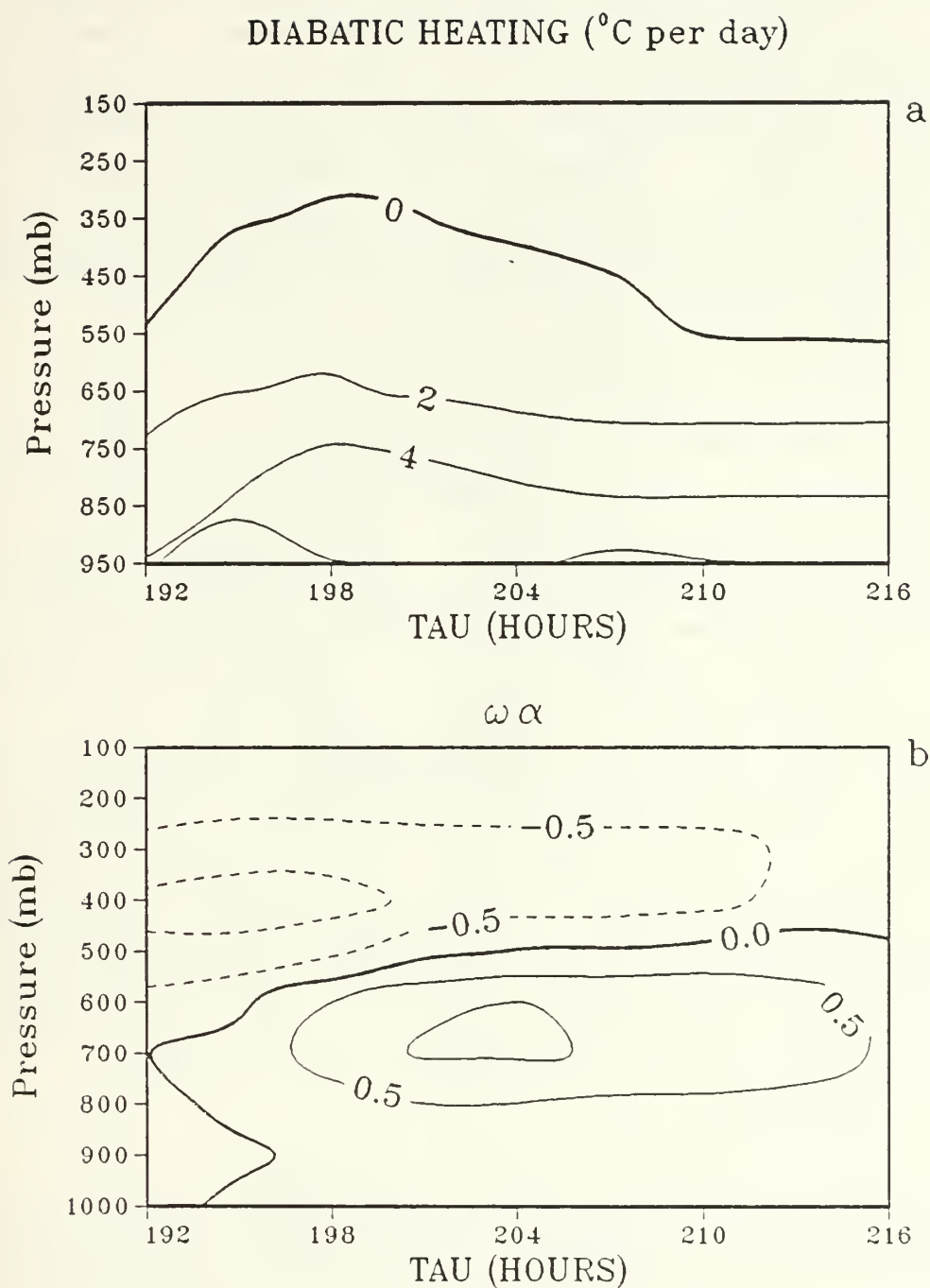
Fig. 5.14.   (a) Time evolution of diabatic heating (°C per day) and (b) baroclinic conversion (mW kg^{-1}) for non-developing NOGAPS Type II.

161

The horizontal distributions of terms in the thickness tendency equation are shown in Fig. 5.15, so that the contributions from the two systems can be separated. The thermal advection dipole (Fig. 5.15 a-c) associated with the dissipating vorticity center is weak and is of the wrong phase for self-development. The contribution from thermal advection is small because of the reduced baroclinity near the non-developing center. The net tendency (Fig. 5.15 j-l) results in increasing (decreasing) thicknesses behind (ahead of) the dissipating surface center. The development of a 500 mb ridge to the northwest of the center (Fig. 5.8 e), which is consistent with these changes, appears to augment the NVA directly above the center. These changes oppose the vertical mass circulation and development of the low-level trough. In contrast, thickness changes associated with the developing Type II disturbance (Fig. 4.18) are consistent with self-development and the growth of PVA aloft.

The large thermal advection dipole (Fig. 5.15 a,b) and associated thickness tendency dipole (Fig. 5.15 j,k) to the south are linked to the developing disturbance there. The large dipole amplitude, which occurs because of the enhanced baroclinity in the south of the domain, is favorable for self-development. As these patterns are partially incorporated into the 5° latitude radius budget volume, the vorticity and heat budgets centered on the dissipating system to the north must be carefully interpreted.

3. Discussion

The Type II polar low was shown to be a baroclinic disturbance which is triggered by PVA aloft. Development is associated with a developing upper-level trough that is coupled to the surface cyclone. The non-developing Type II disturbance studied in this section is a large-scale vortex which decays as a result of surface friction. Although the
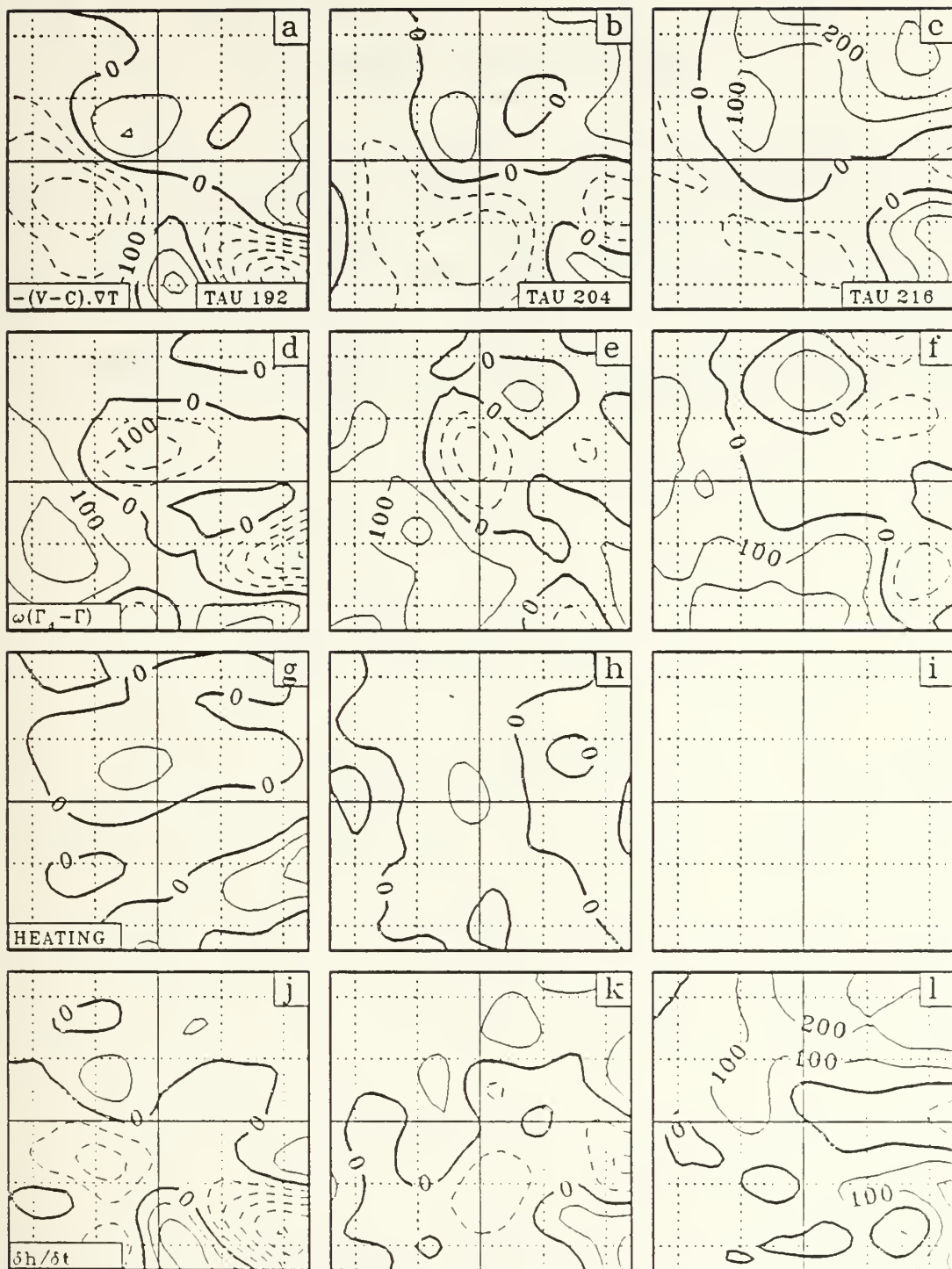
Fig. 5.15.   As in Fig. 5.6 except for non-developing NOGAPS
Type II. No contours are drawn in (i) since
values are close to zero.

163

vorticity budget indicates large PVA aloft, this is not
properly colocated with the dissipating center. An ampli-
fying short-wave trough aloft and associated PVA is coupled
with another developing system to the south, which happens
to be incorporated into the budget volume. The thickness
changes associated with the decaying system actually oppose
the development of upper-level PVA. Thus, the system slowly
dissipates as the upper-level support decreases. As for the
non-developing Type I disturbance, the absence of favorable
coupling with the upper-level jet streak and associated PVA
is the major factor which led to the decay of this system.

VI. SUMMARY AND CONCLUSIONS

The purpose of this study has been to determine the reasons for the growth of baroclinic disturbances which form within polar air streams. Formation and development of these polar lows have been studied using quasi-Lagrangian (storm-following) budgets of vorticity, heat and moisture. These diagnostic analyses have been applied to polar lows from two data sets. The first set is from the model simulations of Sandgathe (1981). These simulated polar lows formed in the polar air stream of a mature extratropical cyclone. Therefore, the effects of nonlinear deformation processes associated with the parent low are included at polar low formation. These conditions are more realistic than in the many modeling studies in which the disturbance forms on a zonal (unperturbed) basic state. The second set is the European Center for Medium Range Weather Forecasts (ECMWF) analyses of observational data from the First GARP Global Experiment (FGGE). This study extends the diagnostic analysis of a polar low previously studied by Cook (1983) and Wash and Cook (1985). A second polar low has been extracted from the FGGE analyses for in-depth studies. Since the FGGE analyses incorporate extensive supplemental observations over the oceans, they are especially suitable for the study of maritime weather systems.

This study uses a combination of simulated and observational data. The distribution of observational data over the ocean is sometimes inadequate to resolve small-scale disturbances. By contrast, model output forms a dynamically consistent data set which is available at every gridpoint to computer roundoff accuracy at every time step. Such a complete specification of physical processes cannot be

165

achieved in an observational study. The increased time resolution of model output was very beneficial in resolving the rapid changes in these polar disturbances. The completeness of the model-generated fields allowed evaluation of interpolation and other computational errors associated with the various diagnostic routines, and enabled closure of budgets to acceptably small residuals. While strong conclusions are possible only on the model budgets, the realism of the model simulations is demonstrated by similar, although noisier, budgets from the observational data set.

The use of cubic splines enables accurate estimates of instantaneous time derivatives without time averaging. Spatial averaging is avoided by the use of a bicubic spline fit to the horizontal data. Thus, these cubic spline techniques preserve the spatial and temporal resolution of the data, and reduce the truncation error associated with calculation of space and time derivatives. The improved space and time resolution associated with the use of cubic splines appear to be beneficial in the analysis of small-scale, short-lived disturbances such as the polar low.

Two types of polar low are identified from this study on the basis of the conditions existing during the formative stage. The first (Type I) forms on the equatorward side of an upper-level jet streak under straight or anticyclonic flow aloft. The disturbance is initiated by low-level baroclinic processes, and is characterized in its early stages by a weak, surface circulation with light winds. The second (Type II) forms in a strong surface polar air stream on the cyclonic side of the upper-level wind maximum. This type is initiated by positive vorticity advection (PVA) aloft. Non-developing examples of both Type I and Type II polar lows are also examined. Comparisons between developing and non-developing cases provide additional insight into reasons for polar low intensification.

A new finding arising from this study is that polar lows may form beneath straight flow aloft on the equatorward side of the jet. There is some controversy concerning the necessity of a short wave aloft during polar low formation and intensification. The composite study of Mullen (1979) and the case studies of Reed (1979), Locatelli et al., (1982), and Mullen (1983) showed that polar lows that form on the cyclonic side of the upper-level jet have a perturbed upper flow during early stages of development. These studies represent examples of Type II polar lows. However, the Type I polar lows identified by the present study form on the equatorward side of the jet beneath straight flow aloft. Although a similar genesis structure has previously been noted for extratropical cyclones (e.g., Petterssen and Smebye's (1971) Type A cyclogenesis), and for so-called "medium-scale" disturbances which form east of Japan (Nitta and Yamamoto, 1974; Chen et al., 1985), these conditions have not hitherto been applied to the polar low.

One of the main conclusions from this study is that both Type I and Type II polar lows form and grow primarily through basic baroclinic instability processes, and thus exhibit many of the features of larger maritime extratropical cyclones. Genesis occurs in an area of enhanced baroclinity that is associated with an upper-tropospheric jet streak. As the polar low intensifies, the baroclinity decreases. The vertical ascent for the model-generated cases exhibits a comma-shaped signature. The comma tail is located in a surface pressure trough in an area of enhanced baroclinity. Another area of enhanced baroclinity occurs to the east of the surface low. These features are similar to the classical frontal cyclone. Similar frontal structure was previously observed by Locatelli et al., (1982) for a number of North Pacific polar lows.

This study shows that polar lows are associated with enhanced baroclinity and reduced static stability, which is consistent with the conclusion that these disturbances are baroclinic phenomena. The small size of the polar low is due to the low Richardson number (indicated by the combination of strong baroclinity and low static stability) as suggested by Mullen (1979). Small-scale baroclinic disturbances are favored when the Richardson number is small near the surface (Gall, 1976a; Staley and Gall, 1977).

In strong, cold air outbreaks in which Type II polar lows grow, this study has shown that enhanced surface friction, and sensible heat fluxes may oppose formation of an unstable surface perturbation. Surface friction opposes the growth of low-level vorticity. Surface heating is largest in the coldest air, which tends to reduce the baroclinity. Addition of heat in antiphase with the growing temperature perturbation associated with a baroclinically unstable disturbance opposes development. Because of these stabilizing effects, it is suggested that the surface disturbance requires mass circulation increases which are triggered by PVA aloft. The stabilizing influence of the surface fluxes and the requirement for significant upper-level PVA possibly explains the rarity of polar lows compared to the frequency of strong cold outbreaks.

The composite study of Mullen (1979) indicates that polar lows tend to form in areas of enhanced air-sea temperature difference, which implies a cyclogenetic role for the surface fluxes. A hypothesis to explain this paradox regarding the role of the surface sensible heat flux in the case of the Type II polar lows has been suggested by this study. These polar lows tend to form in a low static stability environment. Strong surface heating may then lead to further destabilization throughout a deep layer. A combination of strong surface heating and cooling aloft in the

cold sector could enhance development of the upper trough. Although strong surface fluxes oppose surface low formation, it is hypothesized that strong surface heating in the cold air may indirectly contribute to polar low development via enhancement of the self-amplification process in the mid-troposphere. Type II polar lows form on the cyclonic side of the jet where a combination of reduced static stability through a deep layer, enhanced surface heating and PVA aloft create an environment conducive to development. In comparison, the surface fluxes for the Type I disturbance are weak, and the initial perturbation, which is triggered by low-level baroclinic processes, will form near the maximum surface temperature gradient. Because an east-west baroclinic zone slopes toward the pole, the Type I surface low will tend to form on the equatorward side of the upper jet.

The budget analyses reveal several physical processes that are normally associated with a growing baroclinic wave. In both Type I and Type II polar lows, development is accompanied by an increasing vertical mass circulation. The increasing mass inflow at low levels results in vorticity generation, while increasing PVA aloft that is associated with an amplifying geopotential wave tends to offset the divergence sink. This upper-level wave is coupled with the intensifying surface low. The growth of the upper wave is more rapid for the Type II polar low. In the Type I case, generation of positive (negative) vorticity by convergence (divergence) is less efficient in the low absolute vorticity environment on the anticyclonic side of the upper jet. The budgets for the model-generated data are similar in most respects to those from the observational data. However, data uncertainty results in less reliable diagnoses of budget terms in the observational case. The vorticity budget results for both types are rather similar to studies of larger scale extratropical cyclones over or along the east

169

coasts of continents (e.g., Chen and Bosart, 1979; DiMego and Bosart, 1982; Calland, 1983; Bosart and Lin, 1984).

The growth of terms in the heat budgets of both types reflect the growing mass circulation. Diabatic processes, in particular condensation in the ascending air, augment the vertical mass circulation. This leads to increased vorticity generation near the surface and contributes to growth of the upper-level wave. A similar role for latent heat release has previously been described for extratropical cyclones (e.g., Smagorinsky, 1956; Aubert, 1957; Danard, 1964). Latent heat release in the warm sector of the developing polar low leads to an increase in the available potential energy (APE) of the system. Intensification of the polar low is accompanied by baroclinic conversion of this eddy APE to eddy kinetic energy (KE), in accord with previous work for mid-latitude cyclones (e.g., Danard, 1966; Bullock and Johnson, 1971; Gall, 1976b; Vincent et al., 1977; Robertson and Smith, 1983). The numerical study of Hodur (1984) showed that the inclusion of condensation results in increased generation of of eddy APE and conversion to eddy KE in Pacific polar lows.

A second conclusion of this study is that the sequence of self-development (Sutcliff and Forsdyke, 1950) that has been previously applied to larger scale extratropical cyclones (e.g., Palmen and Newton, 1969), applies to the developing polar low. Self-development indicates a cooperative coupling between lower and upper-level features. Self-development is suggested by thickness change patterns of warming (cooling) ahead of (behind) the surface low center. Such changes are hydrostatically consistent with amplification of the upper-level geopotential wave.

In contrast with the developing cases, thickness change patterns in the non-developing cases studied here do not favor self-development. The lack of development in these cases is ascribed to the lack of coupling of lower and

upper-level features. The presence of a vigorous baroclinic disturbance just downstream of the non-developing system appears to oppose the mass circulation of the non-developing case by maintaining upper-level NVA and convergence.

The budget results demonstrate the importance of the nonlinear effects due to thermal and vorticity advection. Mid-tropospheric vorticity advection is required for the genesis of the Type II polar low. Thus, the importance of nonlinear terms at polar low genesis cannot be dismissed. At later stages of development of both polar low types, strong deformation fields due to thermal and vorticity advection create conditions which appear to be favorable for future formation of secondary disturbances. Thermal advection contributes to frontogenesis in areas to the southwest and east, which are the expected locations of cold and warm fronts. These areas of enhanced baroclinity occur in conjunction with upper-level cyclogenesis. The associated PVA appears to initiate vertical ascent which would contribute to the development of a surface disturbance. It is suggested that diagnosis of frontogenesis and upper-level cyclogenesis may be the key to predicting the likelihood and location of subsequent secondary low formation.

This study indicates that the NOGAPS model does not appear to simulate the occlusion process well. The observational data exhibit a well-defined peak in the strength of the vertical mass circulation, with a decrease in the vertical slope of the geopotential features. By contrast, the model appears to maintain the strength of the vertical mass circulation, and have only a modest decrease in the vertical slope. A second deficiency in the NOGAPS model is that the effects of cumulus heating appear to be underestimated. Cumulus processes result in the addition of heat higher in the troposphere than latent heat release arising from large-scale ascent. Heating aloft and cooling near the

surface lead to stabilization of the atmosphere, which results in the demise of the storm. In the NOGAPS cases analysed in this study, large-scale ascent remains strong.

Future studies of polar lows should focus on the conditions that lead to genesis. Because the polar low is a short-lived phenomenon, a better understanding of genesis conditions would enable more timely forecasts of polar low formation. Further research should clarify the role of the deformation fields of the parent low in the formation of secondary disturbances. Attention should also be focused on the evolution of low-level baroclinity in the presence of surface fluxes. Future modeling studies of polar lows should focus on the formation of secondary disturbances in polar airstreams to determine the role of processes which are associated with the parent low. Studies based on idealized zonal initial conditions may underestimate these nonlinear processes.

Polar lows are poorly resolved by observational data. Data insertion schemes based on subjective interpretations of satellite imagery will be necessary in lieu of new data sources. The vertical ascent signature provides information about the divergent component of the wind aloft. Objective analyses of polar lows should reproduce the vertical ascent signature, and other satellite-viewed features such as the direction of cloud streets, cirrus striations and cirrus blow-off from cumulonimbus anvils. Given these improved initial conditions, the existing models appear to contain the physical processes for predicting the formation and intensification of polar lows of the type studied here. Thus, there is some hope of improved forecasts of these vigorous weather systems.

APPENDIX A
DIAGNOSTIC FORMULATION

A. QUASI-LAGRANGIAN BUDGET

This study utilizes the geometry of the quasi-Lagrangian diagnostic budget framework formulated by Johnson and Downey (1975).   The budget equations are derived in a variation of spherical   coordinates   for   nearly-cylindrical   volumes consisting of   sections of   the cone   from the   earth center contained between isobaric surfaces (Fig. A.1).   The volume translates with velocity $\mathbb{C}$, and moves with the storm.

The generalized isobaric budget expression of the quantity f is obtained by expanding the substantial derivative of f and integrating each term over the volume enclosed between pressure levels p_1 and p_2 of horizontal area ΔA. This yields

$$\underbrace{\frac{1}{P_2-P_1} \int_{P_1}^{P_2} \frac{\delta \overline{\overline{f}}}{\delta t}\, dp}_{T} \quad = \quad \underbrace{\frac{\Delta L}{\Delta A} \frac{1}{P_2-P_1} \int_{P_1}^{P_2} \overline{f}(\overline{V}_n - \overline{C}_n)\, dp}_{HM}$$

$$+ \underbrace{\frac{\Delta L}{\Delta A} \frac{1}{P_2-P_1} \int_{P_1}^{P_2} \overline{f'(V_n'-C_n')}\, dp}_{HE} + \underbrace{\frac{1}{P_2-P_1}[\overline{\overline{f}}\;\overline{\overline{\omega}}\,|_{P_2} - \overline{\overline{f}}\;\overline{\overline{\omega}}\,|_{P_1}]}_{VM}$$

$$+ \underbrace{\frac{1}{P_2-P_1}[\overline{\overline{f^*\omega^*}}\,|_{P_2} - \overline{\overline{f^*\omega^*}}\,|_{P_1}]}_{VE} + \underbrace{\frac{1}{P_2-P_1} \int_{P_1}^{P_2} \overline{\overline{S}}\, dp}_{S} + \underbrace{R}_{R} \qquad (A.1)$$

173
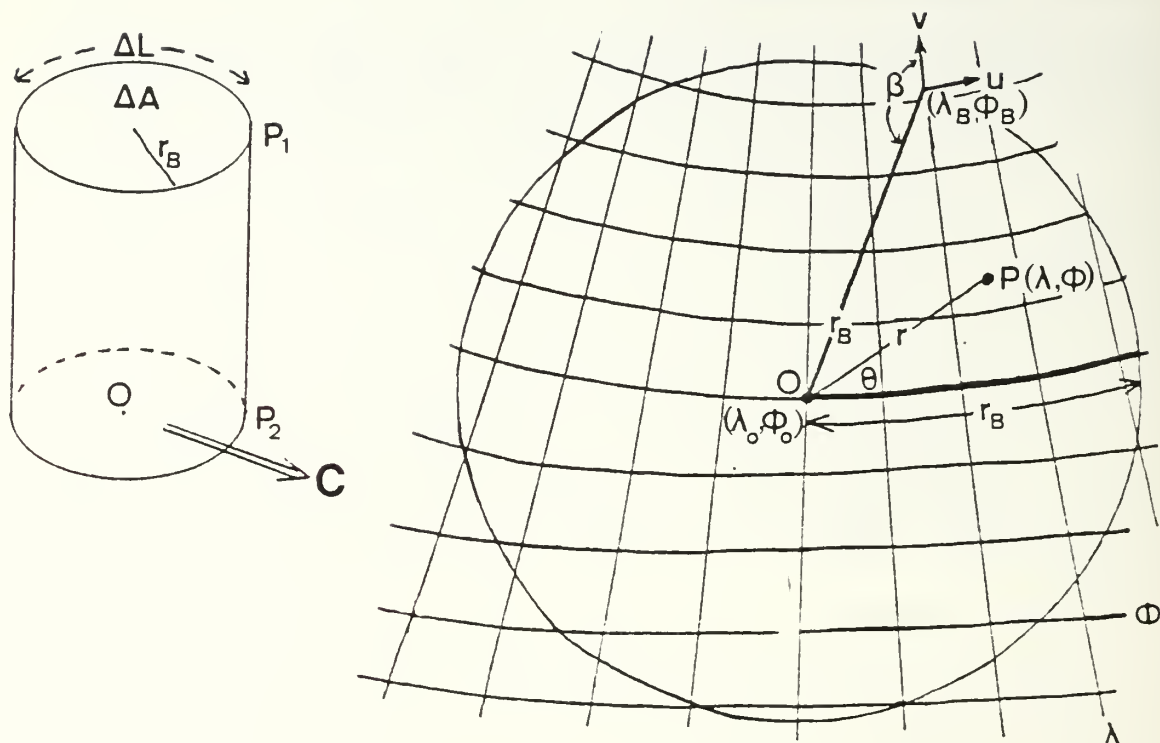
Fig. A.1. Budget volume geometry.

where $\overline{f}$ is the line-average of f around the circumference (ΔL) of the budget volume, $\overline{\overline{f}}$ is the area-average over the budget cross-sectional area (ΔA), and ($V_n - C_n$) is the inward-directed component of velocity normal to the translating boundary. Budget terms are in units of f per unit time. The deviation terms are computed as

$$f' = f - \overline{f} \quad \text{(at each circumference point)} \tag{A.2}$$

174

$$f^{*} = f - \bar{\bar{f}} \quad \text{(at each grid-point)} \qquad (A.3)$$

In (A.1), term (T) is the quasi-Lagrangian volume average rate of change of f. Terms (HM) and (HE) are the gains of f due to convergence of mean and eddy horizontal fluxes. Terms (VM), (VE) represent increases in f due to vertical mean and eddy flux convergence (computed as the inflow through the lower boundary minus the outflow through the top). Term (S) represents the volume-averaged sources and sinks, specified via the conservation equation for the quantity f. Term (R) is the budget residual. A positive residual indicates that the observed increase of f is larger than is estimated by the sum of the computed terms.

1. Computational Method

Calculation of the terms in (A.1) follows Johnson and Downey (1975). A generalized point P (see Fig. A.1) at polar coordinates (r, θ) within the budget area has a latitude of

$$\phi = \sin^{-1}[\sin(\phi_o + \frac{r}{a}) - (1 - \sin \theta) \sin(\frac{r}{a}) \cos \phi_o] \qquad (A.4)$$

and longitude of

$$\lambda = \lambda_o + \sin^{-1}[\frac{\sin(\frac{r}{a}) \cos \theta}{\cos \phi}] \qquad (A.5)$$

where ϕ and λ are the latitude and longitude at the center (0) of the budget area, and a is the earth radius. All angles are in radians. The quantity r is the arc length OP along the earth surface, and the angle θ is the azimuthal angle that this arc makes with the eastward-pointing vector at O. The quantity r/a in A.4 and A.5 is the angle subtended at the earth center by the arc OP. The component of

velocity normal to the boundary (positive inward) at the point (r_B, θ) is given by

$$V_n = u(r_B, \theta) \sin \beta - v(r_B, \theta) \cos \beta \qquad (A.6)$$

where the angle β is

$$\beta = \sin^{-1}[\cos \phi_0 \frac{\cos \theta}{\cos \phi_B}] \qquad (A.7)$$

and the subscript B refers to a point on the boundary. The inward-directed component of C normal to the boundary is computed as

$$C_n = \|\mathbf{C}\| \cos[\theta - \tan^{-1}(\frac{C_y}{C_x})] \qquad (A.8)$$

where C_x and C_y are the eastward and northward components of $\mathbf{C}$. The area average of f is calculated as

$$\overline{\overline{f}} = [2\pi a(1 - \cos(\frac{r_B}{a}))]^{-1} \int_0^{r_B} \int_0^{2\pi} f(r, \theta) \sin(\frac{r}{a}) d\theta dr \qquad (A.9)$$

The line average of f is

$$\overline{f} = \frac{1}{2\pi} \int_0^{2\pi} f(r_B, \theta) d\theta \qquad (A.10)$$

Simpson's 3/8 rule is used for both integrals. For the vertical integrals, a quadrature integration routine based on a cubic spline representation of the integrand is used. This is more accurate than the simpler additive vertical integration schemes commonly used. The circumference and area of the budget volume are computed as

$$\Delta L = 2\pi a \sin(\frac{r_B}{a}) \qquad (A.11)$$

and

176

$$\Delta A = 2\pi a^2 [1 - \text{Cos}(\frac{r_B}{a})] \hspace{2cm} (A.12)$$

To compute the terms in the budget expression (A.1) above, the meteorological variables are first interpolated from the rectangular lat/lon grid to the spherical storm-following budget grid. Equations (A.4) and (A.5) above are used to define the polar grid in terms of the rectangular lat/long grid. Then (A.1) is evaluated with the aid of equations (A.6) to (A.12). The budget grid used throughout is of dimension 36 (azimuth) by 6 (radial) with a radial grid spacing of 1° latitude.

Raw fields of NOGAPS output variables were found to be rather noisy, with apparently random grid-length scale perturbations superposed on the synoptic-scale variations. Additional random uncertainty is introduced during the vertical interpolation from sigma to pressure coordinates. Horizontal interpolation is performed by fitting a cubic to the data on the rectangular lat/long grid as described earlier. With noisy data, this cubic will vary widely between data points, and intensify the noise on the budget grid. For these reasons, all model fields were smoothed prior to horizontal interpolation by using a 25-point smoother developed by Bleck (1965). The filter eliminates short-wave noise while retaining the shape and magnitude of the synoptic-scale features. The filter also preserves the area average on the grid, an essential feature for a budget formulation.

2. Calculation of Kinematic Vertical Velocities

From (A.1), it is apparent that an estimate of vertical velocity is required for the budget calculation. This is obtained kinematically by vertical integration of the divergences. Suitable boundary conditions must be imposed on omega at the top and bottom of the atmosphere.

For the NOGAPS model, omega is assumed zero at 50 mb. For the FGGE analysis, omega is zero at 0 mb. Using the appropriate boundary value, omega is computed at each point as

$$\omega(p) = \omega(P_T) - \int_{P_T}^{P} \nabla_p \cdot \mathbf{V} \, dp \qquad (A.13)$$

A vertical spline fit to the vertical distribution of divergence at each gridpoint is used to evaluate this integral. The technique avoids the cumulative error growth which occurs with the simpler additive downward integration schemes commonly used in the kinematic calculation.

The bicubic spline fit to the u and v components of the wind is used to evaluate the divergences on the new grid. To ensure consistency with NOGAPS and FGGE formulations, earth curvature terms were added. The resulting divergences were adjusted slightly so that their area integral was exactly equal to the line integral of the inflow velocity around the boundary. This equality (Gauss' Theorem) is a central assumption of the budget formulation. Prior to adjustment, the two quantities differed by less than 1% of typical values. This excellent agreement attests to the mutual consistency of the interpolated wind and the divergence. Using the adjusted divergences, values of omega (vertical velocity) were then derived kinematically using (A.13) for each point on the new grid.

Because the model winds are known to computer round-off accuracy, the vertically integrated total column divergences were used as the lower boundary value for omega. By comparison, it was considered that the substantial derivative of surface pressure computed using the quasi-Lagrangian estimates of pressure tendency and translation velocity from three-hourly data was poorly known. Therefore, no adjustment was made to the divergences. Three estimates of the substantial derivative were shown earlier

178

in Fig. A.2. The differences between these estimates reflect the effects of smoothing, interpolation, and time averaging. The instantaneous Eulerian pressure tendency is a model output field. The vertically integrated divergence yields realistic values of the substantial derivative, which
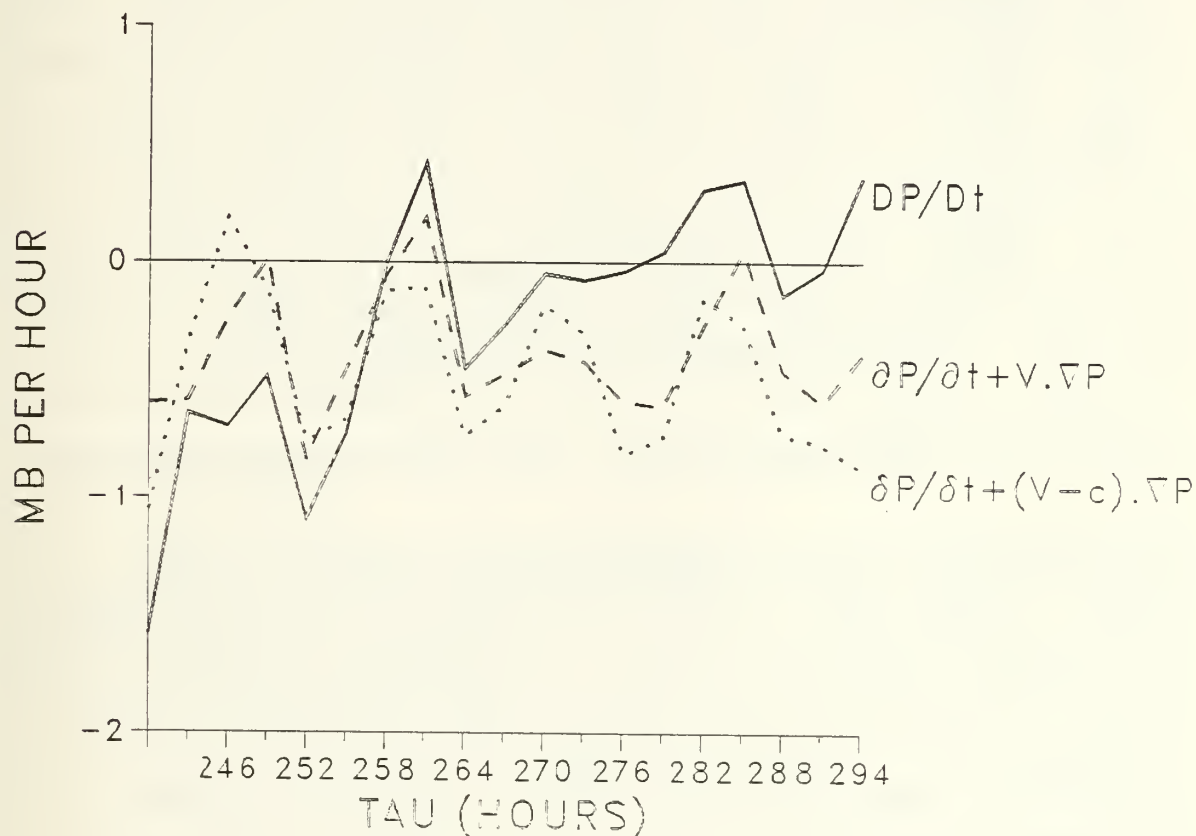
Fig. A.2. Three estimates of DP/Dt (mb h-¹).

For the FGGE data, the winds were considered to be poorly known. Therefore, the vertical velocities and divergences were adjusted to fit both boundary conditions, using the procedure outlined by O'Brien (1970). An analytic weighted correction to the vertical divergence profile was employed. This weighting function

$$C(p) = (1000-P)/2000 + 0.8e^{-0.01(1000-P)} \qquad (A.14)$$

has the form shown in Fig. A.3.
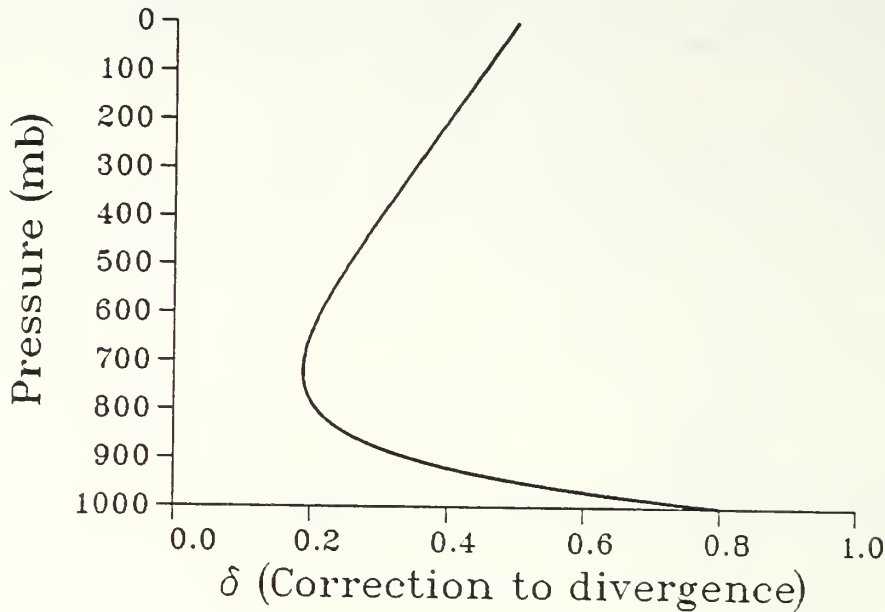
Fig. A.3. Weighting function for correcting divergences.

This function corrects preferentially near the surface, and aloft. Above about 700 mb, the function increases linearly with height to allow for the increasing uncertainty with height of rawinsonde wind data. Wind observations near the surface contain much uncertainty as a result of differing anemometer exposures and boundary layer turbulence (wind gustiness). For this reason, the strongest correction was applied below 900 mb, as shown in Fig. A.3. The area-averaged divergences were corrected by an amount C(P) where δ is obtained from

$$\frac{\delta \bar{\bar{P}}_S}{\delta t} + \overline{(\mathbf{V} - \mathbf{C}) \cdot \mathbf{V}P_S} = \int_{P_T}^{P_S} [-\nabla \cdot \mathbf{V} + \delta C(p)] dp \qquad (A.15)$$

The second term in the integrand of A.15 is just the integral of A.14. The corrected divergences were then used to compute omega using A.13.

The kinematic estimates of omega obtained by this method ensure mass balance at each point on the budget grid. This is necessary to avoid spurious sources and sinks in budgets of other quantities. In the vorticity, heat and moisture budgets, the horizontal and vertical transport terms associated with the mean circulation are each often an order of magnitude larger than the internal sources and sinks. However, their sum (net mean flux convergence) is rather small, and may be less than the sources and sinks. Therefore, in the present work, the mean mass circulation is balanced to better than 0.1% on the budget volume. This mass budget formulation differs from other budget studies in that mass balance is achieved at each gridpoint on the budget volume as well as in an area-averaged sense. This property is essential since mass continuity is an integral feature of model formulation at each gridpoint, and is assumed in the budget formulation. By this method, spurious sinks and sources in the eddy terms arising from mass imbalance are avoided.

As a check on the reliability of the kinematic calculations for the NOGAPS fields, the kinematically derived omegas were compared with the model vertical motion fields. In sigma coordinates,

$$\omega_O = (P_S - P_T)\dot{\sigma} + \sigma(\frac{\partial P_S}{\partial t} + \mathbf{V}_\sigma \cdot \nabla P_S) \qquad (A.16)$$

where the first term on the right side of (A.16) is the model vertical motion in sigma coordinates. The omega fields calculated from (A.16) were interpolated directly to the pressure sufaces. Fields of omega (not shown) derived using (A.16) from the model vertical motion and computed using the kinematic method of this section are qualitatively very similar and differ quantitatively by only a few percent. This close agreement suggests that the spline estimates of

horizontal derivatives are consistent with the finite difference approximation used in the NOGAPS formulation to compute the vertical velocity. However, to ensure mass balance, the kinematic rather than the model omegas are used for the budget calculations.

3. Calculation of Translation Velocity

To position the budget volume, the maximum surface absolute vorticity is used initially as a first guess. The track obtained is then smoothed using a least-squares fit to a smooth cubic spline for both the time series of latitude and longitude. The smooth track so obtained departed by no more than half a degree latitude from the first guess. The smoothed track positions are used to locate the budget volume. The x and y components of the instantaneous translation velocity are obtained as

$$C_x = a \cos \phi \frac{\partial \lambda}{\partial t}, \quad C_y = a \frac{\partial \phi}{\partial t} \tag{A.17}$$

where and are the latitude and longitude of the budget volume at time t. The time derivatives are computed by differentiating the the cubic spline fit to the smoothed time-series of λ and Φ. This method produces a smoothly varying instantaneous translation velocity and minimizes spurious accelerations of the polar low. The instantaneous time derivatives of vorticity, heat, etc., are computed in the same manner using a spline fit in time. These procedures enable computations of budget terms at each output time without time averaging.

4. Transport Partitioning

The gains due to lateral and vertical transports of the budget quantity f are partitioned into mean and eddy mode components, as shown in (A.1). The mean component is

the change of f in the volume due to net flux convergence or
divergence associated with the mean circulation.   However,
it is the small imbalance between the mean lateral inflow of
f and its vertical redistribution that contributes to the
change of f.

The horizontal eddy term represents the covariance
of inflow and values of f on the perimenter.   A positive
eddy term results from inwardly directed wind components
having large f values and/or outward flow with small f.   The
eddy term may be written as

$$\overline{V_{n.}' f'} = \overline{V_n f} - \overline{V_n} \overline{f} \tag{A.18}$$

By Gauss' Theorem

$$\overline{V}_n = \frac{\Delta L}{\Delta A} \overline{\overline{\nabla \cdot \mathbf{V}}} \tag{A.19}$$

and

$$\overline{V_n' f'} = \frac{\Delta L}{\Delta A} \overline{\overline{\nabla \cdot (f\mathbf{V})}} \tag{A.20}$$

Therefore,

$$\overline{\overline{V_n' f'}} = \frac{\Delta L}{\Delta A} \overline{\overline{\mathbf{V} \cdot \nabla f}} + \frac{\Delta L}{\Delta A} [\overline{\overline{f \nabla \cdot \mathbf{V}}} - \overline{f} \; \overline{\overline{\nabla \cdot \mathbf{V}}}] \tag{A.21}$$

Thus,   the eddy term is equivalent to the area averaged
advection of f only when the area average of the product of
divergence and f equals the product of the area averaged
divergence and the boundary mean value of f. This is approx-
imately true when boundary and area averages of f agree
closely and the perturbation quantities are small compared
with the   mean. Such conditions are best fulfilled with a
small budget volume. For a horizontal distribution of f
and/or inflow that is symmetric with respect to the budget

volume, the eddy term will be small. Thus, this term is related to the asymmetry of the storm. The vertical eddy term represents changes in f due to the vertical difference between the spatial covariance of omega and f on the top and bottom surfaces of the budget volume. As such, it is qualitatively similar to the vertical advection of f.

B. CALCULATION OF QUASI-LAGRANGIAN ADVECTION TERMS

Display of advection terms on a rectangular lat/long box poses a special problem in spherical coordinates because not all parts of such a box translate with the same velocity. For example, a box of fixed lat/long dimensions travelling north in the northern hemisphere shrinks in size. To remedy this problem, a correction is made to the translation velocity at each point within the box. (No such correction is required for the circular budget volume, since its area is constant.) This correction can be substantial, especially for a large display box having a large meridional translation velocity. The divergence in spherical coordinates may be written

$$\nabla \cdot \mathbf{V} = \frac{1}{a \cos \phi} \frac{\partial u}{\partial \lambda} + \frac{1}{a} \frac{\partial v}{\partial \phi} - \frac{v}{a} \tan \phi \qquad (A.22)$$

Because every element of the box is translating with the constant vector velocity $C = (c_x, c_y)$, it follows that

$$\frac{1}{a \cos \phi} \frac{\partial C_x}{\partial \lambda} + \frac{1}{a} \frac{\partial C_y}{\partial \phi} - \frac{1}{a} C_y \tan \phi = 0 \qquad (A.23)$$

Geometrically, it is apparent that only the east-west dimension of the volume changes with north-south translation. Therefore, the second term on the right hand side of (A.23) is zero, yielding

$$\frac{\partial C_x}{\partial \lambda} = C_y \frac{\sin \phi}{a} \qquad (A.24)$$

184

or

$$C_x(\lambda) = C_x + (\lambda - \lambda_o) C_y \sin \phi_o \qquad (A.25)$$

where $\lambda - \lambda_o$ is the eastward displacement in radians from the meridian passing through the center point.

The calculation of the vorticity advection term is described to illustrate the use of spherical coordinates. The relative vorticity in spherical coordinates is given by

$$\zeta_r = \frac{1}{a \cos \phi} \frac{\partial v}{\partial \lambda} - \frac{1}{a} \frac{\partial u}{\partial \phi} + \frac{u}{a} \tan \phi \qquad (A.26)$$

The x-component of the vorticity gradient is obtained by differentiating (A.26) with respect to x to obtain

$$\frac{\partial \zeta_r}{\partial x} = \frac{1}{a^2 \cos^2 \phi} \frac{\partial^2 v}{\partial \lambda^2} - \frac{1}{a^2 \cos \phi} \frac{\partial^2 u}{\partial \lambda \partial \phi} + \frac{1}{a^2 \cos \phi} \frac{\partial u}{\partial \lambda} \tan \phi$$
$$(A.27)$$

Similarly, the y-component of the vorticity gradient is

$$\frac{\partial \zeta_r}{\partial y} = \frac{1}{a^2 \cos \phi} \frac{\partial^2 v}{\partial \lambda \partial \phi} - \frac{1}{a^2} \frac{\partial^2 u}{\partial \phi^2} + \frac{1}{a^2} \tan \phi \frac{\partial u}{\partial \phi}$$
$$+ \frac{u}{a^2 \cos^2 \phi} \qquad (A.28)$$

So, finally, using (A.25), (A.27) and (A.28), the vorticity advection is given by

$$-(\mathbf{V} - \mathbf{C}) \cdot \nabla \zeta_r = -[u - C_x - (\lambda - \lambda_o) C_y \sin \phi] \frac{\partial \zeta_r}{\partial x}$$
$$- (v - C_y) \frac{\partial \zeta_r}{\partial y} \qquad (A.29)$$

185

The derivative terms in (A.27) and (A.28) are obtained from
the bicubic spline fit to the rectangular array of u and v
data in (,) space and are mutually consistent. This tech-
nique avoids the space-averaging inherent in finite differ-
ence methods. The calculation of the thermal advection on
the horizontal lat/long grid follows (A.29).

LIST OF REFERENCES

Anderson, R.K., J.P. Ashman, F. Bittner, G.R. Farr, E.W. Ferguson, V.J. Oliver and A.H. Smith, 1969: Application of meteorological satellite data in analysis and forecasting. ESSA Tech. Rep. NESC 51 (NTIS AD-697 033).

Arakawa, A., and V. Lamb, 1977: Computational design of the basic dynamical processes of the UCLA general circulation model. Methods in Computational Physics, 17, 173-265, Academic Press, New York.

----- and W. Schubert, 1974: Interaction of a cumulus cloud ensemble with the large-scale environment, part I. J. Atmos. Sci., 31, 674-701.

Aubert, E.J., 1957: On the release of latent heat as a factor in large scale atmospheric motions. J. Meteor., 14, 527-542.

Baker, D.J., Jr., 1979: Ocean-atmosphere interaction in high southern latitudes. Dynam. Atmos. Oceans, 33, 213-229.

Bengtsson, L., M. Kanamitsu, P. Kallberg, and S. Uppala, 1982: FGGE 4-dimensional data assimilation at ECMWF. Bull. Amer. Met. Soc., 63, 29-43.

Bleck, R., 1965: Lineare Approximationsmethodem zur Bestimmung ein-und zweidimensionaler numerischer Filter des dynamischen Meteorologie, Institut fur Theoretische Meteorologie der Freien Univeristat Berlin.

Blumen, W., 1980: On the evolution and interaction of short and long baroclinic waves of the Eady type. J. Atmos. Sci., 37, 1984-1993.

Bosart, L.F., 1981: The Presidents' Day snowstorm of 18-19 February 1979: A subsynoptic-scale event. Mon. Wea. Rev., 109, 1542-1566.

_____, and S. C. Lin, 1984: A diagnostic analysis of the Presidents' Day snowstorm of February 1979. Mon. Wea. Rev., 112, 2148-2177.

Bosse, T.E., 1984: An evaluation of the NOGAPS diabatic parameterization and the contribution of diabatic heating in a case of explosive maritime cyclogenesis. M.S. Thesis, Department of Meteorology, Naval Postgraduate School, 115 pp.

Bullock, B.R., and D.R. Johnson, 1971: The generation of available potential energy by latent heat release in a mid-latitude cyclone. Mon. Wea. Rev., 99, 1-14.

Calland, W.E., 1983: Quasi-Lagrangian diagnostics applied to an extratropical cyclogenesis in the North Pacific. M.S. Thesis, Department of Meteorology, Naval Postgraduate School, 154 pp.

Carleton, A.M., 1981: Monthly variability of satellite-derived cyclone activity for the Southern Hemisphere winter. J. Climatol., 1, 21-38.

Carr, F.H., and J.P. Millard, 1985: A composite study of comma clouds and their association with severe weather over the Great Plains. Mon. Wea. Rev., 113, 370-387.

Charney, J.G., 1947: The dynamics of long waves in a baroclinic westerly current. J. Meteor., 5, 135-162.

-----, and A. Eliassen, 1964: On the growth of the hurricane depression. J. Atmos. Sci., 24, 68-75.

Chen, T.-G., and L.F. Bosart, 1979: A quasi-Lagrangian vorticity budget of composite cyclone-anticyclone couplets accompanying North American polar air outbreaks. J. Atmos. Sci., 24, 185-194.

-----, C.-B. Chang and D.J. Perkey, 1985: Synoptic study of a medium-scale oceanic cyclone during AMTEX '75. Mon. Wea. Rev., 113, 349-361.

Clark, R.H., 1977: Some remarks on the subject of fronts. Two Day Workshop on Fronts, Conference Handbook, Melbourne. (Available from Royal Meteorological Society, Australian Branch).

Cook, W.A., 1983: A quasi-lagrangian diagnostics investigation of rapid cyclogenesis in a polar airstream. M.S. thesis, Dept. Meteorol., Naval Postgraduate School, Monterey, 147 pp.

Danard, M.B., 1964: On the influence of released latent heat on cyclone development. J. Appl. Meteor., 3, 27-37.

-----, 1966: A quasi-geostrophic numerical model incorporating the effects of release of latent heat. J. Appl. Meteor., 5, 85-93.

-----, and G.L. Ellenton, 1980: Physical influences on east coast cyclogenesis. Atmosphere-Ocean, 18, 65-82.

Deardorff, J.W., 1972: Parameterization of the planetary boundary layer for use in general circulation models. Mon. Wea. Rev., 100, 93-106.

DiMego, G.J., and L.F. Bosart, 1982: The transformation of tropical storm Agnes into an extratropical cyclone. Part II: Moisture, vorticity and kinetic energy budgets. Mon. Wea. Rev., 110, 412-433.

Duncan, C.N., 1977: A numerical investigation of polar lows. Quart. J. Roy. Meteor. Soc., 103, 255-268.

Eady, E.T., 1949: Long waves and cyclone waves. Tellus, 1, 33-52.

Forbes, G.S., and W.D. Lottes, 1982: Characteristics and evolution of mesoscale cloud vortices occurring in polar airstreams. Preprint Volume of Extended Abstracts, Conference on Cloud Physics, Nov. 15-18, 1982, Chicago, Ill., AMS, Boston, Mass.

Frederiksen, J.S., 1979: Baroclinic instability of zonal flows and planetary waves in multi-level models on a sphere. J. Atmos. Sci., 36, 2320-2335.

Gall, R.L., 1976a: A comparison of linear baroclinic instability theory with the eddy statistics of a general circulation model. J. Atmos. Sci., 33, 349-373.

-----, 1976b: The effects of released latent heat in growing baroclinic waves. J. Atmos. Sci., 33, 1686-1701.

Halem, M., E. Kalnay, W. Baker and R. Atlas, 1982: An assessment of the FGGE satellite observing system during SOP-1, Bull. Amer. Met. Soc., 63, 407-426.

Hahn, D.G., and L.H. Horn, 1969: The generation of available potential energy in a mid-latitude cyclone. Final Rept. ESSA Grant WBG 52, Univ. of Wisconsin, Madison.

Harrold, T.W., and K.A. Browning, 1969: The polar low as a baroclinic disturbance. Quart. J. Roy. Meteor. Soc.,95, 710-723.

Hodur, R. M., 1984: A numerical study of the Pacific polar low. Ph. D. Thesis, Department of Meteorology, Naval Postgraduate School, 187 pp.

Johnson, D. R., and W. K. Downey, 1975: Azimuthally averaged transport and budget equations for storms: quasi-Lagrangian diagnostics, 1. Mon. Wea. Rev., 103, 967-979.

Liou, C.-S., and R.L. Elsberry, 1985: Physical processes in prediction of explosive maritime cyclogenesis. Preprints 7th Conference on Numerical Weather Prediction, Montreal, Amer. Meteor. Soc.

Locatelli, J.D., P.V. Hobbs, and J.A. Werth, 1982: Mesoscale structures of vortices in polar airstreams. Mon. Wea. Rev., 110, 1417-1433.

Lorenz, E.N., 1955: Available potential energy and the maintenance of the general circulation. Tellus, 7, 157-167.

Lyall, I.T., 1972: The polar low over Britain. Weather, 27, 378-390.

Mansfield, D.A., 1974: Polar lows: The development of baroclinic disturbances in cold air outbreaks. Quart. J. Roy. Met. Soc., 100, 541-554.

Marchuk, G.I., 1982: Methods of numerical mathematics. Springer-Verlag, 510 pp.

Monteverdi, J.P., 1976: The single airmass disturbance and precipitation characteristics at San Francisco. Mon. Wea. Rev., 104, 1289-1296.

Mullen, S.L., 1979: An investigation of small synoptic-scale cyclones in polar airstreams. Mon. Wea. Rev., 107, 1636-1647.

-----, 1982: Cyclone development in polar airstreams over the winter-time continent. Mon. Wea. Rev., 110, 1664-1676.

-----, 1983: Explosive cyclogenesis associated with cyclones in polar air streams. Mon. Wea. Rev., 110, 1664-1676.

Nitta, T., and J. Yamamoto, 1974: On the observational characteristics of intermediate scale disturbances generated near Japan and vicinity. J. Meteor. Soc. Japan, 52, 11-31.

O'Brien, J.J., 1970: Alternative solutions to the classical vertical velocity problem. J. Appl. Meteor., 9, 197-203.

Okland, H., 1977: On the intensification of small-scale cyclones formed in very cold airmasses heated by the oceans. Institute Rept. Series No. 26, Universitetet i Oslo, Institutt for Geofysik, August 1977, 31pp.

Paegle, J., 1983: Some characteristics of ECMWF level III-b data sets. Global Weather Experiment Newsletter, 1, May issue.

Pagnotti, V., and L. Bosart, 1984: Comparative diagnostic case study of east coast secondary cyclogenesis under weak versus strong synoptic-scale forcing. Mon. Wea. Rev., 112, 5-30.

Palmen, E., and C. W. Newton, 1969: Atmospheric Circulation Systems: Their Structure and Physical Interpretation. Academic Press, 603 pp.

Petterssen, S., 1956: Weather Analysis and Forecasting, Vol. 1, Motion and motion systems. McGraw-Hill, 428 pp.

_____, D. Bradbury and K. Pedersen, 1962: The Norwegian cyclone models in relation to heat and cold sources. Geofys. Publ., 24, 243-280.

-----, and S. J. Smebye, 1971: On the development of extra-tropical cyclones. Quart. J. Roy. Meteor. Soc., 97, 457-482.

Randall, D.A., 1976: The interaction of the planetary boundary layer with large-scale circulations. Ph.D. Thesis, Dept. of Atmos. Sci., Univ. of California, Los Angeles, 268 pp.

Rasmussen, E., 1979: The polar low as an extratropical CISK disturbance. Quart. J. Roy. Soc., 105, 531-549.

-----, 1981: An investigation of a polar low with a spiral cloud structure. J. Atmos. Sci., 38, 1785-1792.

Reed, R.J., 1979: Cyclogenesis in polar airstreams. Mon. Wea. Rev., 107, 38-52.

Robertson, F. R., and P. J. Smith, 1983: The impact of model moist processes on the energetics of extratropical cyclones. Mon. Wea. Rev., 111, 723-744.

Rosmond, T.E., 1981: NOGAPS: Navy Operational Global Atmospheric Prediction System. Proc. Fifth Conf. on Numerical Weather Prediction, Boston, Amer. Met. Soc., 74-79.

Sanders, F., and J.R. Gyakum, 1980: Synoptic-dynamic clima-tology of the "bomb". Mon. Wea. Rev., 108, 1589-1606.

Sandgathe, S.A., 1981: A numerical study of the role of air-sea fluxes in extratropical cyclogenesis, Ph.D. Thesis, Department of Meteorology, Naval Postgraduate School, 134pp.

Sardie, J.M., and T.T. Warner, 1983: On the mechanism for the development of polar lows. J. Atmos. Sci., 40, 869-881.

Seaman, N.L., H. Otten, and R.A. Anthes, 1982: A rapidly developing polar low in the North Sea on January 2, 1979. Preprints, 1st International Conf. on Meteor. and Air/Sea Interaction of the Coastal Zone, The Hague, Netherlands, Amer. Met. Soc., 196-203.

Smagorinsky, J., 1956: On the inclusion of moist adiabatic processes in numerical prediction models. Ber. d. deutsches Wetterd., 5, No. 38, 82-90.

Staley, D.O., and R.L. Gall, 1977: On the wavelength of maximum baroclinic instability. J. Atmos. Sci., 34, 1679-1688.

Stevenson, C.M., 1968: The snowfalls of early December 1967. Weather, 23, 156-161.

Streten, N.A., and A.J. Troup, 1973: A synoptic climatology of satellite observed cloud vortices over the Southern Hemisphere. Quart. J. Roy. Meteor. Soc., 99, 56-72.

Sutcliffe, R.C., and A.G. Forsdyke, 1950: The theory and use of upper air thickness patterns in forecasting. Quart. J. Roy. Meteor. Soc., 76, 189-217.

Suttie, T.K., 1970: Portrait of a polar low. Weather, 25, 504-506.

Tallman, W.C., 1982: An investigation of quasi-Lagrangian diagnostics to the study of numerically simulated oceanic cyclones. M.S. Thesis, Naval Postgraduate School.

Tokioka, T., 1973: A stability study of medium-scale disturbances with inclusion of convective effects. J. Meteor. Soc. Japan, 51, 1-9.

Tracton, S.M., 1973: The role of cumulus convection in the development of extratropical cyclones. Mon. Wea. Rev., 101, 573-593.

Vincent, D.G., G.B. Pant and H.J. Edmon,Jr., 1977: Generation of available potential energy of an extra-tropical cyclone system. Mon. Wea. Rev., 105, 1252-1265.

Wash, C. H., and W. E. Calland, 1985: Diagnostics of explosive cyclogenesis during FGGE, northwest Pacific cyclone of 12-16 January 1979. Conditionally accepted for publication in Mon. Wea. Rev..

Wash, C. H., and W. Cook, 1985: A quasi-Lagrangian diagnostic investigation of rapid cyclogenesis in a polar air stream. Manuscript in preparation.

Weber, E.M. and S. Wilberotter, 1981: Satellite interpretation. Tech. Note 3WW/TN-81/001, 95 pp. (Available from Third Weather Wing, Offutt AFB, NE 68113).

Winninghoff, F. and R.L. Elsberry, 1983: Some aspects of post-frontal convective areas along the west coast of the United States. Naval Postgraduate School Technical Report, NPS-63-84-005.

INITIAL DISTRIBUTION LIST

		No. Copies
1.	Defense Technical Information Center Cameron Station Alexandria, VA 22304-6145	2
2.	Library, Code 0142 Naval Postgraduate School Monterey, CA 93943-5100	2
3.	Chairman (Code 63Rd) Department of Meteorology Naval Postgraduate School Monterey, CA 93943-5100	1
4.	Director New Zealand Meteorological Service P.O. Box 722 Wellington New Zealand	4
5.	Commanding Officer Naval Environmental Prediction Research Facility Monterey, CA 93943-5100	1
6.	Chief of Naval Research 800 N. Quincy Street Arlington, VA 22217	1
7.	Professor R.L. Elsberry (Code 63Es) Department of Meteorology Naval Postgraduate School Monterey, CA 93943-5100	5
8.	Professor R.T. Williams (Code 63Wu) Department of Meteorology Naval Postgraduate School Monterey, CA 93943-5100	1
9.	Professor C.H. Wash (Code 63Wx) Department of Meteorology Naval Postgraduate School Monterey, CA 93943-5100	1
10.	Professor R.G. Paquette (Code 68Pa) Department of Oceanography Naval Postgraduate School Monterey, CA 93943-5100	1
11.	Professor G.E. Latta (Code 53Lz) Department of Mathematics Naval Postgraduate School Monterey, CA 93943-5100	1
12.	Mark R. Sinclair New Zealand Meteorological Service P.O. Box 722 Wellington New Zealand	3

13. Professor R.J. Reed
    Department of Atmospheric Sciences, AK-40
    University of Washington
    Seattle, WA 98195   1

14. Dr. S.L. Mullen
    National Center for Atmospheric Research
    P.O. Box 3000
    Boulder, CO 80307   1

15. Dr. E. Rasmussen
    University of Copenhagen
    Haraldsgade 6
    DK-2200 Copenhagen 6
    Denmark   1

16. Dr. Hans von Storch
    Universitat Hamburg
    Meteorologisches Institut, Bundesstrasse 55
    2000 Hamburg 13, West Germany   1

17. Professor F. Sanders
    9 Flint Street
    Marblehead, MA 01945   1

18. Professor D. Johnson
    Space Science and Engineering Center
    University of Wisconsin
    1225 West Dayton Street
    Madison, WI 53706   1

19. Dr. Johnny C.-L. Chan (Code 63Cd)
    Department of Meteorology
    Naval Postgraduate School
    Monterey, CA 93943-5100   1